

Dual-Metal Atom Electrocatalysts: Theory, Synthesis, Characterization, and Applications

Angus Pedersen, Jesús Barrio, Alain Li, Rhodri Jervis, Dan J. L. Brett, Maria Magdalena Titirici,* and Ifan E. L. Stephens*

Electrochemical clean energy conversion and the production of sustainable chemicals are critical in the journey to realizing a truly sustainable society. To progress electrochemical storage and conversion devices to commercialization, improving the electrocatalyst performance and cost are of utmost importance. Research into dual-metal atom catalysts (DACs) is rising in prominence due to the advantages of these sites over single-metal atom catalysts (SACs), such as breaking scaling relationships for the adsorption energy of reaction intermediates and synergistic effects. This review provides an examination of the fundamental theoretical principles and experimental electrochemical performance of DACs in idealized half cells, as well as fuel cells, before proceeding to analyze the methods used for producing and identifying DACs. Current challenges and potential future research directions of DACs are also discussed.

1. Introduction

To limit global mean temperature rises while sustaining increasing energy demands, renewable energy processes and clean feedstocks need to replace those driven by fossil fuels. This is harder to attain in certain industries where alternative processes are not currently economically viable, and the industry is already highly efficient. For example, in the chemical industry, the International Energy Agency has calculated

a required reduction in emissions per unit production of 75% by 2050 in order to have a 50% chance of limiting global mean temperature rise by 2 °C compared to pre-industrial levels.^[1,2] Improvements in the field of electrocatalysts, especially in relation to electrolyzers and fuel cells, will help these devices become part of the solution to the looming sustainable energy and chemical production needs.^[3] For these devices to be entirely renewable, H₂ (and O₂) needs to be produced by water splitting in electrolyzers through H₂ and O₂ evolution (green hydrogen production), rather than from methane reforming (grey hydrogen production).^[4,5] H₂ can then be used in electrochemical O₂ reduction in fuel cells to

produce electricity.^[6,7] Meanwhile, electrochemical reduction of N₂ to NH₃ can provide a sustainable means to a critical fertilization source for the agricultural industry and a carrier for H₂.^[8] Moreover, a way of producing value-added products and a “circular economy” for industry from CO₂ emissions is via the electrocatalytically driven CO₂ reduction, which converts CO₂ to essential feedstocks, such as ethylene or ethanol for the chemical industry.^[9]

Low-temperature fuel cells and electrolyzers typically utilize catalysts based on platinum group metal (PGM) nanoparticles,^[10] which limits device commercialization due to increasing global demand, low uptake of recycling, and high cost of PGMs.^[11] Consequently, many researchers have turned their attention to reducing PGM loading or entirely replacing them with lower-cost earth-abundant metals, such as Fe, Cu, Ni, Co, Mn, and, most recently, Sn.^[12]


Regardless of the catalyst composition, improvements in the electrochemical activity have been highly sought after with two general options available; increasing the number of accessible catalytic sites and/or increasing the intrinsic activity of the catalytic sites.^[13] Many different catalyst designs have been explored in order to raise the activity, such as alloying^[14] or nanostructuring.^[15] While increasing the density of catalytic sites improves activity, this method becomes physically limited when catalyst loading affects charge and mass transport.^[13] Thus, improving the activity per catalytic site (intrinsic activity) through controlling local geometry and electronic structure has garnered research attention, with successful methods including shrinking the catalytic site down to atomic scale, as well as locally introducing light heteroatoms or hosting the catalytic site at edges.^[10,16–18]

A. Pedersen, J. Barrio, I. E. L. Stephens
Department of Materials
Imperial College London
London SW7 2AZ, UK
E-mail: i.stephens@imperial.ac.uk

A. Li, M. M. Titirici
Department of Chemical Engineering
Imperial College London
London SW7 2AZ, UK
E-mail: m.titirici@imperial.ac.uk

R. Jervis, D. J. L. Brett
Electrochemical Innovation Lab
Department of Chemical Engineering
University College London
Torrington Place, London WC1E 7JE, UK

M. M. Titirici
Advanced Institute for Materials Research (WPI-AIMR)
Tohoku University
2-1-1 Katahira, Aobaku, Sendai, Miyagi 980-8577, Japan

 The ORCID identification number(s) for the author(s) of this article can be found under <https://doi.org/10.1002/aenm.202102715>.

DOI: 10.1002/aenm.202102715

As catalyst metal clusters decrease in size to only a few metal atoms, discrete energy band structures become finely correlated with the number of metal atoms present. Consequently, adding or removing a single metal atom at this stage can largely impact the electronic structure and hence catalytic properties.^[19] Reducing catalytic sites all the way down to well-dispersed single-metal atom catalysts (SACs) effectively increases the proportion of metal centers with low coordination, thereby fully exploiting each metal atom, which, if well defined, can be tuned to selectively drive specific reactions.^[20] In terms of synthesis, SACs typically suffer from the formation of metal

nanoparticles, which are caused by the large surface energy of single metal atom sites inducing aggregation. Hence, catalyst loadings are typically kept below 1–2 wt%, which can limit the overall activity.^[21,22] Additionally, many reactions, such as O–O scission,^[20] N–N scission,^[23] C–C coupling,^[24] or CO hydrogenation,^[25] require several contiguous metal atoms. Indeed, looking towards nature, some of the most difficult multi-electron reactions involve two earth-abundant metal atoms at the active site.^[26] Cytochrome *c* oxidase (CcO), where a single Cu_B sits above the heme *a*₃ site, as illustrated in **Figure 1a**, enables its highly efficient and selective four-electron reduction of dioxygen

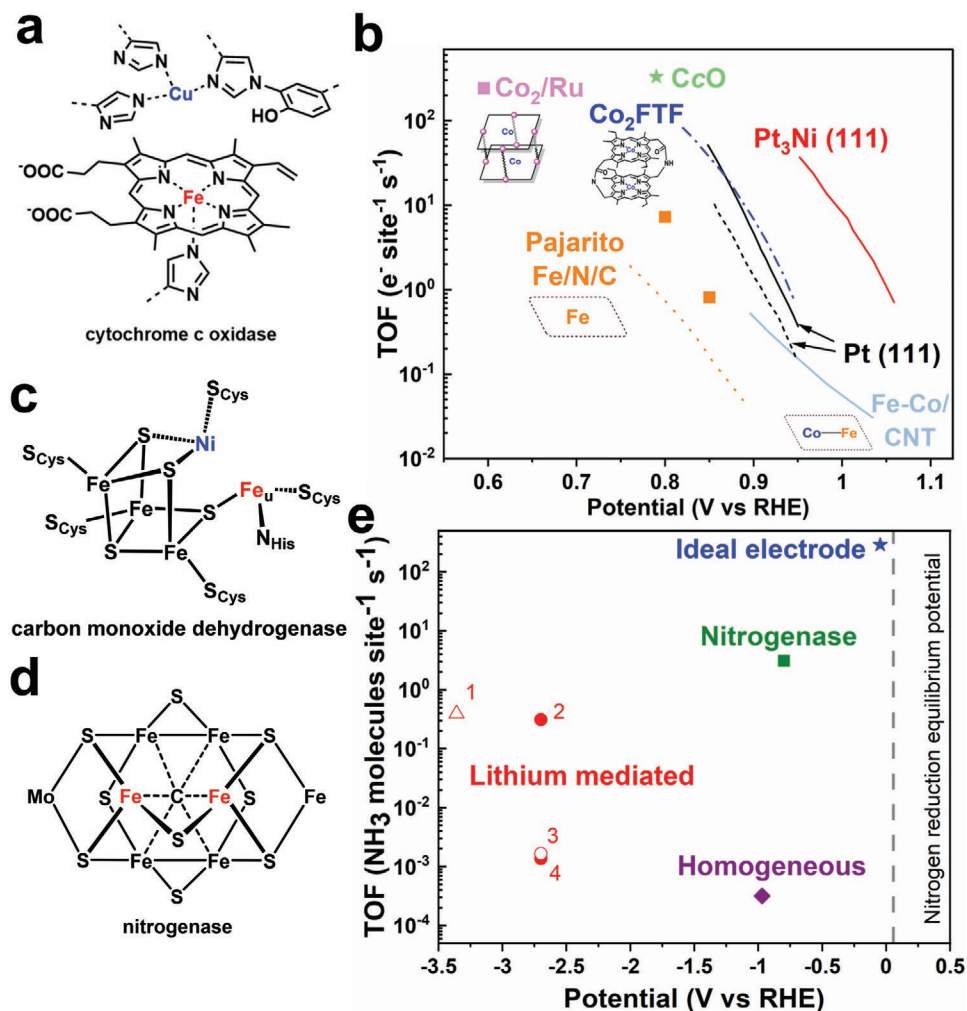


Figure 1. a) Cu_B site sitting above heme *a*₃ in CcO. Based on reference [35]. b) Calculated TOF at varying potentials for dual-metal atom active site in molecular (Co₂/Ru, Co₂FTF), enzyme (CcO), and heterogeneous (Fe-Co/CNT) electrocatalysts, plus Pt(111), Pt₃Ni(111), and a commercial single atom electrocatalyst (Pajarito). Co₂/Ru (pink square) in 0.5 M H₂SO₄ electrolyte. Co-Tolyl prism with Ru represented by pink spheres (see Section 3.3).^[36] Co₂FTF (blue dash-dot line) in 0.5 M CF₃CO₂H at 250 rpm.^[37] CcO (green star): A ferroxidase CcO with ferrocenecarboxylic acid redox mediator.^[32] Fe-Co/CNT (light blue solid line) in 0.1 M KOH at 1600 rpm.^[38] Pajarito: PMF-011904 catalyst in 0.5 M H₂SO₄ at 1600 rpm. Orange dotted line represents ex situ CO chemisorption results while orange squares represent in situ electrochemical NO₂⁻ stripping values.^[39] Pt(111): black dashed line in 0.1 M HClO₄, black solid line in 0.1 M KOH, both at 1600 rpm.^[40] Pt₃Ni (red line) in 0.1 M KOH at 1600 rpm.^[41] See Supporting Information for calculations on TOF of catalysts. c) Structure of metalloenzyme carbon monoxide dehydrogenase with highlighted Fe and Ni dual atom center. Based on reference [42]. d) Structure of metalloenzyme nitrogenase for N₂ reduction with highlighted Fe-S-Fe bridged center. Based on reference [26]. e) TOF of N₂ reduction catalysts, including nitrogenase,^[43,44] homogeneous,^[45] and lithium mediated (1,^[46] 2,^[8] 3,^[47] 4^[48]) at varying potentials (vs RHE) (filled symbols, 1 bar N₂, and open symbols higher pressures). Triangles represent the recyclable proton donor of Suryanto et al.,^[46] and circles indicate sacrificial ethanol proton donors. Potentials were corrected for ohmic losses and can become more negative during operation. Based on reference [44].

to water, without the production of hydrogen peroxide.^[27–29] The O₂ reduction activity of the dual atom site is demonstrated in Figure 1b (results discussed further in Section 2.1.2), where a model CcO shows the highest reported turnover frequency (TOF), well over an order of magnitude higher than a commercial SAC (Pajarito). For CO₂ reduction, the dual-metal atom active sites in carbon monoxide dehydrogenase (Figure 1c) and nitrogenase (Figure 1d) are highly studied, with the latter also remarkably able to catalyze N₂ to ammonia (through reduction under ambient conditions) with the highest TOF to date (Figure 1e).^[30] There are several variants of nitrogenase, namely molybdenum, vanadium, and iron. Of these, Mo-nitrogenase is the most efficient of the three and consequently the most widely studied. The active center in molybdenum nitrogenase is the Mo:7Fe:9S:C homocitrate cluster, where the two Fe atoms bridged by S are surrounded by a matrix of hydrophobic peptides (Figure 1d), which allow the controlled diffusion of protons to the active site via a proton wire.^[31] Enzymes can be attached to electrodes for efficient electrocatalytic reactions,^[32] although in harsh fuel cell environments enzyme stability is an issue (enzyme activity diminishes in hours),^[33] in addition to their large preparation, purification, and electrode surface area footprints.^[34] However, certain key characteristics can be identified and mimicked, such as their dual-metal atom core.

Herein, we define dual-metal atom catalysts (DACs) as catalytic sites containing two isolated metal atoms in atomic proximity to each other, which directly or indirectly cause a change in binding energies of reaction intermediates. These metal atoms are isolated by a more inert substrate which typically does not bind to the reactive intermediate, such as N, C, Au, or S. The orientation of the DAC within the host material can give rise to two divisions in classification, depending on whether the DAC is “in-plane” or “cofacial” about the orientation of the metal atom centers and their supporting environment. The types of DAC explored in this Review include in-plane adjacent and bridged DACs, along with cofacial separated DACs.

In-plane adjacent DACs are those with two reactive metal atoms directly coordinated to one another in the same plane, as illustrated in Figure 2a-i.^[49–52] For in-plane bridged DACs, the two metal atoms are separated by a linking or bridging atom, such as oxygen or nitrogen, as displayed in Figure 2a-ii.^[19,53] Cofacial separated DACs are those with the metal atoms atomically distanced in a different plane, as shown in Figure 2b,^[37,54] which potentially allows for adsorption of a reactant between the planes. We use the DAC terms defined above throughout this Review to enable efficient determination of the type of DAC being discussed.

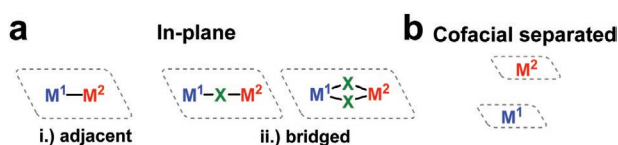


Figure 2. a) Representation of in-plane adjacent and bridged DACs. b) Representation of cofacial separated DACs. Gray dashed lines represent the local support environment of the metal atoms. M¹ and M² represent metal atoms while X represents bridging atoms that do not bind to intermediates, such as O and N.

DACs can combat some limitations of SACs in multielectron reactions with several reaction intermediates, while also potentially possessing 100% site utilization that has been achieved by SACs.^[55] For example, the two metal centers in DACs can provide two points for reactant binding in a 3D geometry, enabling independent binding energies theoretically predicted for ideal O₂ reduction and O₂ evolution catalysts which are not.^[56] DFT calculations predict that the bridged reactant and intermediates adsorption for in-plane adjacent DACs can significantly improve N₂ reduction activity,^[23] while calculations on separated cofacial DACs predict hydrocarbon production during CO₂ reduction.^[57] Heteronuclear DACs in particular can improve activity, stability, and selectivity by tuning the metal centers to alter the electronic structure, which is not possible to the same degree in homonuclear counterparts.^[58] This is because of the opportunity to adapt the ligand atoms, coordination number, and local structure of the metal centers in heteronuclear DACs.^[59] While DACs are predicted to possess superior electrocatalytic activity compared to SACs in certain reactions, their controlled synthesis has been difficult to achieve and, once synthesized, these sites may display low electrochemical or structural stability arising from high surface energy of low-coordination atoms.^[60] The metal atom centers are typically stabilized by coordination to N-doped carbon supports,^[38,52,61,62] which are favorable due to their robustness, low cost, and tunability.^[63,64] Other supports have been successfully utilized to create DACs such as carbon nitrides,^[65,66] and macrocyclic compounds including porphyrins and phthalocyanines.^[54,67]

Tri-metal atom catalysts (TACs) have also shown similar beneficial electrocatalytic properties to DACs,^[68] although the preparation of TACs is even harder to precisely regulate and orientate, explaining their thus far limited experimental synthesis.^[60] Consequently, we do not discuss TACs in detail in this Review. Other types of electrocatalytic sites which can also be highly active are those based on perovskite and metal oxides;^[69–71] however, they are beyond the scope of this Review as they do not directly pertain to DACs, as defined above.

Briefly reviewing the history of DACs in Figure 3, Jasinski first demonstrated the synthesis of a SAC in 1964 using cobalt phthalocyanine (CoPc) as a fuel cell cathode catalyst.^[72] Mitchell and Pérez-Ramírez have succinctly summarized the subsequent key historical events related to SACs.^[73] In terms of DACs, the electrocatalytic properties of macrocycle-derived DACs were first experimentally tested back in 1979 and 1980 by Collman et al., who synthesized dicobalt facing porphyrins for O₂ reduction.^[37,74] Results showed certain Co₂ diporphyrin catalysts nearly exclusively formed water, unlike single cobalt porphyrins, providing early indications of DACs’ electrocatalytic potential. It was not until 2017, when Wang et al. synthesized the first characterized heterogeneous catalyst from a Fe–Co metal-organic framework (MOF), which demonstrated excellent fuel cell performance.^[49] In 2018, Nørskov and co-workers calculated that DACs could provide a path to producing ammonia through electrochemical means owing to the unique binding energies of DACs.^[23] Since then, various methods for producing DACs have been explored; of particular note is the electrodeposition of Fe onto Co for O₂ evolution,^[58] and the atomic layer deposition (ALD) of Pt–Ru dimers utilized for H₂ evolution.^[75] From a theoretical perspective, Rossmeis and co-workers have modeled

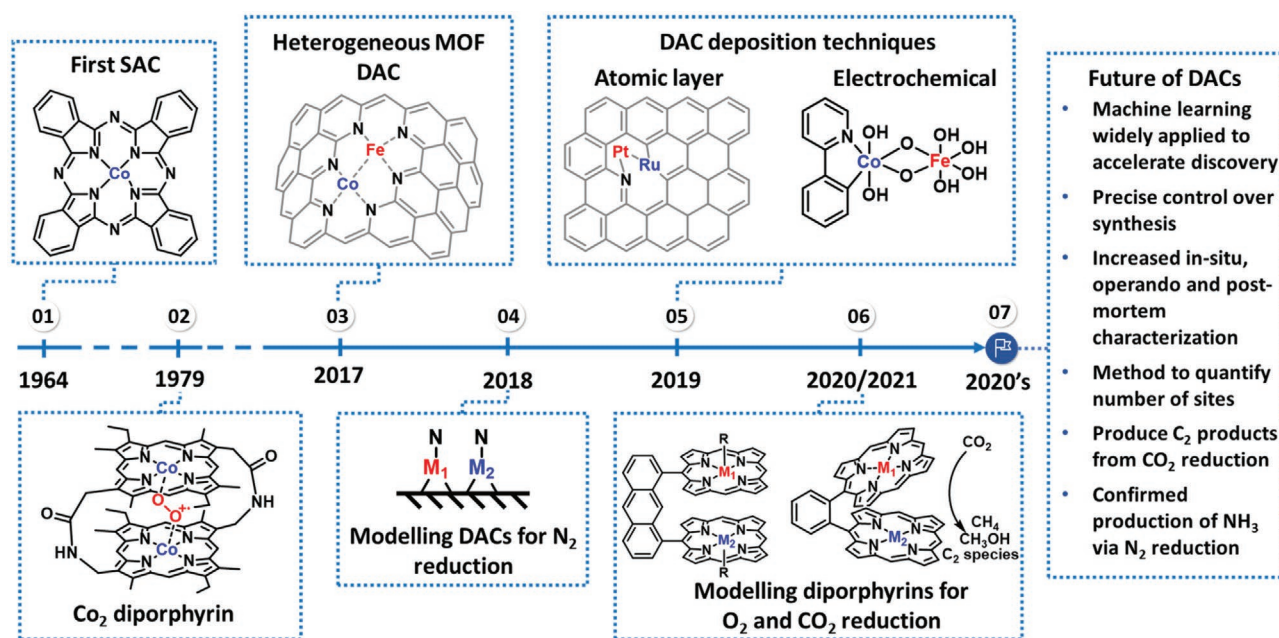


Figure 3. Summarizing the past achievements in DACs and potential future research directions.

diporphyrins, akin to cofacial separated DACs, for O_2 reduction, O_2 evolution, and CO_2 reduction, which has revealed desirable adsorbate and intermediate binding energies for improved electrocatalytic performance.^[56,57,76] Key developments being explored in the near future include machine learning for DAC discovery, precisely controlled synthesis of DACs, further applications of in situ, operando and postmortem characterization and also the conclusive experimental synthesis of ammonia via electrochemical N_2 reduction using DACs.

There have been numerous reviews on SACs for electrocatalysis over the past few years,^[77–86] with some providing certain insights in the area of DACs.^[10,16,60,87,88] However, there are few focused reviews on emerging research of DACs within electrocatalysis,^[89,90] or even general catalysis.^[91] This review focuses on DACs for the O_2 reduction, CO_2 reduction, O_2 evolution, and N_2 reduction electrochemical reactions. We review the literature regarding computational and theoretical predictions via density functional theory (DFT) and other methods, before discussing the experimental performance of DACs for each electrochemical reaction. Then, different synthesis methods for DACs are detailed, followed by the methods and challenges of characterizing such catalysts, and finally concluding with the summary, challenges, and perspectives.

2. Theoretical Insights and Experimental Results

Sabatier's principle states that the ideal catalyst should bind neither too strongly or too weakly to reaction intermediates.^[92] More recently, Nørskov and co-workers provided the theoretical underpinning to Sabatier's principle. Using DFT they revealed the quantitative relationship between catalytic activity and the binding strength of reaction intermediates for O_2 reduction, producing a “volcano” type relationship with a peak activity for

intermediate binding strengths.^[93] Experiments have directly confirmed this theoretical relationship on both model molecular catalysts^[94] and platinum single crystals.^[40,95,96] They later found similar models apply to a number of different electrocatalytic reactions, including H_2 evolution,^[97] O_2 evolution,^[98] CO_2 reduction,^[99] and N_2 reduction.^[100] While volcanoes work well for catalyst activity optimization within a family of materials by obtaining activity descriptors, they poorly assess other important criteria, such as stability.^[101] Hence, theory sections focus on explaining the underlying theoretical trends and activity descriptors of DACs relative to SACs and metal surfaces for O_2 reduction, O_2 evolution, CO_2 reduction, and N_2 reduction.

2.1. O_2 Reduction

The development of H_2 /air fuel cells, which can convert energy in a clean manner from H_2 , has been hindered commercially by the sluggish kinetics of O_2 reduction, which currently requires Pt-based electrocatalysts for sufficient activity and durability. Therefore, reducing or replacing Pt-based electrocatalysts has been a key objective for researchers over the past decades.

2.1.1. Theory

The common pathways for O_2 reduction electron transfer are either via a desired direct four-electron reduction, which forms H_2O in acid, or OH^- in alkaline media, or via a two-electron reduction, which forms H_2O_2 ^[102] (also an industrially important chemical^[20]) as an intermediate, although this is not desired for fuel cell applications.

The four-electron mechanism can proceed either by associative ($*O$, $*OH$, and $*OOH$ intermediates, where $*$ represents

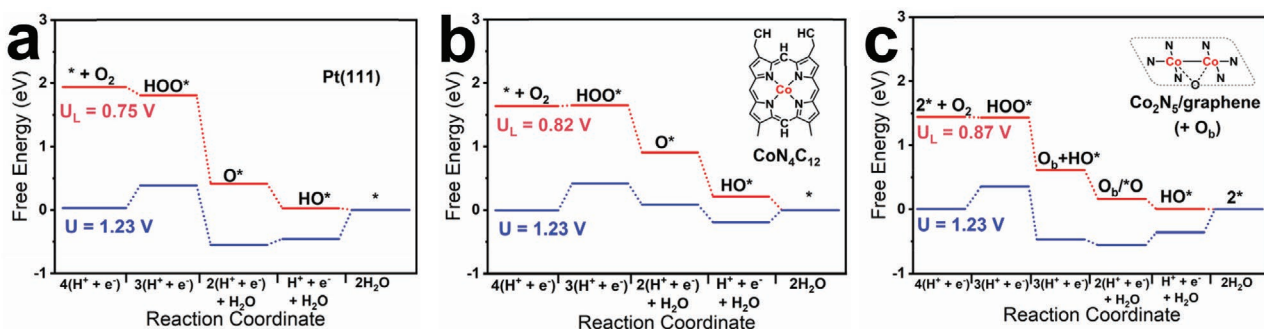
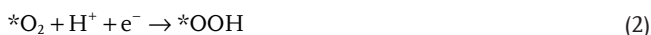


Figure 4. Free energy diagrams for O_2 reduction at limiting potential (U_L , red lines) and equilibrium potential (U , blue lines), with * indicating active site. a) Pt(111) with the associative mechanism. Based on reference [106]. b) CoN_4C_{12} porphyrin with the associative mechanism. c) Dissociative mechanism for in-plane adjacent Co_2N_5 /graphene with O adsorbed behind DAC site (O_b) to reacting O_2 . Gray dashed line represents the surrounding graphene sheet. CoN_4C_{12} and Co_2N_5 /graphene values calculated with VASP solvent model. Based on reference [107].

an adsorption site on the catalyst surface) or dissociative ($*O$ and $*OH$ intermediates) pathway, depending upon the oxygen activation barrier for dissociation on the catalyst surface.^[93] The four-electron pathways in acidic environment for associative, Equations (1–5), and dissociative, Equations (6–8), mechanisms are displayed below. An ideal catalyst would have a completely flat free energy profile at the equilibrium potential. What is evident from the free energy profile in **Figure 4a** is that metal surfaces such as Pt(111) possess a minimum overpotential of 0.3–0.4 V,^[76,93] roughly corresponding to the overpotential required to obtain a significant reaction rate in experiments (see Figure 1b). Similar overpotential restrictions are also found on SACs (Figure 4b). This overpotential arises due to linear scaling between reaction intermediates which prevents the binding energies from being tuned independently of each other, represented as volcano relationships. Without breaking the linear scaling relations of key adsorbed reaction intermediates ($*OOH$ and $*OH$) or the Bronsted-Evans-Polanyi relation between the activation energy of O_2 dissociation and adsorption energy of $*O$. Proposed methods to break scaling relations,^[101] and reduce overpotential, have included creating tensile lattice strain on the catalyst surface, creating transient conditions via resonance oscillations, confinement, and 3D catalytic sites, with some of these methods exploited by the naturally occurring enzyme CcO.^[15,27,103–105] Below, we explore the effect of a dual atom catalytic site, which can enable a different reaction pathway (Figure 4c) and/or modify the binding energy of a particular reaction intermediate, leading to a theoretically reduced overpotential limit.

Associative mechanism:



Dissociative mechanism:



Collman et al. were the first to reveal the potential of DACs by observing cooperativity between Fe and Cu within a model CcO, which opened up the possibility of alternative reaction pathways for O_2 reduction that do not include the linear scaling problems arising from the $*OOH$ intermediate in associative mechanisms of O_2 reduction.^[108] Because of this, cofacial separated metalloporphyrins, or diporphyrins, were later investigated due to their structural similarity with the DAC center in CcO.^[109] From DFT studies, diporphyrins are shown to exhibit different electron pathways depending on where the O_2 binds; if binding on the outside in end-on fashion, they behave like a single porphyrin with a SAC center, being two-electron selective (**Figure 5a**). In contrast, if O_2 binds on the inside, it is four-electron selective as O_2 is adsorbed by a bridge-*trans* configuration with weakened O=O bonding (Figure 5b).^[109,110] These DFT observations explain why in biological systems the active metal atom has saturated coordination on the opposite side to the binding reactant to prevent undesired reactions.^[111] This computational result arises from the O_2 μ -bridge link between the metal centers of the diporphyrin sharing structural similarity to dissociated oxygen, as each oxygen atom is adsorbed to its own metal site.^[112] This means the oxygen atoms do not need to move to a hollow site, as is the case for pure metal surfaces.^[113] Because of this, O_2 dissociation can be achieved with weaker binding to O_2 reduction intermediates, hence synthesizing ligands on the outside of diporphyrins could potentially improve O_2 reduction kinetics.^[112] Of possible diporphyrins, Rossmeisl and co-workers initially identified that “pacman,” diporphyrin anthracene (DPA), and dioporphyrin dibenzofuran (DPD) containing strong binding metals (Mn, Fe, or Co) with ligands (Figure 5c,d) or without, could reduce overpotential below 0.3 V through a less restricted $*O + *OH$ pathway which bypasses $*OOH$ scaling.^[112] In particular, DPA containing Co centers and NH_3 ligands showed the lowest overpotential of ≈ 0.15 V, with facilitated $*OOH$ dissociation in the optimal

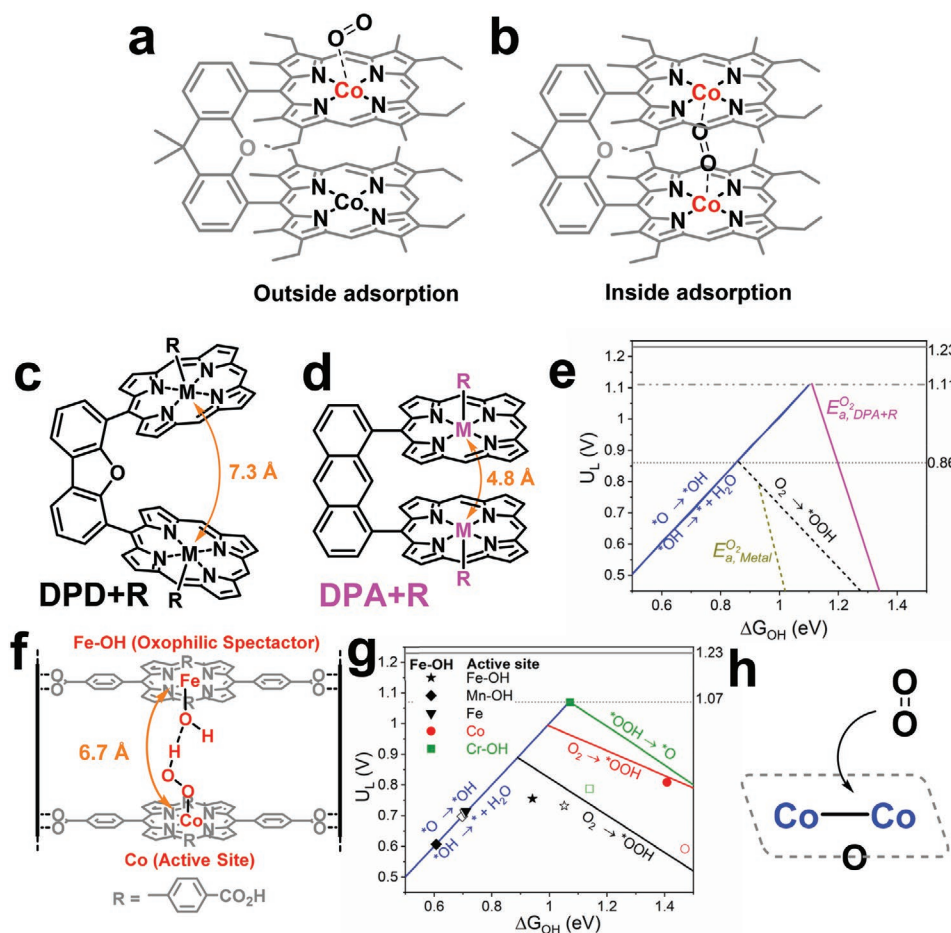


Figure 5. a) End-on O_2 adsorption on single Co site. b) Bridged O_2 adsorption inside the cofacial separated structure. Based on reference [109]. c) Side view of DPD+R structure. d) Side view of DPA+R structure. M represents metal (e.g., Mn, Co, or Fe) and R represents the coordination of ligands. Based on reference [112]. e) Activity volcano displaying the improved overpotential through modified scaling relationships in DPA motifs compared to metal surfaces, based on adsorption energy of $*OH$, ΔG_{OH} . Blue solid line represents potential limited by strong binding of $*OH$. Black solid and dash lines represent potential limited by weak binding of $*OOH$. E_a represents both O_2 adsorption energy and dissociation energy of adsorbed $*O_2$ to two adsorbed $*O$, with $E_a^{O_2}$ illustrating potential limited by O_2 dissociation. The dashed lime line represents $E_{a,metal}^{O_2}$ of metal surfaces and pink solid line represents $E_{a,DPA+R}^{O_2}$ of DPA with ligand coordination (depicted in d). Based on reference [76]. f) Structure of PMOF-Al with separated cofacial sites consisting of Co active site with $*OOH$ intermediate and Fe-OH spectator. Thick solid line represents Al-oxide chain. g) Volcano plot showing change in activity for scenarios of Fe-OH spectator (filled symbols and red and green volcano legs) and no spectator (empty symbols and black volcano leg). Based on reference [115]. h) In-plane adjacent Co_2 with O adsorbed behind DAC site to reacting O_2 . Gray dash line represents graphene sheet. Based on reference [107].

oxygen adsorption energy region between 0.9 to 1.4 eV, indicated in Figure 5e.^[112]

Other separated cofacial macrocyclic DACs have also been predicted to circumvent O_2 reduction scaling relations,^[114] even those based on industrially relevant MOF-based materials whose 3-D structure can be manipulated to the reaction of interest. Here, Sours et al.^[115] based their rational DFT analysis on water stable and ORR active PMOF-Al,^[116] which consists of ≈ 6.7 Å spatially stacked TCPP (tetrakis(4-carboxyphenyl)-porphyrin) ligands connected via 1-D Al-oxide chains (Figure 5f). The transition metal spacing of ≈ 6.7 Å was found in the favorable region for $*OOH$ stabilization from the initial analysis. Porphyrinic zirconium MOF (PCN-226(Co)) developed by Huang and co-workers provides another example of tailored active site spacing (7 Å),^[117] suggesting similar porphyrin-based MOFs could serve as ideal catalysts for O_2 reduction by forming

$M_1-O-O-M_2$ bridges in a regulated way. For Sours et al.'s calculations, the most stable coverages and oxidation stages of the transition metals explored ($M_1 = Cr, Mn, Fe, Co, Ni$; $M_2 = Cr, Mn, Fe$) were based on Pourbaix diagrams.^[115] Sours et al. found $*OOH$ became more stabilized with increased electronegativity ($Mn < Cr < Fe$), owing to the charge delocalization on the spectator ligand ($-OH$) which resulted in a stronger hydrogen bond.^[115] The predicted greatest limiting potential for the transition metals is achieved by Cr-Fe/PMOF-Al DAC with 1.07 V (Figure 5g).^[115] As noted by the authors, $*OOH$ stabilization only improves activity for catalysts who are influenced by their potential-determining step.^[115] OH as a modifying ligand has also been considered for in-plane adjacent DACs.^[118]

Vegge and co-workers explored Co SAC and both in-plane and cofacial Co_2 DACs on N-doped graphene sheets with different solvent DFT models.^[107] The Co SAC followed an

associative O₂ reduction mechanism while both Co₂ DAC types increased O₂ reduction activity and suppressed H₂O₂ formation by facilitating *OOH dissociation to *O and *OH. Interestingly, only with an O adsorbed strongly to the in-plane adjacent Co₂ on the opposite side of the reacting O₂ (Figure 5h) did appreciable deviation from scaling relations occur, suggesting the limiting potential could be improved assuming the *OH adsorption was weakened.

One issue that arises from DACs is the vast number of possible metal atom combinations that could be tested for O₂ reduction, among other electrochemical reactions. To tackle this issue, a comprehensive set of DFT results from in-plane adjacent DAC coordinated to N on graphene for O₂ reduction was developed for training in a machine learning study to discover hidden trends within the data.^[119] While collecting the DFT results, experimentally unexplored and potentially highly active DACs were discovered, such as Ni–Cu. In the machine learning study, various factors determined to influence O₂ reduction activity were identified and ranked based on a mean impact value, with the top three features for the metal atoms calculated as their electron affinity, sum of the Van der Waals radius, and Pauling electronegativity.

2.1.2. Experimental

A key metric for evaluating experimental catalysts is through their intrinsic activity, which can be defined by calculating their TOF. Progress has been made on TOF calculations of SACs by measuring active site density using ex situ cryo CO pulse chemisorption and temperature-programmed desorption,^[120,121] in situ electrochemical NO₂[−] stripping^[122] and, recently, in situ cyanide anion probe.^[123] Lower TOF values are obtained with temperature-programmed desorption of CO, as the ex situ adsorbed CO overestimates the number of electrochemically accessible active sites, resulting in a lower calculated TOF. Mössbauer spectroscopy can also probe the total density of specific sites, although deviating from the number of sites accessible for adsorption of O₂ or CO, due to being a bulk characterization technique (Section 4.2.3).^[121] It has been previously discussed that the true catalytic TOF value likely lies between that obtained from in-situ electrochemical NO₂[−] stripping and ex situ temperature-programmed desorption of CO.^[39] In terms of DACs, molecular cofacial separated Co prisms (Co₂/Ru) have obtained TOF values close to CcO, albeit at lower potentials and with Ru clips (Figure 1b).^[36] Ru influence on the complexes' activity was not well detailed with Ru SACs known for O₂ reduction activity.^[124] Interestingly, calculated TOF values of cofacial separated Co complexes (Co₂FTF) compete with those for Pt(111) (Figure 1b). To date, the vast majority of heterogeneous DAC electrocatalysts have not included TOF calculations for O₂ reduction, due to a lack of established methods for accurate site density determination for DACs. From Figure 1b, Fe-Co/CNT shows greater TOF than the evaluated Fe/N/C SAC (Pajarito), with similar TOF values to Pt(111), but markedly less than Pt₃Ni(111) (the most active O₂ reduction catalyst ever observed in aqueous environments^[41]). Notwithstanding ambiguities in the TOFs calculations, experiments, thus far, suggest that while DACs seem to be more active than SACs, they have

not yet achieved the outstanding activity promised by the theoretical calculations.

Ye et al. were able to separately synthesize in-plane Fe-based SAC and in-plane adjacent DAC and TAC on N-doped carbon denoted as Fe₁-N/C, Fe₂-N/C and Fe₃-N/C, respectively, by utilizing different Fe precursors (Fe₂-N/C synthesis shown Section 3.1.1). The specific activity in acidic electrolyte (0.5 M H₂SO₄) (at 0.75 V vs RHE) was 16.4 mA cm^{−2} for Fe₂-N/C, approximately 4.9 and 1.7 times higher than Fe₁-N/C and Fe₃-N/C, respectively.^[68] This was attributed to peroxo-like adsorption of O₂ on the Fe₂ and Fe₃, as observed by low-temperature FTIR (Section 4.2.5), which facilitated O–O bond cleavage by increased O–O bond length according to DFT calculations. Similar peroxo-like O₂ adsorption geometry was observed by Xiao et al. and Lu et al. for their in-plane adjacent Co₂/N/C and Zn-Co/N/C DAC, respectively.^[50,125] Following stability testing of 20 000 cycles, Fe₁-N/C exhibited the lowest shift in E_{1/2} (Figure 6a). This result was attributed to the dissociation of trace amounts of Fe–Fe bonding in Fe₂-N/C and Fe₃-N/C which was examined through high-angle annular dark-field scanning transmission electron microscopy (HAADF-STEM).^[68]

In the work by Wei and co-workers, Fe-CoN_x-OH/C sites were achieved through OH-ligand self-binding strategy on N-doped carbon applied to a Fe–Co binuclear site.^[126] They propose that the electron-withdrawing OH ligand modifies the energy level of Fe, promoting the intermediate adsorption binding of Fe–O, while the triangular geometry facilitates the breaking of the O–O bond through a bridge-*cis* adsorption model. Additionally, the kinetic current density at 0.85 V for Fe-CoN₅-OH/C was 7245 mA cm^{−2}, while FeN_x/C and CoN_x/C only managed 0.339 and 0.110 mA cm^{−2}, respectively, resulting in an intrinsic activity over 20 times greater for the Fe-CoN₅-OH/C electrocatalyst.

Since Collman et al. first discovered the activity of Co₂FTF (Figure 6b),^[37,74] various cofacial separated DAC phthalocyanines (M₂Pc₂, M = Zn, Co, Fe, Cu) connected by rigid linkages have been prepared by Bekaroglu and co-workers for O₂ reduction.^[127–133] From their work, Fe₂Pc₂ was found to display the best activity, suggesting that the cofacial separated metals bind oxygen molecules to form M–O–O–M, leading to the four-electron pathway. To improve upon the rigid linker design, Tanaka and co-workers experimentally synthesized and tested a cofacial bridged μ-oxo-Fe(III) diporphyrin and diphthalocyanine connected by a flexible fourfold rotaxane DAC (Figure 6c).^[54] A possible O₂ reduction pathway was suggested whereby the cofacial bridged DAC becomes a separated DAC following two-electron O₂ reduction and prior to four-electron O₂ reduction. In a different design, Cao's group devised a cofacial separated Co-based bisporphyrin dyad resembling a Pacman shape (Figure 6d),^[35] very similar to theoretical catalysts in Figure 5c.^[35] The DACs were more efficient and selective than mononuclear counterparts; for instance, the electron transfer number for O₂ reduction was only 2.9 for Co porphyrin SACs, whereas values of 3.8 and 3.9 were obtained for cofacial separated symmetrical and asymmetrical DACs, respectively. Interestingly, the asymmetrical Co DAC outperforms its symmetrical counterpart in terms of greater O₂ reduction currents and reduced overpotentials. So far, evidence of experimentally synthesized heterogeneous catalysts with controlled separated cofacial catalytic sites

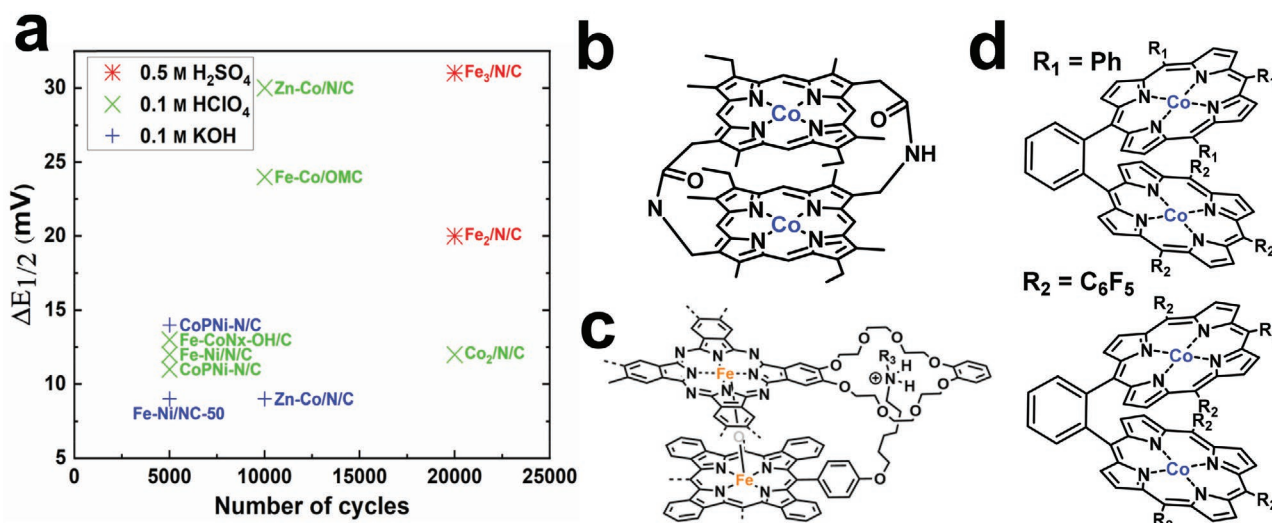


Figure 6. Reported performance of DACs a) for change in O_2 reduction half-wave potential ($\Delta E_{1/2}$) following cycling stability testing. b) Separated cofacial Co–Co (Co_2TF) DAC. Based on reference [37]. c) μ -oxo-dinuclear Fe complex consisting of fourfold rotaxane heterodimer of a porphyrin and a phthalocyanine. Three arms of fourfold rotaxane have been omitted for clarity. Based on reference [54].

forming $M_1-O-O-M_2$ bridges is scarce. Joo's group synthesized Fe–Co ordered mesoporous porphyrinic carbons (Fe–Co/OMC) (Section 3.1.2).^[134] These were suggested to have formed Co–OH–Co or Fe–O–O–Fe bridges during O_2 reduction according to their DFT calculation where M_1-M_2 distances were ≈ 4.6 Å, which agreed well with EXAFS results and HRTEM of inter-layer distances (4.8 Å). Although, alignment of the metal site positions remains an issue with their synthesis method.

2.1.3. Hydrogen Fuel Cell

The aim for DACs is to be applied in energy and chemical conversion devices. Electrochemical testing is typically applied initially in a rotating disc electrode (RDE) configuration; however, operational differences between RDEs and fuel cells exist. The main issues with RDE testing lie in the low catalyst loadings required for the thin films and small current densities obtained due to low oxygen solubility in the electrolyte, which leads to mass transport limitations.^[135] RDE setups also typically

employ less harsh environments during testing compared to fuel cells (generally using 0.1 M concentration electrolytes at room temperature). Taking this into account, it is not possible to accurately predict the activity in membrane electrode assemblies from measured RDE values;^[136] however, trends in activity between the two methods have been shown.^[137] Alternative testing regimes more representative and comparative to a fuel cell system, such as floating electrode^[138] and gas diffusion electrodes^[139–141] have also been developed, although no DACs considered in this review have done so.

Following initial testing in RDEs, DACs in H_2/O_2 fuel cell operation have been demonstrated on several occasions with promising activity (Figure 7a). The Fe–CoN_x-OH/C DAC of Xiao et al.^[126] presents the highest activity at 0.8 V, although there is a lack of details on the testing conditions (Table 1). So far, only Wang et al.^[49] have presented results of a DAC (Fe–Co/N/C) under more relevant H_2 /air supply (Figure 7b), which now falls well below the current state-of-the-art Fe-based catalysts. Under H_2 /air conditions and constant-current operation of 600 mA cm⁻² and 1000 mA cm⁻² the catalyst displayed a negligible change in

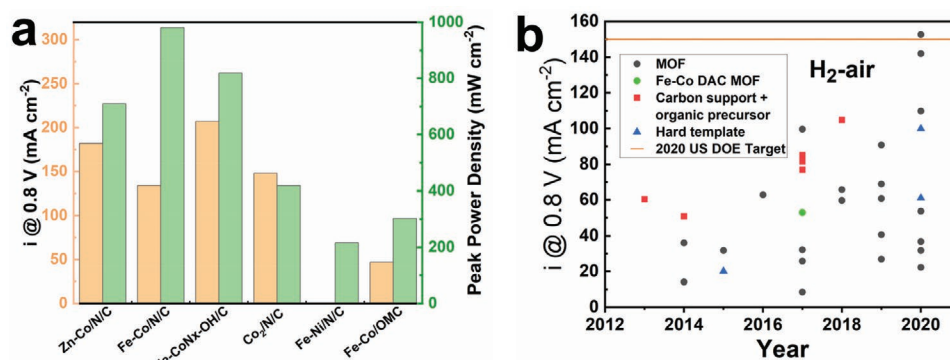


Figure 7. a) H_2/O_2 fuel cell activity at the cathode for non-PGM DACs. Operational details and references found in Table 1. b) H_2 -air fuel cell activity (not iR -corrected) of Fe-based catalysts from 2013 to 2020, with MOF derived Fe–Co DAC^[49] highlighted in green. Synthesis method: carbon support + organic precursors (CB); hard template (HT); US Department of Energy (US DOE). Based on reference [142].

Table 1. Performance of fuel cells containing DACs at the cathode.

Catalyst material	Gas supply	Catalyst loading [mg cm ⁻²]	Back pressure [Mpa]	Temperature [K]	<i>i</i> _{0.8} [mA cm ⁻²]	Peak power density [mW cm ⁻²]	Refs.
Zn-Co/N/C	H ₂ /O ₂	–	–	–	182	710	[50]
Fe-Co/N/C	H ₂ /O ₂	0.77	0.2	353	134	980	[49]
Fe-Co/N/C	H ₂ /O ₂	0.77	0.1	353		850	[49]
Fe-Co/N/C	H ₂ /air	0.77	0.2	353	53	505	[49]
Fe-CoN _x -OH/C	–	–	–	–	207	819	[126]
Co ₂ /N/C	H ₂ /O ₂	4	0.14	353	148	418	[125]
Fe-Ni/N/C	H ₂ /O ₂	4	0.21	353	0	216	[51]
Fe-Co/OMC	H ₂ /O ₂	1.5	0.2	353	47	302	[134]
Pt-O ₂ -Fe-N ₄ /C	H ₂ /O ₂	3	0.21	353	602	860	[143]

working voltage during 100 h, indicating the potential catalyst stability. Although, far longer stability would need to be exhibited for automotive applications, with the US DOE 2025 target set as 8000 h under automotive load cycling.^[144]

Summarizing observations of the literature, it is clear there is a lack of progression from RDE to fuel cell for DACs. This progression could be bridged by using alternative setups such as floating electrodes or GDEs. So far DACs have not experimentally achieved the desired low overpotential predicted by theory. Although, the lack of published fuel cell testing suggests some DACs may have issues of stability and durability under the harsher reaction conditions of a fuel cell. Further to this, some authors have used operating conditions not aligned to standardized protocols set out by institutions such as the US DOE,^[144] and have not detailed all key information regarding the fuel cell operation (Table 1), making it difficult to compare catalysts' performance. In terms of characterization, more common comparison of DACs prior and post fuel cell operation would provide confirmation the catalytic site structures does not become altered after testing, as shown by Wang et al. using XAS.^[49] Developments in operando XAS for fuel cells have also been made,^[145] which could provide critical information on changes in the active site of DACs during operation.

To yield high current densities in real devices, it is imperative to maximize the active site density in addition to creating highly intrinsically active DACs. For SACs, Jiao et al.^[55] demonstrated 100% site utilization (using a chemical vapor deposition approach) with an active site density of 1.92 × 10²⁰ sites g⁻¹ (based on CO sorption), an order of magnitude higher than a commercial Fe/N/C SAC (Pajarito) (2.02 × 10¹⁹ sites g⁻¹).^[39] While TOF was similar for both SACs (0.71–0.80 e site⁻¹ s⁻¹ at 0.8 V vs RHE), Jiao et al. yielded unprecedented O₂ reduction activity in a H₂-O₂ fuel cell (33 mA cm⁻² at 0.90 V, not iR corrected).^[55] Finally, to realize high power performance in fuel cells, the reactant accessibility to the catalyst needs consideration since active sites are typically hosted in micropores, thus requiring a well-connected macroporous structure to enable efficient O₂ transport.^[146]

2.2. O₂ Evolution

Electrochemical water splitting provides a potential source of carbon emission-free hydrogen production. It is generally limited by the O₂ evolution at the anode, owing to its high

overpotential.^[147] In terms of results so far, RuO₂ and IrO₂ are examples of the few catalysts with sufficient stability and activity for the harsh conditions of acidic O₂ evolution,^[148,149] however, they are both expensive and scarce resources, hence requiring a replacement catalyst material. On the other hand, Fe-, Ni-, Mn- or Co-based oxide or hydroxide electrocatalysts have shown efficient and stable O₂ evolution electrocatalysis in alkaline conditions for many decades^[150–153] and have found renewed research focus for renewable energy storage.^[154]

2.2.1. Theory

O₂ evolution is a four-electron oxidation mechanism and proceeds via Equations (9–12) with *OH, *O, and *OOH intermediates (i.e., the reverse of Equations (1–5)). In opposition to O₂ reduction, it is known that O₂ evolution always advances on oxidized surfaces, with strong *OOH adsorption or weak *O adsorption limiting the reaction for studied materials.^[155–157] This allows the free energy for the second charge transfer step (Equation 10) to be identified as a universal single descriptor.^[158]



The reaction intermediates binding experiences the same type of problematic linear scaling relations observed in other electrochemical reactions such as O₂ reduction and CO₂ reduction.^[159] To break the scaling relations, proposed methods include a hydrogen acceptor functionality on oxide surfaces.^[56] The previously mentioned DFT work by Li et al. for dual active site O₂ reduction catalysts in alkaline conditions was also applied to O₂ evolution for a different cofacial separated DAC.^[114] In this case, two cofacial separated CoN₄-C₆₀ catalytic sites within atomic distances were shown to display a very low overpotential of 0.08 V, while a Zn-based macrocycle complex could achieve an ideal overpotential of 0 V. This is achieved at certain atomic distances, for example when 3.75 < Co–Co < 5.75 Å,

intermediates for O₂ evolution (and O₂ reduction) would form **OH, **O, and **OOH structures, circumventing the scaling relationships between traditional intermediates, thus unlocking the possibility for ultralow overpotential.

From an experimental perspective, O₂ evolution catalyst performance is often just measured over one cycle and without methods such as online electrochemistry-mass spectrometry, one cannot confirm whether the current recorded is arising from CO₂ or CO evolution when using an electrocatalyst with a carbon-based support.^[160,161] It remains to be seen whether DAC structures would remain stable at the high potentials required for O₂ evolution.

2.2.2. Experimental

Thus far, there has been limited research conducted on the use of DAC for the sole purpose of O₂ evolution. Hu and co-workers formed a bridged Fe-O₂-Co-N/C DAC via electrochemical deposition,^[58] which displayed an overpotential at 10 mA cm⁻² (η_{10}) of 321 mV (Figure 8), an improvement from the value of 443 mV for Co/N/C (tested in purified KOH). This result supports their hypothesis that Fe doping is required for high activity of Co/N/C. Additionally, the calculated TOF of 12 s⁻¹ at overpotential of 350 mV was comparable in activity to the most active transition metal-based nanomaterial O₂ evolution catalysts in the literature. Following accelerated degradation testing of 3000 cycles the overpotential was found to only rise by 4 mV (at 10 mA cm⁻²). This comprehensive work highlights the potential of highly active DACs for O₂ evolution. Latter works have also shown the efficiency of Ni-Fe sites on polymeric carbon nitride (Ni_{0.65}-Fe₃₅/PCN) for the O₂ evolution.^[65]

2.3. Bifunctional (O₂ Reduction and O₂ Evolution)

Pt group nanoparticles and alloys are considered highly active electrocatalysts for O₂ reduction, while RuO₂ and IrO₂ based

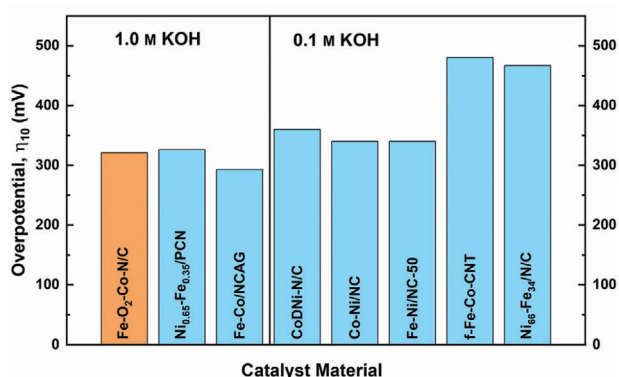


Figure 8. η_{10} of DACs for O₂ evolution in alkaline conditions. The color of the bar indicates the type of DAC suggested to occur in the catalyst material. Blue = in-plane adjacent DAC, orange = in plane bridged DAC. Catalyst loading: Fe-O₂-Co-N/C = 0.381 mg cm⁻²,^[58] Ni_{0.65}-Fe_{0.35}/PCN = 0.268 mg cm⁻²,^[65] Fe-Co/NCAG = 1 mg cm⁻²,^[162] Co/DNi-N/C = 0.3 mg cm⁻²,^[163] Co-Ni/N/C = 0.4 mg cm⁻²,^[164] Fe-Ni/NC-50 = 0.25 mg cm⁻²,^[61] f-Fe-Co-CNT = 0.2 mg cm⁻²,^[165] Ni₆₆-Fe₃₄/N/C = 0.25 mg cm⁻².^[166]

electrocatalysts exhibit the best O₂ evolution activity.^[10,148,149] What these materials do have in common is their low abundance and high cost, making their wide-scale deployment unfeasible, unless the loading of precious metal is sufficiently minimized without compromising catalytic performance.

2.3.1. Theory

The optimum bifunctional catalyst would be able to catalyze O₂ evolution and O₂ reduction at potentials close to equilibrium; however, owing to the scaling relations in O₂ evolution and O₂ reduction, there is no experimental catalyst able to conduct these reactions without an overpotential.^[56] The issue with bifunctional catalysts is the differing characteristics required for optimum performance in each direction of the reaction. To graphically address this, Busch et al. developed double volcano plots for bifunctional ORR and OER to demonstrate the limitations of traditional M/N/C (M = metal) SACs and pure metal or alloy surfaces (Figure 9), whereby large overpotentials are required in both reactions.^[56] Delving into the issue, they found the binding of *OH and *OOH created the catalytic inefficiencies, which could be theoretically overcome by binuclear mechanisms whereby a second nearby cofacial active site possesses a proton donor for O₂ reduction, or proton acceptor for O₂ evolution (Figure 9). Interestingly, their results presented Mn in either a pyrrolic or pyridinic macrocycle with outer bound NH₃ as top candidates for overcoming the scaling relations. Busch et al. highlighted that the oxidation of ammonia to an amino group may be possible at O₂ evolution and O₂ reduction potentials.^[56] Another important caveat mentioned by the authors is the practicality of controllably synthesizing such sites.^[56]

Zhao et al. also theoretically explored locally modifying catalytic sites with hydroxyl groups, although for in-plane adjacent DACs and SACs under alkaline conditions on defective graphene (denoted as (HO)₂-M¹-M²/DG, where M¹ and M² are Ni, Co, or Fe).^[167] The addition of a hydroxyl group was shown to raise activity towards O₂ reduction for the DACs, explained by the increased oxidation states of the transition metals'. In contrast, bifunctional SAC Ni/DG, which formed the lowest overpotential of all considered catalysts, could not exist as HO-Ni/DG since reaction intermediates could not be adsorbed stably under reaction conditions.^[168]

From an experimental perspective, for composite electrodes made from the current state-of-the-art bifunctional Pt/IrO_x, degradation is soon observed due to the required potential cycling range.^[168] If one made a truly reversible O₂ reduction and evolution DAC with low overpotential (<0.3 V), the smaller operational potential range may enable stability in acid. Inspiration for design of bifunctional DACs can be taken from Figure 9, although as Busch et al. stated, the stability of such precise sites under harsh OER conditions is not considered during their DFT analysis.^[56]

2.3.2. Experimental

There have been several experimental demonstrations of in-plane adjacent DACs consisting of Ni, Fe or Co metal centers with bifunctional O₂ evolution/O₂ reduction activity.^[61,163,164,166]

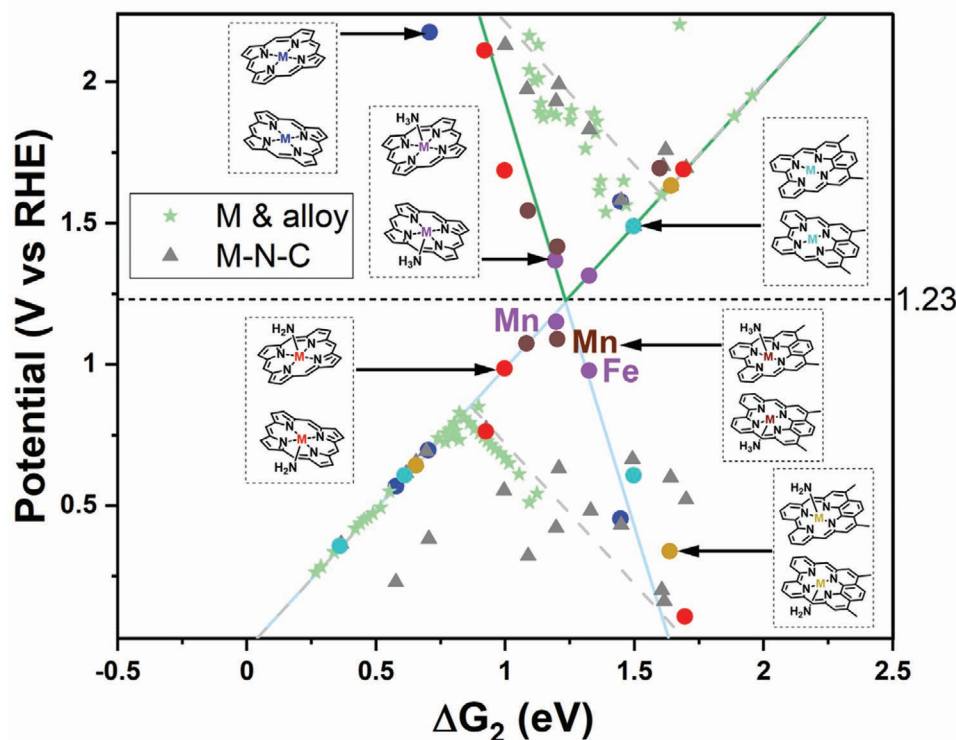


Figure 9. Potential versus ΔG_2 ($=G_{\text{O}} - G_{\text{OH}}$) with calculated volcano plots for ORR (light blue) and OER (green) where the second active site possesses a proton donor ($^*\text{OH}$) or acceptor group ($^*\text{O}$) for O_2 reduction or evolution, respectively. Grey dashed lines show scaling limitations of $^*\text{OH}$ and $^*\text{OOH}$. Based on reference [56].

Chen et al. provided an example of how advantageous traits of individual elements can be combined to create an improved bifunctional DAC.^[162] By combining Fe atoms, known for high O_2 reduction activity, with Co, known for excellent O_2 reduction stability and O_2 evolution activity, a highly active bifunctional adjacent Fe–Co site based DAC was produced from an N-doped carbon aerogel (Fe–Co/NCAG), which exceeded the properties of monometallic counterparts. Of all the DACs synthesized so far, the Fe–Co/NCAG DAC realized the lowest O_2 evolution η_{10} of 293 mV (Figure 8) and the lowest change in overpotential between O_2 reduction/ O_2 evolution of 0.64 V, which was even lower than the benchmark catalysts of Pt/C and RuO_2 (0.70 V). Stability was assessed by 1000 cycles in a Zn–air battery, which in the future could be extended to truly ascertain the catalyst stability.

2.4. CO_2 Reduction

The conversion of CO_2 into valuable products is an attractive solution to fight the rising atmospheric CO_2 concentrations and its detrimental impact on the environment.^[169] The conversion of CO_2 to industrially relevant chemical precursors (such as CO, CH_4 , CH_3OH and longer carbon chains) and can be achieved electrochemically in ambient conditions via the CO_2 reduction process.^[170] Au and Ag are active towards CO formation,^[171,172] Sn toward formic acid/formate,^[173] while Cu metal has been known since 1989 to yield hydrocarbons.^[174] CO_2 electrolyzers based on these metals are becoming commercially available,^[175]

with targets and a roadmap towards technoeconomic viability of CO_2 reduction products recently outlined, which can be applied from lab to commercial scale.^[176] To reach these targets, SACs can display high electrocatalytic performance, although they are typically limited to reactions involving a single molecule.^[177] For complex reactions such as CO_2 reduction, improved performance can potentially be created by more complex atomically dispersed catalysts, for instance, DACs.

2.4.1. Theory

H_2 evolution is the major competing reaction to CO_2 reduction, hence catalysts must display high selectivity toward CO_2 reduction products, in addition to stability and activity.^[178] CO_2 reduction is a multielectron–proton transfer process involving a multitude of reaction intermediates such as $^*\text{COOH}/^*\text{CHO}$ and $^*\text{CO}$ for the simplest pathway, making the overall reaction more complex.^[179] Scaling relationships between these reaction intermediates on electrocatalysts also exist for CO_2 reduction and due to the high number of intermediates, it becomes difficult to tune the adsorption of one intermediate without affecting the adsorption energy of other intermediates.^[179] In this regard, the nitrogenase enzyme has attracted plenty of attention, as it is the only system found in nature that can convert CO_2 to multicarbon products (such as ethane, ethylene, propene, and more) through C–C coupling reactions.^[180–182] This is due to the fact that the catalytic active site of nitrogenase (based on a Fe DAC— Figure 1d) enables the further

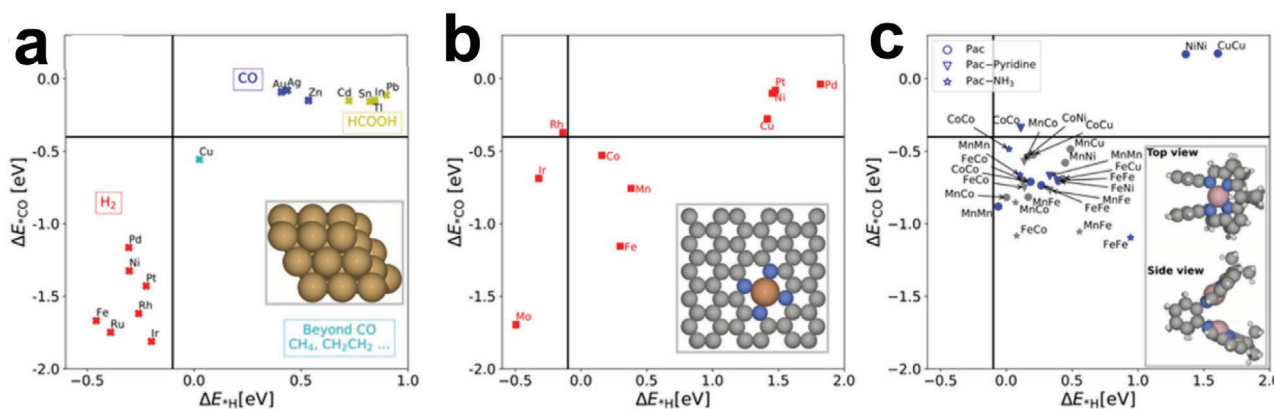


Figure 10. Adsorption energies of CO_2 reduction intermediates $\ast\text{CO}$ and $\ast\text{H}$ on a) Pure metals (structure inset). b) $\text{M}/\text{N}_4/\text{C}$ (M = metal) (structure inset). c) Pacman structures consisting of a separated cofacial DAC connected via a benzene ring (structure inset). Colors: Gold = Cu, Orange = Fe, Pink = Co, Gray = C, Blue = N, Red = O, and White = H.. Solid black line represents thermodynamic boundary for adsorbed or nonadsorbed hydrogen. Reproduced with permission.^[57] Copyright 2021, American Chemical Society. Original data in refs. a)^[188] and b).^[189]

reduction of CO to hydrocarbons and oxygenates through a bridged adsorption of CO_2 , which also occurs in carbon monoxide dehydrogenase (Figure 1c), one of the most efficient CO_2 reduction catalysts.^[183,184] Unlike nitrogenase, Fe-based single atoms are subjected to scaling relationships; Strasser and co-workers have analyzed $\text{M}/\text{N}/\text{C}$ (M = metal atom)^[185] and in particular $\text{Fe}/\text{N}/\text{C}$ SAC^[25] which present efficient conversion of CO_2 to CO ; however, the single sites are not favorable for $\ast\text{CO}$ and $\ast\text{H}$ co-adsorption for conversion beyond CO .^[25,185] This has limited the theoretically predicted and experimental observed electrocatalytic performance of most SACs to just CO ,^[186] while the production of higher added value products such as C_2 (e.g., EtOH), C_3 (e.g., $n\text{PrOH}$) and other desirable hydrogenated carbon chains used as chemical feedstocks, transportation fuels, and electricity generation, remains a challenge.^[183,99] Strasser's group suggested DACs would enable the hydrocarbon production on their $\text{Fe}/\text{N}/\text{C}$ catalyst by allowing rapid protonation of adsorbed CO within a twin site.^[25]

Based on $\ast\text{CO}$ and $\ast\text{H}$ adsorption, Rossmeisl and co-workers developed Figure 10a–c to enable clear comparison between pure metals, SACs, and separated cofacial Pacman DAC.^[57] Figure 10a demonstrates Cu metal uniquely being able to produce CO_2 reduction products beyond CO , owing to its intermediate $\ast\text{CO}$ and $\ast\text{H}$ adsorption strength.^[57] In comparison to pure metals, porphyrin structured SACs exhibit differences, such as the $\text{Fe}/\text{N}_4/\text{C}$ enabling efficient CO production without H_2 formation, owing to destabilization of $\ast\text{H}$ (Figure 10b).^[57] However, compared to Cu metal, SACs based on Fe, Mn, or Co exhibit low selectivity to C_1 product and cannot produce C_2 species (Figure 10b).^[57] Interestingly, Cu- N_4 SACs were predicted to produce CO as the main product.^[57] Meanwhile, they found nearly all Pacman structures owned favorable $\ast\text{H}$ (weak) and $\ast\text{CO}$ (moderate) adsorption and many can produce desirable C_1 or C_2 products (Figure 10c).^[57]

Sun and co-workers found in-plane adjacent DAC on graphene enhanced the stabilization of $\ast\text{COOH}$ and $\ast\text{CHO}$ intermediates, while simultaneously reducing the adsorption energy of CO , thereby breaking scaling relations.^[187] Their models suggested O and OH adsorption energies scaled linearly for the metal dimers on graphene, suggesting E_{ad} (O) as a single

descriptor to determine CH_3OH to CH_4 preference and also estimating OH blockage. For instance, by replacing Mn–Cu dimers with Ni–Cu, selectivity changes from CH_4 production to CH_3OH , owing to the difference in oxophilicity between Mn and Ni. Interestingly, for both Mn–Cu and Ni–Cu dimers it was shown $\text{C}\ast\text{OH}$ was stabilized with respect to $\text{C}\ast\text{O}$.

Following this, Sun and co-workers explored phthalocyanine sheets with various 3d transition metal in-plane adjacent DACs and found Mn_2Pc displayed the best electrocatalytic performance for CH_3OH synthesis.^[190] This was due to the Mn dimer significantly lowering the reaction activation energy and the neighboring Mn atoms assisting in the bonding of the $\ast\text{COOH}$ intermediate, which was considered the rate-limiting step. Furthermore, the Mn–C–O–Mn bridge adsorption, similar to carbon monoxide dehydrogenase,^[184] promotes metal-to-adsorbate π -back bonding leading to easy transitioning between C-end to O-end adsorbate with reduced energy in CH_3OH desorption. Experimentally synthesized rectangular-shape expanded Pc containing Mo or W dimers have previously been reported in literature,^[191] suggesting these highly active metal moieties could potentially be produced. Whether the presented structures would be stable under real CO_2 reduction operating conditions remains to be seen.

2.4.2. Experimental

Early indication of DAC electrocatalytic activity towards CO_2 reduction was found by Enoki et al. with a cofacial separated Co diporphyrin, which displayed catalytic activity over twice that of the mononuclear complex.^[192] More recently, Ren et al. found that, for CO_2 reduction, Ni/ N/C SAC possessed high current density for production of CO ; however, the catalytic sites were limited by sluggish kinetics in the first CO_2 reduction step of the first proton-coupled electron transfer.^[52] In comparison, $\text{Fe}/\text{N}/\text{C}$ SAC displayed desirable low onset potential, although the CO product on these sites binds too strongly, thereby limiting its desorption and hence reactivity of the sites. To tackle the individual issues, Ren et al. generated in-plane adjacent Ni– $\text{Fe}/\text{N}/\text{C}$ DAC sites, which were able to achieve improved

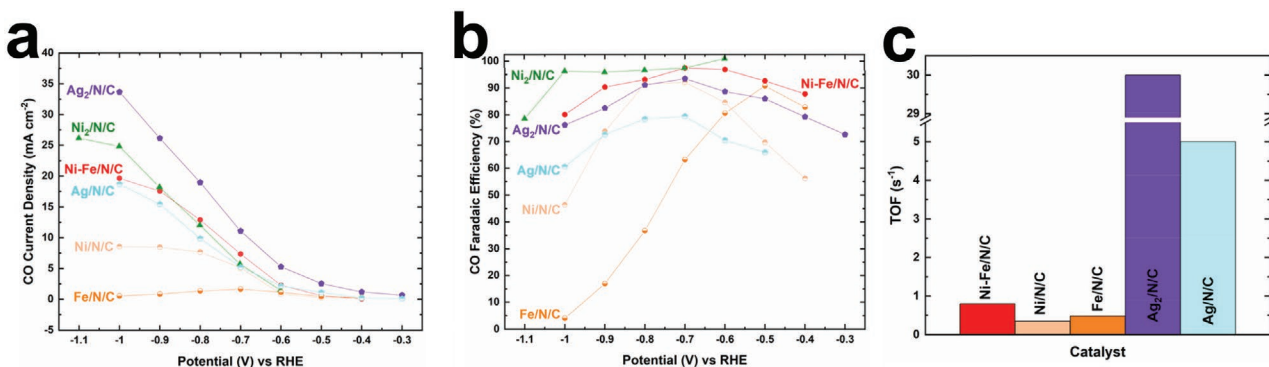


Figure 11. Results for in-plane adjacent DACs and SAC counterparts at various applied potentials against. a) CO Faradaic efficiency and b) partial current density. c) TOF for CO production at 0.7 V (vs RHE). All catalysts tested in H-cell setups with 0.5 M KHCO₃ electrolyte and catalyst loadings of either 0.5 mg cm⁻² (Ni-Fe/N/C, Ni/N/C, and Fe/N/C), 0.3 mg cm⁻² (Ni₂/N/C),^[193] or 0.2 mg cm⁻² (Ag₂/N/C and Ag/N/C).^[195]

CO Faradaic efficiency and current density (Figure 11a,b). The improved intrinsic activity of the Ni-Fe/N/C DAC compared to its SAC counterparts is also highlighted in Figure 11c. The CO₂ reduction mechanism of the Ni-Fe/N/C catalyst was evaluated via DFT analysis, which attributed the enhanced performance to the geometric structure of the DAC, which allowed CO₂ molecules to be adsorbed on one metal site and the COOH intermediate to dissociate on the second metal site. Sun et al. recently observed their Ni₂/N/C catalyst containing potential in-plane adjacent Ni₂ sites presented favorable CO Faradaic efficiency (Figure 11a).^[193] The one-pot pyrolysis process for forming Ni₂/N/C was claimed to be achieved by tuning the amount and binding strength of nitrogen sources,^[193] although the formation mechanism and characterization of the catalytic sites are so far limited. A separate Ni₂/N/C catalyst has also been tested in a flow cell configuration for CO₂ reduction, enabling higher CO current density.^[194] Meanwhile, precious metal-based in-plane adjacent Ag₂/N/C DACs for CO₂ reduction have been created by Li et al. (Section 3.1.2).^[195] Promisingly, TOF values for CO production were ~6 times greater for the Ag DAC compared to separately synthesized Ag/N/C SAC (Figure 11c).

To the best of our knowledge, the limited experimentally synthesized DACs have to date only shown high selectivity towards CO formation (Figure 11). This signifies scope to experimentally explore other geometrical configuration of DACs such as cofacial separated sites to form alternative more desirable longer carbon chain products, taking on board the lessons learnt from theoretical insights. Other potential configurations include nearby single-atom sites. For instance, nearby single atom Cu active sites (similar to CuPc) have obtained Faradaic efficiency of 50% from CO₂ to CH₄.^[196] This was through a proposed mechanism of *CO on one metal atom site desorbing, migrating, and then dimerizing with the *CO intermediate on a C₂H₄-producing site (second metal site), thus resulting in a lower C–C dimerization energy barrier.^[196] Another Cu SAC has even recorded acetone as a major product.^[197] Meanwhile, efficient dynamic catalyst sites may even exist, for instance, an initially single atom Cu sites displayed 55% Faradaic yield of ethanol (with recycling) due to the proposed mechanism of the Cu atoms being able to reversibly form Cu nanoparticle catalytic sites under reaction

conditions, according to operando X-ray absorption spectroscopy (XAS) (Section 4.2.1).^[198]

2.5. N₂ Reduction

NH₃ production is currently carried out in industry through the Haber-Bosch process. This process allowed the growth of society in the last century and continues to be widely exploited due to the high demand of NH₃ worldwide as an energy carrier or fertilizer. Nevertheless, due to the thermodynamic requirements of the reaction, along with extensive CO₂ emissions resulting from methane steam reforming, this process utilizes around 1% of the global energy consumption and produces 1.4% of the global CO₂ emissions.^[199,200] To face the challenge of producing such a vastly utilized chemical like NH₃ via a less energy-intensive approach, electrochemical N₂ fixation (or nitrogen reduction reaction, N₂ reduction) has emerged as a suitable alternative.^[201,202]

2.5.1. Theory

N₂ reduction to NH₃ occurs in nature on the nitrogenase enzyme, with a Mo-Fe-S cofactor consisting of two Fe atoms at the catalytic center. They^[180] high Faradaic selectivity at around 60%, and high rates (on a per site basis: see Figure 1e); the selectivity is due to the restricted access of electrons and the hydrophobic environment around the cofactor which minimizes the proton transport towards the active site.^[31] The Faradaic efficiency is constrained by scaling between the sole intermediate of H₂ evolution, *H and *N₂.^[180] The rates are also constrained by scaling between the N-containing intermediates *N₂, *NH₂, and *N₂H, etc.^[203] Approaches for reducing the proton concentration in the vicinity of the active site have been reported, such as the utilization of a lithium mediated system in organic electrolyte,^[47,204,205] or employing proton-filtering materials.^[206] However, materials that emulate the active principle of the natural nitrogenase enzyme, which displays Fe DAC embedded in a matrix of sulfur atoms (Figure 1c), have still not been realized.

These DAC structures have been shown by Nørskov and co-workers, through theoretical calculations, to enable an efficient

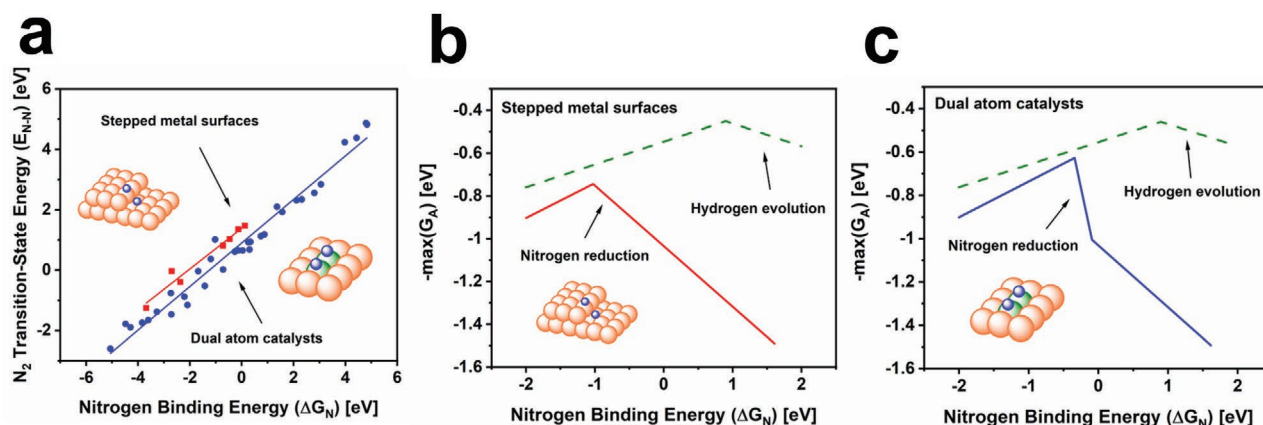


Figure 12. a) Nitrogen transition state energy versus dissociation energy in stepped surfaces (red squares) and dual atom catalysts (blue circles). Based on references [23,208]. b) Activation barrier for N_2 reduction (red line) and hydrogen evolution (dashed green line) on stepped metal surfaces at -0.5 V versus RHE and c) Activation barrier for N_2 reduction (blue line) and hydrogen evolution (dashed green line) for dual atom catalysts at -0.5 V versus RHE. Based on reference [209].

thermochemical NH_3 production under benign conditions due to the improved transition state behavior.^[23] Their results showed that Re stripes of different lengths within a Cu (211) metal lattice lowered dissociation barriers for N_2 , consequently breaking the transition-state scaling relationship between E_{N-N} and $2G_N$ (Figure 12a). Overcoming scaling relationships employing DAC that force on top binding of $*N$ can therefore lead to a higher predicted activity (Figure 12b,c).^[207]

As previously mentioned, carbon materials are ideal candidates to support DAC with improved transition scaling relationships for N_2 reduction, due to their polymeric structure, potentially sustainable character, robustness, low price, and the feasibility to tailor their chemical composition and electronic structure.^[209] In particular, the modification of their structure through heteroatom doping can induce a rearrangement of the charge density and distribution around neighboring carbon atoms, promoting the binding toward reactant molecules.^[210] Particularly, C_2N displays a lone electron pair in their pyrazine moieties as well as a “hole” within the 2D structure^[211] which prevents the agglomeration of transition metal atoms, resulting in SACs and DACs.^[212] Therefore, the tailored design of transition metal DAC- C_2N hybrids (TM₂- C_2N) can potentially lead to the emulation of the active principle of the nitrogenase enzyme, allowing an efficient interaction with N_2 molecules and subsequent hydrogenation with improved transition scaling relationships, as predicted by DFT calculations.^[213,214]

Despite further theoretical studies reporting the efficiency of DACs and related metallic structures on different supports for the N_2 reduction,^[215,216] to date there is no experimental report with a rigorous testing protocol^[217,218] confirming the enhanced electrocatalytic activity of these systems.

3. Synthesis Techniques

Synthetic techniques with atomic precision that allow the reliable production of DAC are highly sought after. So far, methods of producing DAC have included high-temperature pyrolysis, deposition techniques, and wet-chemistry approaches, with

these methods further broken down in Figure 13. The benefits and drawbacks of some of these methods are also summarized in Table 2. It should be noted that entirely pure DACs have yet to be obtained, as a certain minority or even majority of single metal sites can be typically found within these catalysts. Some methods described in this section have not been used to synthesize catalysts for electrochemical reactions; however, they may prove a useful synthesis strategy or inspiration for electrocatalysts in the future. It is also worth briefly mentioning here some best practice during synthesis. For instance, checking the purity of precursors and solvents and their potential contaminants,^[223] preventing cross-contamination, especially in the case of PGM versus non-PGM studies. Where electrochemical methods are used, rigorous electrochemical procedures are required, including cleaning and use of high purity electrolyte.^[224]

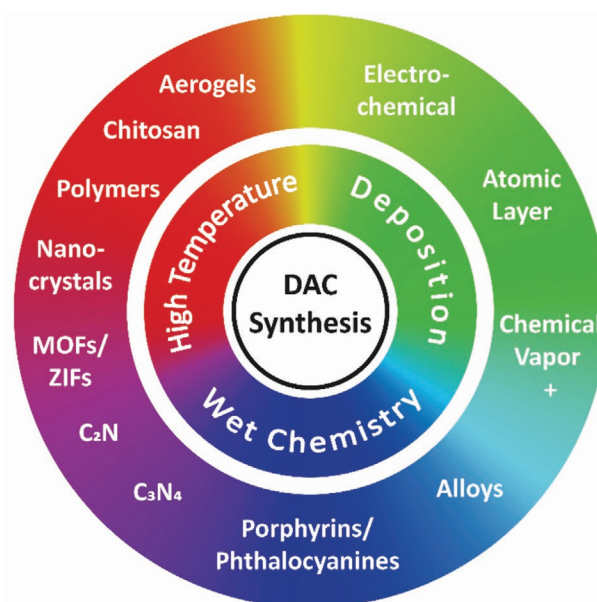


Figure 13. Summary of synthesis techniques for forming DACs.

Table 2. Selected list of methods for DACs synthesis.

Method	Advantages	Disadvantages	Supports	Examples	Refs.
MOF/ZIF pyrolysis	High metal loading, tunable size	High temperature, mixed active sites, encapsulation results in low active metal loading	N-doped carbon/carbon nanotubes	Fe-Co/N/C, Fe-Co/CNT, Fe ₂ /N/C	[38,49,68]
Chemical vapor deposition	Scalable (mass production)	Requires additional treatment steps, high temperature	N-doped graphene, graphene	W ₁ Mo ₁ -NG, Fe ₂ /graphene	[59,219]
Atomic layer Deposition	Atomic control, uniform thickness	Expensive, slow deposition rate, low yield, scalability	Graphene, N-doped carbon nanotubes	Pt ₂ graphene, Pt-Ru/NCNTs	[19,75]
Wet Chemistry	Variety of metallic moieties, no specialized equipment	Low metal loading/aggregation, attachment to conductive support, stability	Inorganic substrates/carbon	Zn-Zn or Co-Co with molecular clips, Pacman Co-Co	[35,36]
Electrochemical deposition	Basic electrochemical setup, simple process, all sites electrochemically accessible	Oxide formation, low metal loading, require SAC on N-doped carbon initial SAC		Fe-O ₂ -Co-N/C, A-CoPt/N/C	[58,220]

3.1. High Temperature

High-temperature treatment has so far been the most common synthesis technique to produce DACs and their associated support. However, this method invariably results in an array of different catalytic site structures due to the instability of the precursors at these highly elevated temperatures and, as a result, acid etching processes are usually required.^[223] Hence, the pyrolysis temperature, which for DAC usually ranges from ≈700- to 1000 °C, and selection of atmosphere, typically N₂, Ar, H₂, NH₃, or mixtures, are both crucial in controlling the catalyst composition and morphology and therefore its activity and stability.^[49,52,68,224] High-temperature pyrolysis can be split into two categories, depending on whether the metal is contained within specific complexes (mainly MOF-based precursors) or irregular complexes such as biological precursor. To produce nitrogen coordinated DACs or few-atom cluster catalysts, one-pot strategies where metal-nitrogen binding takes place during pyrolysis are preferred due to the competition of metal atom aggregation by metal-nitrogen binding.^[193] It is known for SACs such as FeN₄, the high temperature used in their materialization causes condensation of the metal sites into undesirable nanoparticle formation, limiting loadings to typically remaining below 1–2 wt%.^[21,22]

3.1.1. ZIF/MOF

MOFs are made up of metal nodes interconnected by organic linkers which can create a variety of nanoporous materials of different structures. While MOFs have demonstrated intrinsic activity for electrocatalytic application,^[225] they can often suffer from charge transfer and stability issues.^[226] Zeolitic imidazolate frameworks (ZIFs) are a subcategory of MOFs which can act as sacrificial templates, molecular-scale cages or porous metal-containing N-doped carbon materials.^[227] This makes ZIFs ideal for deriving highly active DACs, owing to their abundant pores, large surface area, and adaptability for composition and structural manipulation.^[228,229] In particular, ZIF-8, formed using 2-methylimidazole and hydrated Zn nitrate precursors, have proven themselves as a method for producing

in-plane adjacent DACs by encapsulation of a metal precursor (Figure 14).

Wang and co-workers were first to claim a route to heterogeneous in-plane adjacent DACs, whereby a bimetallic MOF, similar to ZIF-8, containing Zn and Co was used to encapsulate FeCl₃ molecules by a double solvent method, as shown in Figure 14a.^[49] The comparatively volatile Zn was suggested to evaporate and be replaced by Fe ions, forming a suggested Fe-Co DAC, according to HAADF-STEM and ⁵⁷Fe Mössbauer measurements prior to electrochemical testing and post-mortem EXAFS. Wang et al. modified the Fe-Co DAC synthesis with CNT in subsequent work.^[38] Meanwhile, Ye et al. were able to in situ encapsulate Fe(acac)₂, Fe₂(CO)₉ (Figure 14b) or Fe₃(CO)₁₂ precursors inside ZIF-8 cavities. Subsequent pyrolysis and evaporation of Zn allowed the Fe cluster attachment to the N-doped carbon, resulting in Fe₁-N/C, Fe₂-N/C or Fe₃-N/C sites.^[68] The downside to this encapsulation process is the relatively low content of the desired Fe metal. Plenty of other examples exist utilizing the functionality of ZIFs (ZIF-8, ZIF-67) to produce in-plane adjacent DACs for electrochemical reactions.^[52,125,163,230,231]

One comment on both ZIF-8 based methods reported above (and in many other reports) is the lack of confirmation or acknowledgment of unconverted Zn atoms which may form (usually inactive) SAC or part of DAC sites. Differentiating between Zn-Co and Fe-Co sites via HAADF-STEM does not seem feasible. Analysis by inductively coupled plasma techniques (Section 4.2.6) would provide quick confirmation of any surviving Zn.

A current drawback of one-step pyrolytic methods is the limited loading of active metal and therefore active-site density.^[232] Additionally, for certain metals such as iron, high concentrations trigger the formation of undesirable nanoparticles, carbides, and nitrides via carbothermal reduction at high temperatures ($T > 550$ °C for iron carbides).^[232,233] Encapsulation methods (Figure 14) may prevent metal agglomeration but this also inherently limits metal loading. Decoupling the high temperature pyrolytic treatment and active metal loading steps on a templated site, as first described by Fellingner et al.,^[232,234] enables a more controlled and high loading SAC. This active site templating and transmetalation approach was developed

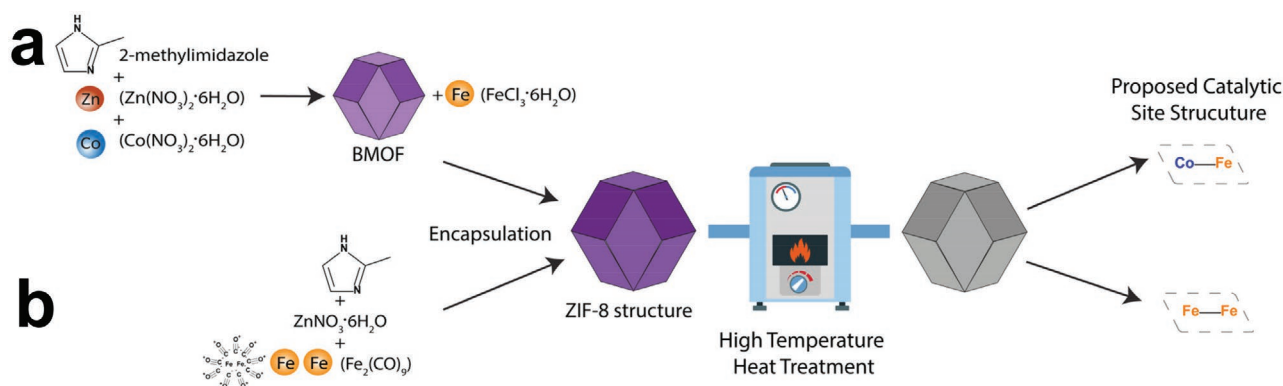


Figure 14. Schematic illustrations of DAC formation from ZIFs. a) Preparation of Fe-Co DAC on N-doped carbon from BMOF by Wang and co-workers.^[49] b) Preparation of Fe-Fe DAC via encapsulation in ZIF-8 by Ye et al.^[68] Gray dashed lines represent the local support environment of the metal atoms.

further using chemical vapor deposition (Section 3.2.2) on a pyrolyzed ZIF-8 to create unprecedented Fe/N/C SAC activity in the cathode of a H₂-O₂ proton exchange membrane fuel cell.^[55] This promising two-step approach could potentially be used to create DACs, providing a suitable templated site is first created.

3.1.2. Alternative High-Temperature Methods

Examples of alternative methods for producing DACs via high-temperature methods are discussed below; however, these

techniques have resulted in a mixture of SACs and DACs with varying controllability of synthesis.

Lu et al. first demonstrated chitosan could be used as a precursor to form an O₂ reduction active Zn-Co DAC, due to the naturally rich network of amine groups in chitosan (Figure 15a).^[50] They suggested a competitive complexation strategy, whereby 4s and 4p electrons of Co²⁺ and Zn²⁺ coordinate to the naturally occurring -NH₂ and -OH groups in chitosan, resulting in a homogeneous distribution of Zn-Co sites according to pre-electrochemical testing HAADF-STEM and XAS. Soon after, Liu et al. also proved chitosan could be used to create similar O₂ reduction active Zn-Co sites in a S-doped NC support

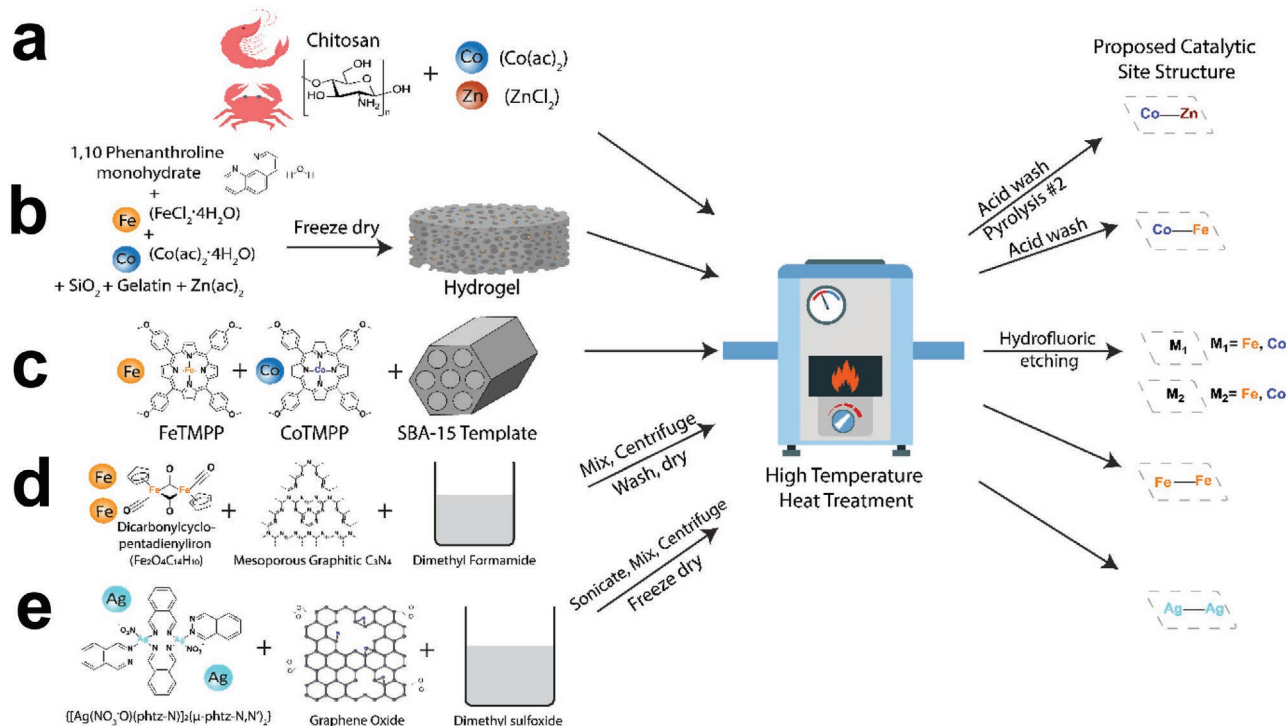


Figure 15. Schematic illustration of alternative high-temperature methods for DAC formation. a) Chitosan-derived in-plane adjacent Zn-Co DAC by Lu et al.^[50] b) Aerogel-derived in-plane adjacent Fe-Co DAC by Chen et al.^[63] c) SBA-15-derived cofacial separated Fe-Co DAC by Joo and co-workers.^[34] d) Carbon nitride (C₃N₄) derived DAC used for alkene epoxidation by Tian et al.^[237] e) In-plane adjacent Ag-Ag DAC derived from graphene and dual-Ag precursors by Li et al.^[194]

(Zn–Co–N_x–C–S_y).^[230] While chitosan is valued as a sustainable bioderived precursor, whether it can be used for well-controlled formation of DAC sites in the presented methods remains debatable.

In a separate synthesis method, a porous N-doped carbon aerogel was utilized to host sites for orthogonal plane N₃Fe–CoN₃ DAC, according to pre-electrochemical testing XAS, for bifunctional O₂ reduction/O₂ evolution (Figure 15b).^[163] This method lacks the controllable synthesis of pure DAC owing to the varying structure of the N-doped carbon support and the indication that micropores serve as the main host of Fe–Co sites.

Joo's group synthesized Fe–Co ordered mesoporous porphyrinic carbons (Fe–Co/OMC), using SBA-15 as a template, while FeTMPP and CoTMPP served as a metal, N and C source (Figure 15c).^[134] Metallic nanoparticles were observed under transmission electron microscopy (TEM) following pyrolysis; however, these were removed following HF washing of the SBA-15 template, with some cofacial separated DAC potentially forming according to pre-electrochemical testing XAS. There was no control over the positions of the metal centers, aside from being restricted in the radial direction of the pores, therefore remaining single metal sites may not have aligned in cofacial positions. Conversely, since the SBA-15 was coated purely with FeTMPP and CoTMPP it is likely some metal centers aligned into cofacial separated DACs. To help align the sites, the FeTMPP and CoTMPP precursors could in future be bridged by an atom in the axial plane before inserting into the SBA-15 template, with the bridging atom removed during pyrolysis.

So far, the high-temperature methods presented in this section may lead to some DAC sites; however, the required post-treatment suggests a need to remove undesirable pyrolysis products such as metallic nanoparticles and oxides. Tian et al. developed a rational process of using mesoporous carbon nitride (C₃N₄) with a diiron precursor which did not require treatment post-pyrolysis (Figure 15d). Similar C₃N₄-derived materials have been used for non-electrocatalytic application of DAC but can provide synthetic inspiration.^[236,237] To improve conductivity for electrocatalytic DACs, the C₃N₄ containing catalyst can be placed over carbon nanotubes, as demonstrated by Liu et al. for OER.^[66] Although, using both Ni and Fe precursors, similar to Wu et al.^[65] likely results in a distribution of catalytic sites. Meanwhile, Li et al.^[194] used graphene oxide as a support for molecular-derived dual-Ag atoms^[238] and subsequently used the catalyst for CO₂ reduction without post-pyrolysis treatment (Figure 15e). Still, this method demands well-defined defects within the graphene oxide for DAC formation. What remains undefined from the methods outlined above is the rational design of heteronuclear DACs which can be produced in a controllable way. Most likely to solve this issue, sequential methods such as encapsulation (Figure 14), active site templating, or deposition (Section 3.2) are likely required.

3.2. Deposition

3.2.1. Atomic Layer Deposition

ALD enables finely controlled and reproducible build-up of atomic layers on high surface area materials at relatively low

temperatures, like CVD except that deposition is divided by sequential self-limiting surface reactions, with each layer separated by inert gas purging. ALD is applicable to high surface area substrates, even those with high aspect ratio indents, with the ALD process historically used extensively in the microelectronics industry, and more recently for catalysis and energy storage.^[239–241] The downsides to ALD are the high equipment cost, slow deposition rate, and the limited number of reagents that can be used for the self-limiting reactions, which commonly include highly toxic precursors (e.g., H₂S) and precious metals precursors. However, this list is continually expanding to include more sustainable and cost-effective precursors, such as base metals.^[242–246] The reasons listed above explain the limited implementation of ALD in common chemistry laboratories and lack of scale-up from laboratory-based research to industry for catalysis. ALD is also very sensitive to operational temperature, typically requiring a trial-and-error approach for successful synthesis.

In its favor, ALD has demonstrated its reliability for the controllable synthesis for DAC, as shown by Yan et al. who reported the formation of Pt dimers separated by oxygen atoms on graphene for the non-electrochemical hydrolytic dehydrogenation of ammonia borane.^[19]

In terms of electrochemical reactions, Pt–Ru dimers were synthesized via ALD, as shown in Figure 16a, on nitrogen-doped carbon nanotubes with a suggested predominant catalytic site coordination of N–Pt–Ru–C₂, which was found to be remarkably efficient for H₂ evolution.^[75] Just below 70% of catalytic sites consisted of Pt–Ru dimers, according to counting 200 sites (pre-electrochemical testing) with HAADF-STEM, with those dimers displaying varying structures, therefore suggesting further work can be done to improve the controllability of DAC formation with ALD, for instance by using a more well-defined N-doped carbon precursor.

3.2.2. Chemical Vapor Deposition Combined with Other Methods

CVD alone is not typically able to precisely tune the film thickness, surface coverage, and morphology of catalysts, therefore is not a typical candidate for the synthesis of SACs or DACs.^[245] Nonetheless, Wu and co-workers demonstrated the ability of CVD to produce SACs (M–N–C where M = Fe, Co, Ni, or Mn) for O₂ reduction.^[247] For DACs synthesis, Yang et al. conducted a prior hydrothermal treatment and freeze-drying process using polyoxometalate precursors containing W and Mo, where the metal atoms were anchored onto partially reduced graphene oxide. Subsequently, CVD treatment formed oxo-linked DACs (Figure 16b) according to HAADF-STEM and XAS prior to pH-universal H₂ evolution testing.^[59] The oxo-linked W–Mo, Mo₂ or W₂ were embedded in N-doped graphene by processing CVD in varying molar ratios and CVD times. The polyoxometalates with variable coordination number and geometry with separated units prevented the metal atoms from agglomerating during the initial hydrothermal treatment.^[59] In a separate system designed for potential application in spintronics, monolayer graphene was produced by CVD on a Cu catalyst; its growth was followed by drop casting FeCl₃ solution as the source of Fe dopant atoms. Interestingly, controlled vacancy sites were then

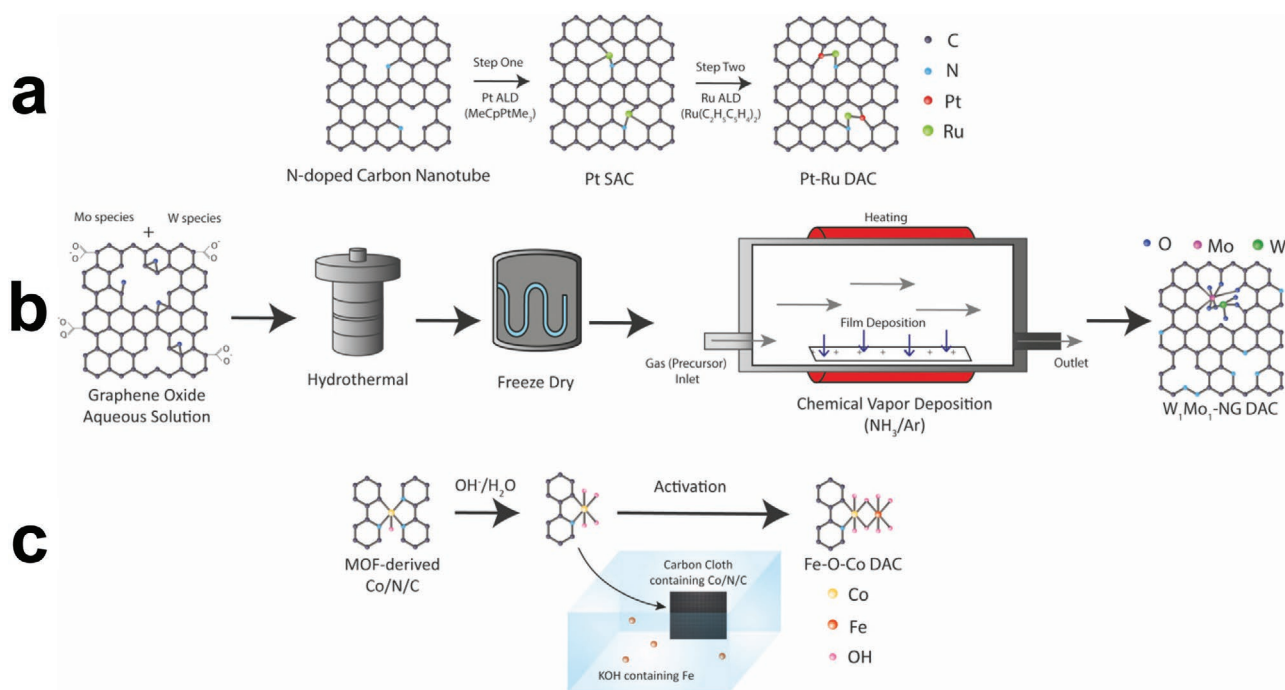


Figure 16. Schematic illustration of deposition procedures for forming DACs. a) ALD synthesis for Pt–Ru dimers on NCNTs. Based on reference [75]. b) W₁Mo₁-NG DAC synthesis including chemical vapor deposition. Based on reference [59]. c) Conventional electrochemical deposition of Fe on MOF-derived Co/N/C to form Fe–Co DACs. Based on reference [58]. In all schemes, atoms are represented as C gray, N light blue, Pt red and Ru light green, O dark blue, Mo purple, W dark green, Co yellow, Fe brown, OH pink.

created using a focused electron beam (80 kV), which resulted in the formation of Fe₂ dimers within the graphene.^[219] These methods serve as examples of how CVD can be used in conjunction with hydrothermal treatment/freeze drying or electron beams to produce the synthesis of DACs.

3.2.3. Electrochemical Deposition

Electrochemical deposition benefits from avoiding the need for high temperatures and binders that arise in methods involving pyrolysis, therefore enabling a low-cost and energy-efficient process. Additionally, by depositing the metal precursors on the outermost surface of supports, maximum utilization of the metal precursor is achieved. Electrochemical deposition can be broken down into two distinct methods. The first is quasi-electrodeposition, considered as a potential cycling method, where the counter electrode contains the atoms to be deposited, which so far has only successfully been employed with Pt.^[62,220,248] By tuning the electrodeposition potential and cycle times, one can accomplish deposition of Pt from counter electrodes to working electrodes in acidic or alkaline conditions with atomic-scale precision.^[249] Zhang et al. utilized this technique for Co-N/C, prepared from Co-MOF as the catalyst at the working electrode and Pt wire for the counter electrode.^[62] Zhang et al. synthesized CoN₄ sites by MOFs pyrolysis then, in order to modify the local electronic structure, they carried out the electrodeposition of Pt atoms onto N₄ sites adjacent to the CoN₄ sites by cycling from 0.1 to 1.1 V (vs RHE). O₂ reduction Co-Pt DAC was observed on N-doped graphitic spheres according to pre-electrochemical

HAADF imaging (referred to as A-Co-Pt/N/C). Following this work, Zhang et al. replicated this technique for a H₂ evolution catalyst.^[222]

The second type of electrodeposition can be considered as conventional electrodeposition, whereby the metal to be deposited is contained within the electrolyte. The naturally slow diffusion rate of metal ions can be controlled by their precursor concentration and enables the deposition of isolated atoms onto the catalyst support. For instance, Hu and co-workers incidentally found Fe impurities in their KOH electrolyte would electrochemically deposit on their Co-N/C SAC, forming a Fe-Co-N/C DAC with oxygen atoms bridging the Fe–Co (Figure 16c).^[58] This method defines a simple approach for the formation of defined and electrochemically active DAC, which could potentially be exploited with other elements of interest as already achieved for other types of catalytic sites.^[250] Additionally, by optimizing the concentration of metal precursor and time for deposition, precise controllability during synthesis may be obtained. The work by Hu and co-workers also highlights the importance of using high purity electrolyte and rigorous electrochemical testing protocols^[224] to prevent potential contamination of catalytic sites.

3.3. Wet Chemistry

Wet chemistry methods benefit from being conducted in common chemistry laboratories, without the need for specialized facilities and equipment, therefore allowing more accessible synthesis routes for researchers and potentially fast route

to upscale, where feasible, in case of promising performance. Isolated atoms and dual atoms possess a higher surface energy compared to nanoparticles, explaining their tendency to aggregate during the synthesis and catalytic processes. Consequently, the interaction between metal atoms and support is crucial in preventing atoms from aggregating and good dispersion of isolated dual atom sites.^[77] Nevertheless, wet-chemical methods typically employ low concentrations of metal precursors in order to limit the formation of metal nanoparticles and clusters. In-plane adjacent transition DACs in C_2N have been predicted by DFT to display beneficial characteristics for various electrocatalytic reactions,^[211,251,252] with a potential ability to host two metal atoms owing to their pore containing N_6 with a diameter of ≈ 8 Å.^[213] Their so far limited synthesis techniques, which has been recently evaluated by Antonietti and co-workers,^[253] should be explored further imminently.

In terms of cofacial DACs, a complex synthetic chemistry route was taken by Mihara et al. to obtain their μ -oxo-dinuclear Fe(III) connected by a flexible fourfold rotaxane (Figure 6c).^[54] More recently, direct formation and high-yield molecular porphyrin-based Co or Zn cofacial separated DACs for O_2 reduction have been achieved by Crawley et al. through coordination-driven self-assembly methods, although Ru-based molecular clips were required (Figure 17a).^[36] Meanwhile, cofacial separated Co-based bisporphyrin dyad resembling a Pacman shape very similar to theoretical catalysts in Figures 5c and 10c has been produced by Cao's group for O_2 reduction (Figure 6d).^[35] These methods of producing molecular cofacial DACs would require functionalization to an appropriately conductive support and be resistive to harsh pH environments for realistic applications in electrochemical reactions.

Directly synthesizing cofacial separated heterogenous DACs requires Angstrom control. One method to achieve this could be obtained by the porphyrinic zirconium MOF (PCN-226(Co)) synthesis exhibited by Huang and co-workers for O_2 reduction (Figure 17b),^[117] which provides an example of tailored active

site spacing (7 Å) with a configuration very similar to that proposed by Sours et al. (Figure 5f).^[115] This suggests similar porphyrin-based MOFs could serve as ideal designs for cofacial separated catalysts for O_2 reduction as well as CO_2 and N_2 reduction, although conductivity and stability of nonpyrolyzed MOFs typically hinder their electrochemical application.

4. Advanced Characterization

As discussed in Section 3, precise controllable synthesis of DACs has been difficult to obtain, for both SACs and DACs while there is a lack of robust characterization methods and algorithms for quantifying the ratios of types of catalytic sites. Consequently, the characterization and differentiation of DACs from SACs are subject to error, with their precise geometric and electronic structure even harder to assess. It is through a suite of complementary characterization techniques, such as those outlined in Figure 18, that one can try to solve these issues and thoroughly examine the geometrical and size dependence of catalysis performance. Thorough characterization is fundamentally important to accurately assess key electrocatalysis metrics such as turnover frequency, which can vary by several orders of magnitude between types of catalytic sites.^[15] Operando measurements are crucial to elucidating stepwise reaction kinetics and short-lived intermediates, which would otherwise be missed from ex situ measurements.^[254] Furthermore, the finely controlled structures of DACs have a tendency to agglomerate and/or change during the electrochemical operating environment, causing deactivation in long-term testing and difficulty in determining key structure-activity/selectivity relationships,^[255] demonstrating the importance of operando measurements.

We hence focus on advanced characterization techniques that can identify DACs from SACs and other types of catalysts. These typically include aberration-corrected scanning transmission electron microscopy (STEM), X-ray absorption

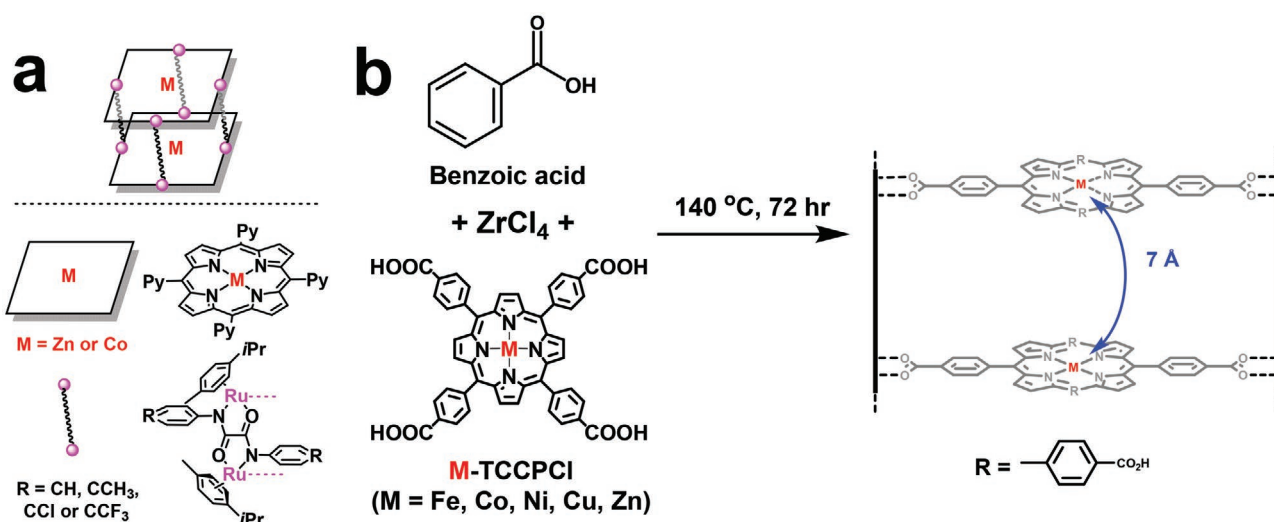


Figure 17. Schematic illustrations showing proposed synthesis of a) Self-assembled separated cofacial DACs using Ru molecular clips with constituents shown. Adapted with permission.^[36] Copyright 2021, American Chemical Society. b) Pacman separated cofacial Co DACs. Adapted with permission.^[35] Copyright 2020, Royal Society of Chemistry. c) Porphyrinic zirconium MOF (PCN-226). Solid black line depicts zirconium chains with composition $[ZrO(-COO)_2]_n$ with Zr atoms hepta-coordinated. Adapted with permission.^[117] Copyright 2020, American Chemical Society.

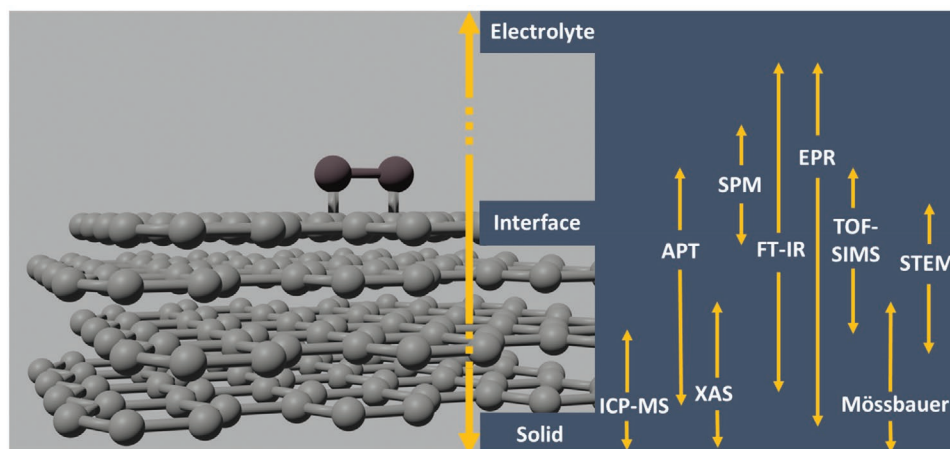


Figure 18. The regions probed by techniques used for characterizing DACs.

spectroscopy (XAS), infrared (IR) spectroscopy, along with other relevant and potential characterization methods also discussed.

4.1. Microscopy

4.1.1. Scanning Transmission Electron Microscopy

Aberration corrected STEM can provide images with atomic resolution, and therefore is able to identify neighboring metal atoms and their atomic distance, while also evaluating the degree of uniformity of the surface species. High-angle annular dark-field (HAADF)-STEM relies on the higher atomic number of the metal atoms in catalytic sites appearing brighter than the lower atomic number of the elements in the catalyst support, which typically consists of carbon and nitrogen. HAADF-STEM has been extensively used to define the two metal centers in DAC,^[50,58,126,163] although they can be hard to distinguish from SAC, especially in amorphous carbon supports, since the atomic distances between the metal centers are at the resolution limit of many HAADF-STEM facilities. This fact has recently led to questionable identification of DACs.

Yan et al.,^[19] angular rotations of identified close proximity Pt atoms under aberration-corrected HAADF-STEM was neatly used as evidence of Pt dimers present rather than just the coincidence of two isolated Pt atoms at different Z positions (Figure 19a,b). One issue they observed was Pt dimers uncoupling and some even departing from the surface due to the high energy of the electron beam (Figure 19b,c). To work with beam-sensitive samples, low-dose and high-speed STEM is becoming possible,^[257] while low-voltage 4D-STEM is another recent advancement that allows imaging of both the high atomic number metal atoms and low atomic number N-doped C plane simultaneously (Figure 19d).^[256] This imaging development will be invaluable in application to dual sites, although at the moment access to these facilities are extremely restricted. Figure 19e–i illustrates other examples of HAADF-STEM images prior to electrochemical testing, where it can be seen a distribution of atomic sites are present along with varying image quality owing to different facility capabilities and noise filtering. Interestingly, Figure 19j provides a rare example of

catalyst imaging post-electrochemical testing, with Ag DACs sites still evident.^[195] More widely adopted postelectrocatalytic imaging is recommended to confirm DACs sites are stable in catalysts. Ideally, in the future, identical location measurements could be obtained to directly compare the same sites before and after testing. HAADF-STEM can be used to quantify numbers of SACs and DACs, as well as TACs, within a catalyst.^[226] Nevertheless, the identification of sites can be open to interpretation and additionally only a small fraction of catalyst can be analyzed with each image, allowing the opportunity for selectivity in the catalyst area chosen. Other issues of using STEM facilities arise from their limited accessibility for many researchers and difficult sample preparation.

STEM can also be combined with other techniques such as electron energy-loss spectroscopy (EELS) to provide mapping of atomic species,^[261] although dose damage is even more problematic in STEM-EELS due to inefficiencies in inelastic core-loss scattering. This could be reduced by advanced data collection and analysis.^[91] Vibrational spectroscopy can complement STEM-EELS by providing unmatched energy resolutions, with the vibrational signature of a single atom defect in graphene recently matched to its observed spectral fine structure.^[259] Eventually, this could be applied to SACs, DACs, and their adsorbed species, assuming computational challenges of 3-D materials for these experiments can be overcome.^[259] For potential in situ or operando measurement in an electrolyte, the adsorbed species might differ from those to a sample that has been transferred through air into the ultrahigh vacuum microscope.

4.1.2. Scanning Probe Microscopy

Electrochemical scanning probe microscopy (EC-SPM) techniques have been able to resolve atomic features on surfaces, even in the harsh conditions of the electrolytes used in the in situ and operando environments.^[264] For instance, electrochemical scanning tunneling microscopy (EC-STM) can resolve catalyst structures on the atomic scale,^[261] although it has not yet been developed in the field of electrocatalysis to determine DACs. However, ultrahigh vacuum STM technique

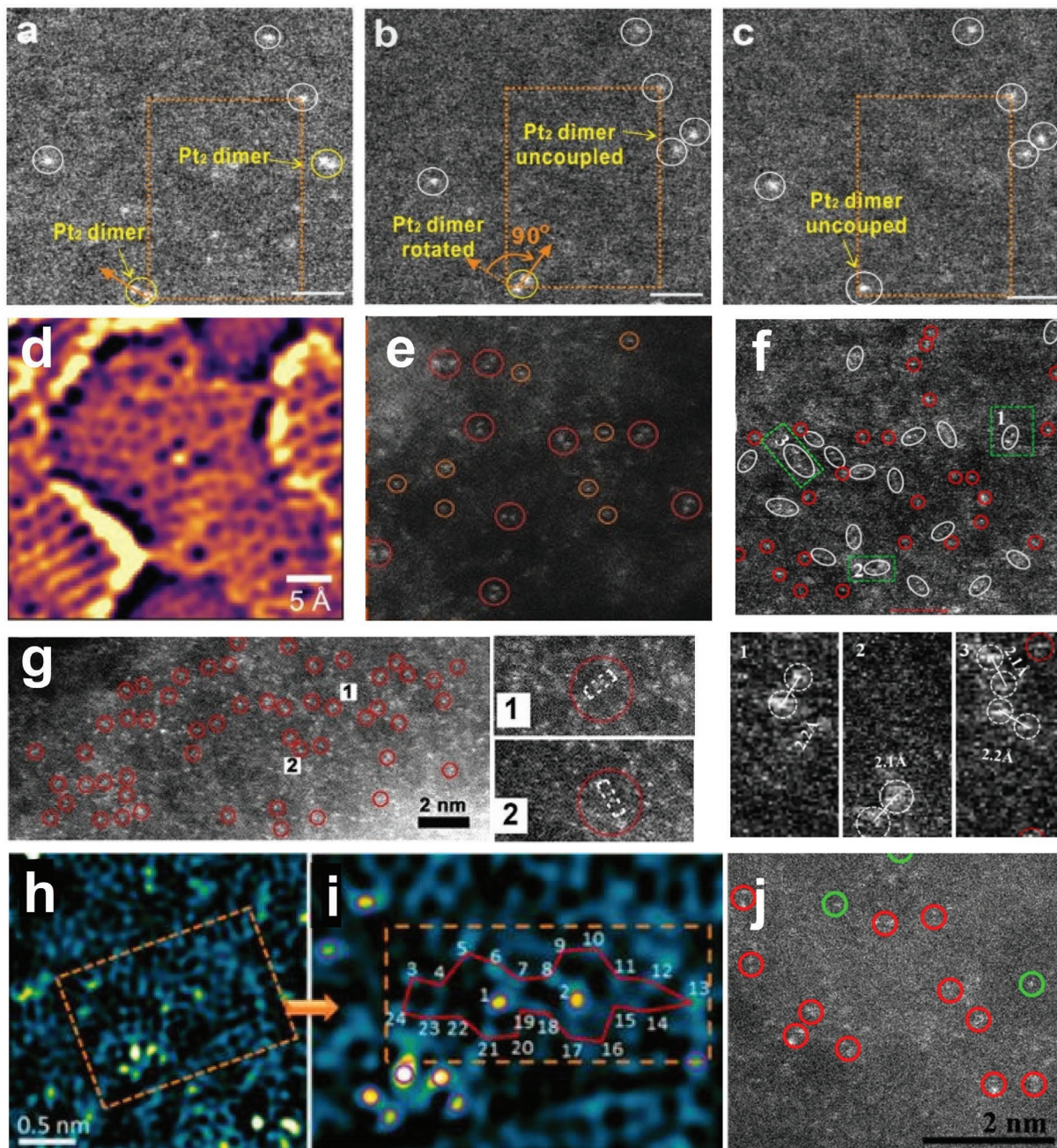


Figure 19. All images were obtained with aberration-corrected HAADF-STEM before electrochemical testing unless otherwise stated. a) Observation of Pt₂ dimers on graphene (synthesized by ALD, Section 3.2.1). b) Observation of Pt₂ dimer rotation and uncoupled Pt₂ dimer. c) Uncoupled Pt₂ dimer. Pt single atoms and dimers are highlighted in white and yellow circles, respectively. Scale bars, 1 nm. All obtained at 200 keV. Reproduced under Creative Commons CC BY license.^[19] Copyright 2017, Nature Publishing Group. d) FeN₄ site in a defective graphene lattice obtained by 4D-STEM with a 30 keV probe. The structure is visualized through the derivative of the center of mass of each diffraction pattern. A ≈0.5 Å Gaussian filter is applied to reduce noise at frequencies significantly higher than the information limit of the instrument. Reproduced with permission.^[259] Copyright 2020, Cambridge University Press. e) Zn-Co/N/C (for synthesis see Figure 15a) with image obtained at 200 keV. Dual sites highlighted by red circles and single sites highlighted by orange circles. Scale bar not provided. Reproduced with permission.^[50] Copyright 2019, Wiley-VCH. f) Co₂/N/C (for synthesis see Figure 14a, without the addition of Fe precursor) with images obtained at 300 kV. Scale bar, 1 nm. Co single atoms and dimers are highlighted in red and white circles, respectively. Highlighted dual sites in green boxes 1, 2, and 3 are enlarged in lower images correspondingly. Reproduced with permission.^[125] Copyright 2018, Elsevier Ltd. g) Fe-Co/N/C (for synthesis see Figure 14a) at 300 kV. Reproduced with permission.^[49] Copyright 2017, American Chemical Society. h) Image of A-CoPt-NC (produced by electrochemical deposition, Section 3.2.3) after fast Fourier transformation filtering obtained at 80 kV. Bright yellow spots are metal atoms, and cyan spots are carbon atoms. i) Partially zoomed-in image of the area framed in h) of Co-Pt DAC. i, h) Reproduced with permission.^[62] Copyright 2018, American Chemical Society. j) Ag₂/N/C (for synthesis see Figure 15e) post catalytic stability test (-0.7 V in the CO₂-saturated electrolyte for 36 h). Red circles ascribed to parallel Ag₂ sites, while green circles assigned to Ag₂ sites aligned with the projection. Images obtained with 120 kV acceleration voltage. Reproduced with permission.^[194] Copyright 2020, Elsevier.

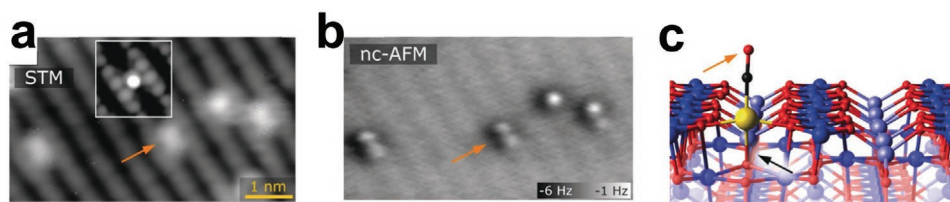


Figure 20. Model $\text{Ir}_1/\text{Fe}_3\text{O}_4$ catalyst after exposure to CO at room temperature. a) STM image showing the majority of Ir_1CO species (Ir adatoms are two-fold coordinated) as elongated protrusions (orange arrow) between bright Fe rows of $\text{Fe}_3\text{O}_4(001)$ support. In a minority of cases a single bright protrusion is observed (inset). b) Noncontact AFM resolving two distinct protrusions of Ir_1CO species (orange arrow). c) Computationally derived illustration of minimum energy structure for Ir_1CO monocarbonyl. Black arrow indicates the additional bond between Ir adatom and O atom in sub-surface layer. Images obtained with 1.5 V sample bias and acquired at 78 K using a CO-functionalized tip. Reproduced under the Creative Commons CC BY license.^[263] Copyright 2019, The Authors.

can distinguish dimer adatoms and their interaction on atomically flat surfaces such as silicon crystals for the semiconductor industry in modern electronic devices. For instance, defined In–Sn heterodimers and In–In homodimers and chains of these on Si(001) have been investigated by STM.^[262] More recently, partially dissociated water dimers on the O_2 evolution active hematite interface were confirmed through non-contact atomic force microscopy (AFM), combined with other techniques.^[263] CO adsorption on model single atom Ir adatoms on a $\text{Fe}_3\text{O}_4(001)$ support was demonstrated by STM, non-contact AFM and DFT (Figure 20a–c),^[260] while in separate work Cu adatoms on the same support was proven by measuring the relative change in height of the Cu before and after CO adsorption via STM.^[264] In situ noise analysis in EC-STM has even been able to identify the active sites present in O_2 reduction and evolution.^[265] This demonstrates the potential of scanning probe and atomic force techniques in characterizing the surface interaction of DACs, assuming developments in sensitivity can continue to be made. However, it should be noted that STM is an incredibly challenging and time-consuming technique which can only be performed on atomically flat surfaces, meaning it is beyond the reach of most researchers (much more so than STEM).

4.1.3. Atom Probe Tomography

Atom probe tomography (APT) can provide 3D constructions of samples containing any element, with a sensitivity in the order of parts per millions and down to sub-nanometer resolution.^[268] Jiang et al.^[266] demonstrate one method of sample

preparation through a nanofabrication “sandwich,” embedding their O_2 reduction Fe-CNT electrocatalyst between layers of Ni, Au and Si and milling a sample tip using a focused ion beam (Figure 21a). Their APT results suggest Fe atoms may directly coordinate to both C and O (Figure 21b). In separate work, Jiang et al.^[267] used APT to create maps displaying the atomically dispersed Ni atoms used for CO_2 reduction, which seem to show Ni atoms predominantly coordinating to C (Figure 21c). What is evident in both Figure 21b,c is the large voids, which were attributed to the low detection efficiency of atoms (Figure 21b).^[266] This reveals one limitation of APT; the nanoscale sample volume analyzed results in 10^7 – 10^8 ion counts, whereas time-of-flight secondary ion mass spectrometry (Section 4.2.4) and inductively coupled plasma mass spectrometry (Section 4.2.6) analyze μm^3 – mm^3 sample volumes, resulting in $>10^9$ ions.^[268] Nevertheless, looking toward the future with the advent of new sample preparation routes, laser pulsing, and detectors, APT presents a possible pathway to measuring the identity and coordination nature of dual-atoms catalytic sites as well as all surrounding atoms, thus becoming a complementary characterization to STEM (Section 4.1.1) and X-ray absorption spectroscopy (Section 4.2.1).^[268]

4.2. Spectroscopy and Spectrometry

4.2.1. X-Ray Absorption Spectroscopy

XAS carried out at synchrotron facilities can supply information on electronic structure (catalyst atoms oxidation states, d-band

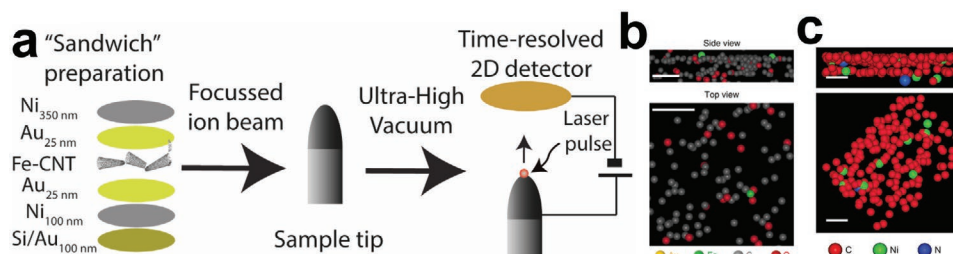


Figure 21. Atom probe tomography. a) Schematic preparation process of Fe-CNT catalyst for measurement. Based on reference [269]. b) Side view (upper) and top view (lower) of CNT planes containing Fe SAC. Spheres represent Au (yellow), Fe (green), C (gray), and O (red) atoms. Scale bars, 2 nm. Reproduced under the Creative Commons CC BY license.^[269] Copyright 2019, Nature Publishing Group. c) Side view (upper) and top view (lower) of Ni SAC within graphene layers. Spheres represent Ni (green), N (blue), and C (red) atoms. Scale bars, 1 nm. Reproduced with permission.^[270] Copyright 2017, Elsevier.

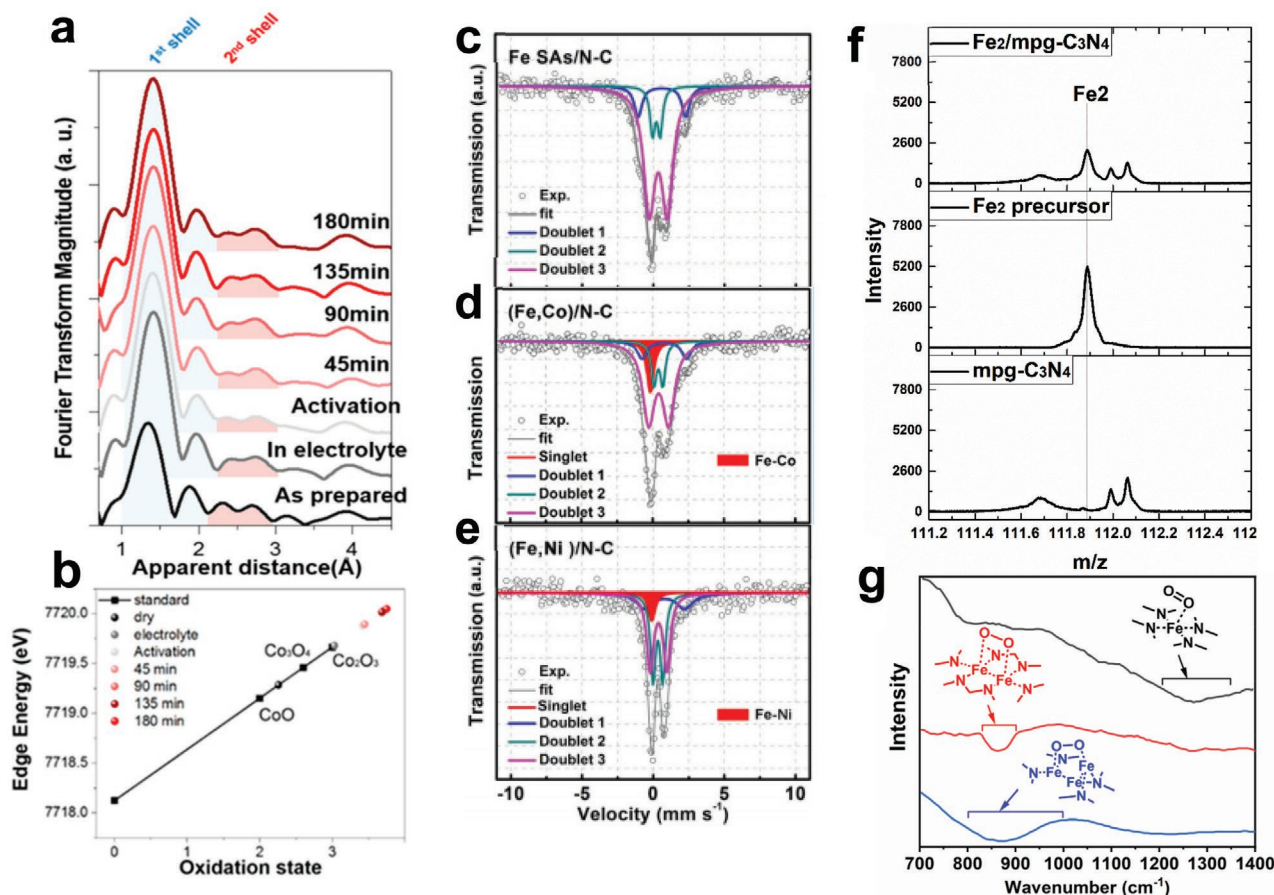


Figure 22. a) Fourier transformed Co K-edge EXAFS (without phase correction) for Co/N/C as prepared and under operando conditions with constant current density (10 mA cm^{-2}) for up to 180 min. b) K-edge energies (at 50% level) of XANES spectra with Co reference compounds included. a,b) Reproduced with permission.^[58] Copyright 2019, American Chemical Society. c–e) ^{57}Fe Mössbauer transmission spectra recorded at 298 K for Fe/N/C SAC and Fe-Ni/N/C and Fe-Co/N/C DACs, with both fittings and experimental components. Red highlighted singlet in d,e) represents the Fe–Ni and Fe–Co. Reproduced with permission.^[49] Copyright 2017, American Chemical Society. f) ToF-SIMS of $\text{Fe}_2/\text{mpg-C}_3\text{N}_4$, Fe_2 precursor and $\text{mpg-C}_3\text{N}_4$ with signal around m/z 111.9 signal assigned to Fe_2^+ . Reproduced under the Creative Commons CC BY license.^[237] Copyright 2018, Nature Publishing Group. g) Low temperature (140 K) FTIR showing superoxo-like O_2 adsorption on $\text{Fe}_1/\text{N/C}$ SAC and peroxy-like O_2 adsorption on $\text{Fe}_2/\text{N/C}$ DAC and $\text{Fe}_3/\text{N/C}$ TAC. Based on reference [68].

occupancy, and local symmetry) through X-ray absorption near-edge spectroscopy (XANES), while coordination number and atomic bond distances can be found from extended X-ray absorption fine structure (EXAFS) analysis. The benefit of DACs is the bonding distance from EXAFS data is presented in both directions for the metal atoms. For instance, the bond length from first metal atom to the second metal atoms and vice versa should be identical, therefore providing stronger support of the proposed structure.^[91] EXAFS measurements have even been used to quantitatively analyze the ratio of Co particles, CoN_4 SACs, and Co_2N_5 DACs within samples, although it is unclear how this was achieved.^[125] Information deduced from XANES and EXAFS data can be complemented by theoretical calculations as well as by direct imaging of DACs through techniques such as STEM (Section 4.1.1). XAS can also be carried out in situ or in operando, being able to provide insights that can be used to propose coordination geometry of catalytic sites while in the testing environment or during operation.

Hu and co-workers have used XAS to analyze changes in electrocatalytic site structure of their prepared Co/N/C SAC

under activated O_2 evolution conditions (Figure 16c).^[58] From operando Co K-edge EXAFS, the second coordination shell of Co is represented by signals from 2 to 3 Å, with a new scattering path (Co–Fe) distinguished at 2.51 Å (Figure 22a), which was suggested to arise from a new Co–Fe interaction. Meanwhile, the coordination number of ≈ 0.25 suggested only one-fourth of Co ions interacted with Fe ions in their Co-Fe/N/C catalyst. Hu's group used operando XAS to demonstrate their robust catalyst with no significant structural change in all interaction paths after 180 min (Figure 22a), although a minor change in the Co–Fe path was noted by the authors. The incorporation of Fe was confirmed by inductively coupled plasma atomic emission spectroscopy (ICP-AES) (Section 4.2.6). Operando XAS also revealed that the Co oxidation state increased during OER (Figure 22b), which was ascribed to a Co(IV)=O intermediate during OER. Operando XAS has also been used on a Ni_2 DAC for CO_2 reduction.^[194] These works demonstrate the importance of in situ and operando techniques in determining how catalytic sites mechanisms truly function and changes that may take place at the site during catalysis.^[254] For operando hard

XAS, the X-ray beam can induce structural changes in the electrochemical system; consequently, care is required to resolve the difference between changes occurring from applied potential/adsorbates and the high-energy X-ray beam.^[255] While indicators of heterometallic DACs can be observed from EXAFS, it can be difficult to discriminate from metal-metal signals from larger metallic clusters.^[269] It should also be noted that XAS provides sample-averaged information, therefore requiring precise synthesis of DAC in order to interpret the data obtained. Another issue involving XAS arises from the fact it is a bulk method that identifies both electrochemically accessible and inaccessible sites, meaning identified sites may not be contributing to electrochemical activity; however, the use of operando XAS under potential control can help to distinguish these sites as the former show response in the XANES spectra, and linear combination fitting can be used to estimate the ratio of electrochemically active sites in the sample. Finally, structures determined from XAS data are defined by a best-fit model, with the presented best-fit model not always having physical grounding. Guan et al.^[91] suggested one method to improve current data presentation would be for different models to be presented, along with the model errors and statistical analysis, allowing the reader to compare models and make a more informed decision. Greater use of post-mortem studies (following electrochemical testing) is advised where possible to confirm the robustness of the DACs, as completed by Wang et al. and Zhang et al.^[49,75]

4.2.2. Electron Paramagnetic Resonance and Nuclear Magnetic Resonance

Electron paramagnetic resonance (EPR) is a highly sensitive spectroscopic method for studying paramagnetic species, providing information on the electronic structure of materials.^[270] Because EPR is sensitive to unpaired electrons only, most atoms are “transparent” to EPR; however, many transition metals ions are EPR active. Depending on the type of EPR, conditions, and sample properties, the paramagnetic species separation distances, local coordination structure, charge assignment, and spin quantity^[274] can be determined. Hyperfine interactions between the unpaired electron and local nuclei can give rise to the splitting of EPR resonance signals, indicating the type of local nucleus. For instance, electron spin echo envelope modulation EPR was applied successfully to complex clusters such as nitrogenase, where it helped resolve the long-debated central interstitial atom as C.^[272] Meanwhile, Le Mest et al.^[273] and Liu et al.^[35] analyzed cofacial separated Pacman-like Co–Co dimer structures with EPR. For the former study, EPR was crucial in determining that neutral Co porphyrin dimers were not able to bind O₂, whereas the protonated version could. In the latter, EPR determined Co–Co distances of the O₂ reduction catalyst. Furthermore, Matsushita et al. made expanded phthalocyanine rings allowing them to host two adjacent in-plane Mo ions;^[191] EPR was used in conjunction with IR to distinguish between Mo^V=O and Mo^V≡N structures, that could not be told apart by ¹H NMR and HR-MS. The former is EPR-silent and is indeed the complex they obtained. Meanwhile, from EPR, model SACs consisting of ferric porphyrins with hangman groups showed an elongated Fe–Cl bond length compared to the

non-hangman equivalent,^[274] suggesting future insights could be obtained from hangman groups that form DACs.

In terms of heterogenous electrocatalysts with conductive carbon supports, cryogenic conditions ($T \leq 10$ K, which are not commonly available) are required to enable resolved paramagnetic species signals.^[270] EPR also suffers from high knowledge barriers to fully understand the technique and requires simulation to employ it to its full capability. For a tutorial review for non-specialists, we recommend work by Roessler and Salvadori.^[270] For SACs, most have not delved into this insightful technique, although examples are appearing of how X-band EPR can be used to good effect while characterizing Fe/N/C SACs.^[271,275–278] To the best of our knowledge, EPR has so far not been applied directly to characterize heterogeneous DACs; however, with continued improvements in sensitivity,^[279] and development of in situ methods,^[280] EPR could present a powerful method of DAC characterization.

Aside from EPR, ¹³C and ¹H nuclear magnetic resonance (NMR) spectroscopy is an insightful tool for organic ligand analysis in metal complexes on supports;^[284] however, so far it has not been used for electrochemical DACs. As the technique and understanding progress it is expected NMR could provide a further characterization on DACs.

4.2.3. Mössbauer Spectroscopy

Mössbauer spectroscopy is principally suited to differentiating sites of similar structure which are in different oxidation and/or spin states for isotopes of selected elements (Fe, Au, Ru, Ir, etc.) by providing fingerprints on their local electronic structure and coordination.^[282,283] Mössbauer spectroscopy has so far been utilized in limited cases for determining the presence of DACs. One such example was presented by Wang et al. who used ex-situ room temperature ⁵⁷Fe Mössbauer spectroscopy to understand the coordination environment of their in-plane adjacent Fe–Co/N/C DAC.^[49] Compared to the Fe/N/C SAC Mössbauer spectrum (Figure 22c), the Fe–Co/N/C DAC was assigned an additional minor singlet component (Figure 22d), suggested to indicate the presence of a Fe–Co bond. A Fe–Ni/N/C catalyst was also produced by Wang et al. in the same work by changing Co nodes to Ni nodes in the MOF. The Mössbauer spectrum of Fe–Ni/N/C (Figure 22e) was assigned a similar singlet component to the Fe–Ni bond. One important consideration is ex situ room temperature Mössbauer struggles to detect inorganic cluster species, which may be unknowingly present within the catalyst.^[271] Hence, where possible, low temperature, in situ and postmortem Mössbauer should be conducted to fully understand the catalytic sites.^[276] In other work, Kneebone et al. used ⁵⁷Fe Mössbauer spectroscopy in combination with nuclear inelastic scattering, a probe molecule (NO_(g)) and DFT calculations on an O₂ reduction active PANI-based Fe–N–C catalyst.^[284] Their results suggested edge-hosted FeN₄ or Fe₂N₅ sites (previously studied by Holby et al.^[285,286] using DFT) were responsible for NO and oxygen binding in the catalyst. Further conclusions on the catalyst could not be drawn due to its inhomogeneity. A benefit of ⁵⁷Fe Mössbauer spectroscopy is that it can also be used to determine the active site utilization of Fe catalysts, providing a quantitative analysis of the limits of further activity

enhancement.^[121] On the other hand, an issue with Mössbauer, aside from the limited number of elements it can be applied to, and the requirement of isotopes, is the fact it is a bulk method similar to XAS, not being able to distinguish between electrochemically accessible and inaccessible sites. Despite this, Mössbauer is seen as a complementary characterization technique in helping to determine DACs of relevant elements and it is predicted to be utilized further in papers attempting to determine the chemical state of their catalytic sites.

4.2.4. Time-of-Flight Secondary Ion Mass Spectrometry

Time-of-flight secondary ion mass spectrometry (ToF-SIMS) can provide characterization via a high-energy ion beam which causes surface material sputtering, which is then analyzed by mass spectrometry. ToF-SIMS was first identified in the 1990s as a technique for probing SACs by Bertrand and co-workers,^[287] who later found evidence of FeN₄/C and Fe₂/N/C sites in pyrolyzed catalysts based on positive ion fragment results.^[288,289] For DACs, Tian et al. found via ToF-SIMS their Fe₂/mpg-C₃N₄ alkene epoxidation catalyst contained Fe₂ sites by comparing the intensity of the Fe₂ precursor, mpg-C₃N₄ and Fe₂ doped mpg-C₃N₄ catalyst (Figure 22f).^[235] Although, only a limited m/z range of SIMS results are presented by Tian et al., which does not rule out the possibility of other Fe-containing fragments in the catalyst. Additionally, no measurement details for the ToF-SIMS results are given by the authors. Meanwhile, Jaramillo and co-workers used ToF-SIMS to help confirm Ni_xC_y sites in their CO₂ reduction active Ni/N/C SAC.^[258] Additionally, dual sites were ruled out due to a lack of fragment intensity in the region expected for Ni₂N_xC_y m/z values.^[258] Without their HAADF-STEM results, it would have been difficult to substantiate this, since DAC or other clusters could be in quantities below the detection limit of ToF-SIMS or present within electrochemically accessible pores which are not reached by the surface-sensitive ToF-SIMS. While ToF-SIMS can resolve individual atoms it can become difficult to interpret results when increasing numbers of elements are present as several entities may have the same m/z. Additionally, organic species also typically exist on catalyst surfaces, causing signals of interest to be masked by those of organics. This can be helped by sputtering clean the catalyst surface. These examples demonstrate the possibilities and limitations of ToF-SIMS for DAC characterization; with one final drawback being the low accessibility of this technique.

4.2.5. Fourier-Transform Infrared Spectroscopy

In situ FTIR has emerged as an extremely sensitive technique to analyze reaction intermediates in electrochemical processes and elucidate their adsorption mode within a substrate.^[290–292] This technique therefore offers the possibility of correlating differences in the vibrational modes of the adsorbates with changes in the potential.^[293] Real-time information regarding the atomic structure of the catalyst can as well be obtained employing in situ FTIR. The wavenumber of the vibration attributed to a given adsorbate changes depending on the adsorption mode,

influenced by the nature of the catalyst (SAC or DAC, bulk material etc.). For example, Stair and co-workers^[297] were able to quickly differentiate between Pt single atoms and Pt nanoparticles using FTIR by showing that CO selectively adsorbed to Pt nanoparticles. Flytzani-Stephanopoulos and co-workers have also characterized thermal heterogeneous catalysts FTIR, this time in situ (with HAADF-STEM) to confirm iridium dimers can bind end-on to WO₃.^[295] Meanwhile, evidence of a dual catalytic site at the perimeter of Au nanoparticles in Au/TiO₂ was provided by Green et al. who proposed a low-temperature mechanism for the CO oxidation on Au/TiO₂, utilizing in situ FTIR to monitor the kinetic changes at both interfacial Au and TiO₂ sites.^[296]

Characterization of atomic electrocatalysts through low-temperature FTIR was shown by Ye et al. who analyzed O₂ adsorption in their O₂ reduction Fe atomic catalysts.^[68] Figure 22g shows how SAC Fe₁/N/C presents a peak at 1200–1350 cm⁻¹ associated with superoxo (end-on) O₂ adsorption. Meanwhile, Fe₂/N/C DAC and Fe₃/N/C TAC-based catalysts show peaks present between 800 and 1000 cm⁻¹, demonstrating peroxo-like (side-on) O₂ adsorption. Finally, operando synchrotron FTIR has been used to detect the *COOH intermediate species (observed at 1532 cm⁻¹) in CO₂ reduction to CO on Ni₂ sites.^[194] These results provide clear motivation to further employ in situ and operando FTIR to establish reaction pathways and key binding modes of adsorbed intermediates in DACs.

4.2.6. Inductively Coupled Plasma Mass Spectrometry

Inductively coupled plasma atomic emission spectroscopy (ICP-AES) or mass spectrometry (ICP-MS) is used for the detection of chemical elements. ICP-AES has been used as a complementary characterization technique to suggest DACs, whereby Pt loadings in a catalyst were analyzed following SAC synthesis (via first step ALD) and then tested again after DAC formation (via second step ALD), with the ratio of Pt loadings approximately doubling.^[19] This provided an early suggestion of potential DAC synthesis, although by no means solely confirmed DAC formation, with XAS and STEM also required. In the same manner, ICP-AES could quickly provide initial confirmation of unsuccessful DAC synthesis from an initial SAC. Aside from methods that initially create a SAC, followed by a DAC, such as the case in ALD presented above, ICP cannot be used as a characterization tool to distinguish the type of catalytic site.

5. Summary

DACs, which can be found in the active sites of metalloenzymes, such as CcO and nitrogenase, are known to possess several advantages over nanoparticles and pure metals including high selectivity, high intrinsic activity, and maximum atom utilization. Additionally, according to DFT, DACs solve the fundamentally limited electrocatalyst activity issues of SACs by circumventing known scaling relations that are present in any electrochemical reaction that involves more than one reaction intermediate. This is achieved through the geometrical and

synergistic effect of the atomically nearby metal centers and the availability of two active sites for reaction intermediate binding. If theoretical predictions of DAC performance could be realized in real fuel cells and electrolyzers and stabilized over the entire calendar lifetime, the impact would be transformative: the resulting devices would operate at unprecedentedly high efficiencies, potentially without even needing PGM catalysts. In terms of characterization, it can be concluded that an ensemble of ex situ and in situ methods, including XAS and STEM, are required to determine the electrochemically active DAC sites. So far, a range of catalytic sites have been presented in heterogeneous catalysts, caused by deposition and high-temperature pyrolysis techniques commonly used for heterogeneous DAC synthesis. These DACs have been analyzed for several electrochemical reactions, along with some promising incipient research completed in relevant devices, although the stability of the highly active sites under harsher conditions is still an open question.

5.1. Challenges

While DACs demonstrate several advantages over SACs and other catalysts, several obstacles remain which hinder their progress and application. For DACs, particular challenges lie in the identification and differentiation of the two metal centers. Deeper insights from advanced atomic resolution characterization such as HAADF-STEM, XANES, EXAFS, ToF-SIMS, APT, and DFT are required to piece together information on the geometric arrangement and electronic structure of the metal centers in DACs such as coordination numbers, atomic distances, and neighboring atoms.

Another hurdle for DACs is their controllable and scalable synthesis with high metal loading without the formation of nanoparticles, clusters, or SACs as well as preventing their potential deactivation during working conditions from processes including agglomeration. Precisely tuning the catalyst support and local environment maximizes the likelihood of DAC formation with enhanced stability, although this remains a challenge. Following synthesis, the number of active DACs is required for accurate determination for TOF. However, so far there is a lack of methods to determine the types of atomic active sites present across the catalyst materials.

It should not be neglected that DACs require sufficient accessibility of reactants to their sites to enable optimum performance, therefore supporting materials should demonstrate a hierarchical pore structure with high surface area (and high conductivity).

5.2. Further Research and Perspectives

While there are numerous examples of DACs used in several electrochemical reactions, this list is comparatively short compared to SACs, indicating that DACs are still a relatively unexplored area of research with many potential avenues for further study. Thus far, metalloenzymes have provided inspiration for several DAC designs and further biomimicry can be taken from nature. For example, hemerythrin, a protein responsible for O₂

transport and found in some marine invertebrates, is an interesting example of an oxo-bridged diiron center; this is similar to the metal center found in soluble methane monooxygenase, which catalyzes the conversion of methane to methanol, breaking the strong C–H bond.^[297–299] Additionally, hemocyanin with its oxo-bridged Cu dual atom center, could provide further electrocatalytic inspiration.^[300] By further understanding the relevant processes taking place in relevant metalloenzymes and other living organisms, a more accurate catalyst design for successful biomimicry will be obtained.

Further understanding of the role of each metal atom and the dynamic nature of atomic configurations in a DAC during reaction conditions can be obtained employing advanced in situ and in operando characterization, such as XAS.^[269] More commonly combining operando XAS measurements with DFT can help construct a representative active site model and consequently identify the most active centers.^[186] We anticipate that high-energy-resolution fluorescence detection XAS will be particularly useful,^[301,302] as will artificial neural networks to process complex in situ XAS data.^[303]

Looking toward the near future, from developed design principles and improving data sets, machine learning techniques are beginning to allow accelerated throughput of potential catalysts.^[119] This is necessary for DACs due to the extensive list of possible combinations for heteronuclear dimers, with the mixing of 3d, 4d, and 5d and main group metals leading to >900 potential contenders for one certain type of support with asymmetric adsorption sites.^[304] Moreover, theoretical models should also elucidate factors controlling DAC stability under relevant conditions so design rules can be developed for more durable catalysts.

Determination of the number of active sites, as achieved for Fe/N/C O₂ reduction catalysts,^[120,122] is required to enable calculation of TOF and comparison of performance.^[39] So far, no method has been produced for quantitative active site determination of DACs, although it is suggested sites mimicking CcO, which is known to be inhibited by cyanide,^[32] may also be poisoned by cyanide and hence quantified.

In terms of synthetic routes, focus should be made on developing new methods to create controlled model DAC systems, possibly via ultra-high vacuum system containing ToF mass selection of metal dimers.^[305] The ultimate goal is to achieve controlled production of DACs in an inexpensive, low energy intensive and facile manner to enable effective scaling of the process. Experimentally synthesized examples of potential suitable catalyst support that could enable beneficial DAC interaction include confining metal catalyst centers on carbon substrates, in particular shapes such as carboncones, nanobowls, graphene layers, carbon nanotubes, or as recently achieved via MOFs.^[114,117,306–309] Ultimately, DACs need to be more thoroughly evaluated in electrochemical devices to ascertain their performance under realistic conditions. Providing that these obstacles can be surmounted, we envision that DACs in electrochemical devices will make a profound impact on our transition to net zero.

Supporting Information

Supporting Information is available from the Wiley Online Library or from the author.

Acknowledgements

A.P. thanks the EPSRC Centre for Doctoral Training in the Advanced Characterisation of Materials (grant number EP/L015277/1). I.E.L.S., and J.B. gratefully acknowledge the Engineering and Physical Sciences Research Council (EP/M0138/1), the European Research Council (ERC) under the European Union's Horizon 2020 research and innovation programme (grant agreement No. 866402) and the National Research Council Canada through the Materials for Clean Fuels Challenge Program. A.L. thanks the EU for the Marie Curie Research Fellowship (892614) through the project HAEMOGLOBIN.

Conflict of Interest

The authors declare no conflict of interest.

Keywords

CO₂ reduction, electrocatalysts, N₂ reduction, O₂ evolution, O₂ reduction

Received: September 1, 2021

Revised: October 25, 2021

Published online: December 5, 2021

- [1] International Energy Agency, *Energy Technology Perspectives 2017*, Paris, **2017**, https://www.oecd-ilibrary.org/energy/energy-technology-perspectives-2017_energy_tech-2017-en (accessed: November 2021).
- [2] P. G. Levi, J. M. Cullen, *Environ. Sci. Technol.* **2018**, *52*, 1725.
- [3] W. Li, J. Liu, D. Zhao, *Nat. Rev. Mater.* **2016**, *1*, 16023.
- [4] A. Grimaud, J. Rossmeisl, P. Strasser, *Research Needs towards Sustainable Production of Fuels and Chemicals*, (Eds: A. Latimer, C. F. Dickens), Belgium, **2019**, <https://www.energy-x.eu/research-needs-report/> (accessed: November 2021).
- [5] K. Ayers, N. Danilovic, R. Ouimet, M. Carmo, B. Pivovar, M. Bornstein, *Annu. Rev. Chem. Biomol. Eng.* **2019**, *10*, 219.
- [6] X. X. Wang, M. T. Swihart, G. Wu, *Nat. Catal.* **2019**, *2*, 578.
- [7] X. Tian, X. F. Lu, B. Y. Xia, X. W. Lou, *Joule* **2020**, *4*, 45.
- [8] N. Lazouski, M. Chung, K. Williams, M. L. Gala, K. Manthiram, *Nat. Catal.* **2020**, *3*, 463.
- [9] Y. Y. Birdja, E. Pérez-Gallent, M. C. Figueiredo, A. J. Göttle, F. Calle-Vallejo, M. T. M. Koper, *Nat. Energy* **2019**, *4*, 732.
- [10] B. Lu, Q. Liu, S. Chen, *ACS Catal.* **2020**, *10*, 7584.
- [11] S. T. Thompson, D. Papageorgopoulos, *Nat. Catal.* **2019**, *2*, 558.
- [12] F. Luo, A. Roy, L. Silvioli, D. A. Cullen, A. Zitolo, M. T. Sougrati, I. C. Oguz, T. Mineva, D. Teschner, S. Wagner, J. Wen, F. Dionigi, U. I. Kramm, J. Rossmeisl, F. Jaouen, P. Strasser, *Nat. Mater.* **2020**, *19*, 1215.
- [13] J. D. Benck, T. R. Hellstern, J. Kibsgaard, P. Chakhranont, T. F. Jaramillo, *ACS Catal.* **2014**, *4*, 3957.
- [14] S. Zhang, L. Nguyen, J. X. Liang, J. Shan, J. J. Liu, A. I. Frenkel, A. Patlolla, W. Huang, J. Li, F. F. Tao, *Nat. Commun.* **2015**, *6*, 7938.
- [15] Z. W. Seh, J. Kibsgaard, C. F. Dickens, I. Chorkendorff, J. K. Nørskov, T. F. Jaramillo, *Science* **2017**, *355*, eaad4998.
- [16] Y. Zhu, J. Sokolowski, X. Song, Y. He, Y. Mei, G. Wu, *Adv. Energy Mater.* **2020**, *10*, 1902844.
- [17] J. Wang, Z. Li, Y. Wu, Y. Li, *Adv. Mater.* **2018**, *30*, 1801649.
- [18] X. Zhang, Z. Li, Y. Qu, T. Yuan, W. Wang, Y. Wu, *Chem* **2019**, *5*, 1486.
- [19] H. Yan, Y. Lin, H. Wu, W. Zhang, Z. Sun, H. Cheng, W. Liu, C. Wang, J. Li, X. Huang, T. Yao, J. Yang, S. Wei, J. Lu, *Nat. Commun.* **2017**, *8*, 1070.
- [20] S. Yang, A. Verdaguier-Casadevall, L. Arnarson, L. Silvioli, V. Čolić, R. Frydendal, J. Rossmeisl, I. Chorkendorff, I. E. L. Stephens, *ACS Catal.* **2018**, *8*, 4064.
- [21] Z. Y. Wu, X. X. Xu, B. C. Hu, H. W. Liang, Y. Lin, L. F. Chen, S. H. Yu, *Angew. Chem., Int. Ed.* **2015**, *54*, 8179.
- [22] J. J. Li, S. Chen, N. Yang, M. Deng, S. Ibraheem, J. Deng, J. J. Li, L. Li, Z. Wei, *Angew. Chem., Int. Ed.* **2019**, *58*, 7035.
- [23] A. R. Singh, J. H. Montoya, B. A. Rohr, C. Tsai, A. Vojvodic, J. K. Nørskov, *ACS Catal.* **2018**, *8*, 4017.
- [24] X. Liu, P. Schlexer, J. Xiao, Y. Ji, L. Wang, R. B. Sandberg, M. Tang, K. S. Brown, H. Peng, S. Ringe, C. Hahn, T. F. Jaramillo, J. K. Nørskov, K. Chan, *Nat. Commun.* **2019**, *10*, 32.
- [25] W. Ju, A. Bagger, X. Wang, Y. Tsai, F. Luo, T. Möller, H. Wang, J. Rossmeisl, A. S. Varela, P. Strasser, *ACS Energy Lett.* **2019**, *4*, 1663.
- [26] R. M. Bullock, J. G. Chen, L. Gagliardi, P. J. Chirik, O. K. Farha, C. H. Hendon, C. W. Jones, J. A. Keith, J. Klosin, S. D. Minton, R. H. Morris, A. T. Radosevich, T. B. Rauchfuss, N. A. Strotman, A. Vojvodic, T. R. Ward, J. Y. Yang, Y. Surendranath, *Science* **2020**, *369*, eabc3183.
- [27] C. H. Kjaergaard, J. Rossmeisl, J. K. Nørskov, *Inorg. Chem.* **2010**, *49*, 3567.
- [28] M. Wikström, K. Krab, V. Sharma, *Chem. Rev.* **2018**, *118*, 2469.
- [29] P. E. M. Siegbahn, M. R. A. Blomberg, *Chem. Rev.* **2010**, *110*, 7040.
- [30] L. C. Seefeldt, Z.-Y. Yang, S. Duval, D. R. Dean, *Biochim. Biophys. Acta, Bioenerg.* **2013**, *1827*, 1102.
- [31] H. L. Rutledge, F. A. Tezcan, *Chem. Rev.* **2020**, *120*, 5158.
- [32] X. Wang, R. Clément, M. Roger, M. Bauzan, I. Mazurenko, A. De Poulpique, M. Ilbert, E. Lojou, *J. Am. Chem. Soc.* **2019**, *141*, 11093.
- [33] H. Chen, O. Simoska, K. Lim, M. Grattieri, M. Yuan, F. Dong, Y. S. Lee, K. Beaver, S. Weliwatte, E. M. Gaffney, S. D. Minton, *Chem. Rev.* **2020**, *120*, 12903.
- [34] J. A. Cracknell, K. A. Vincent, F. A. Armstrong, *Chem. Rev.* **2008**, *108*, 2439.
- [35] Y. Liu, G. Zhou, Z. Zhang, H. Lei, Z. Yao, J. Li, J. Lin, R. Cao, *Chem. Sci.* **2020**, *11*, 87.
- [36] M. R. Crawley, D. Zhang, A. N. Oldacre, C. M. Beavers, A. E. Friedman, T. R. Cook, *J. Am. Chem. Soc.* **2021**, *143*, 1098.
- [37] J. P. Collman, P. Denisevich, Y. Konai, M. Marrocco, C. Koval, F. C. Anson, *J. Am. Chem. Soc.* **1980**, *102*, 6027.
- [38] J. Wang, W. Liu, G. Luo, Z. Li, C. C. Zhao, H. Zhang, M. Zhu, Q. Xu, X. Wang, C. C. Zhao, Y. Qu, Z. Yang, T. Yao, Y. Y. Li, Y. Lin, Y. Wu, Y. Y. Li, *Energy Environ. Sci.* **2018**, *11*, 3375.
- [39] M. Primbs, Y. Sun, A. Roy, D. Malko, A. Mehmood, M.-T. Sougrati, P.-Y. Blanchard, G. Granozzi, T. Kosmala, G. Daniel, P. Atanassov, J. Sharman, C. Durante, A. Kucernak, D. Jones, F. Jaouen, P. Strasser, *Energy Environ. Sci.* **2020**, *13*, 2480.
- [40] K. D. Jensen, J. Tymoczko, J. Rossmeisl, A. S. Bandarenka, I. Chorkendorff, M. Escudero-Escribano, I. E. L. Stephens, *Angew. Chem., Int. Ed.* **2018**, *57*, 2800.
- [41] J. Staszak-Jirkovský, R. Subbaraman, D. Strmcnik, K. L. Harrison, C. E. Diesendruck, R. Assary, O. Frank, L. Kobr, G. K. H. Wiberg, B. Genorio, J. G. Connell, P. P. Lopes, V. R. Stamenkovic, L. Curtiss, J. S. Moore, K. R. Zavadil, N. M. Markovic, *ACS Catal.* **2015**, *5*, 6600.
- [42] C. Yoo, Y. Lee, *Chem. Sci.* **2016**, *8*, 600.
- [43] O. Westhead, R. Jervis, I. E. L. Stephens, A comparison of the figures-of-merit for nitrogen reduction on nitrogenase, solid electrodes and homogeneous catalysts, <https://data.hpc.imperial.ac.uk/resolve/?doi=8243> (accessed: November 2021).
- [44] O. Westhead, R. Jervis, I. E. L. Stephens, *Science* **2021**, *372*, 1149.
- [45] D. V. Yandulov, R. R. Schrock, *Science* **2003**, *301*, 76.
- [46] B. H. R. Suryanto, K. Matuszek, J. Choi, R. Y. Hodgetts, H.-L. Du, J. M. Bakker, C. S. M. Kang, P. V. Cherepanov, A. N. Simonov, D. R. MacFarlane, *Science* **2021**, *372*, 1187.

- [47] S. Z. Andersen, M. J. Statt, V. J. Bukas, S. G. Shapel, J. B. Pedersen, K. Krempel, M. Saccoccio, D. Chakraborty, J. Kibsgaard, P. C. K. Vesborg, J. Nørskov, I. Chorkendorff, *Energy Environ. Sci.* **2020**, *13*, 4291.
- [48] J. M. Rivera Ortiz, R. H. Burris, *J. Bacteriol.* **1975**, *123*, 537.
- [49] J. Wang, Z. Huang, W. Liu, C. Chang, H. Tang, Z. Li, W. Chen, C. Jia, T. Yao, S. Wei, Y. Wu, Y. Li, *J. Am. Chem. Soc.* **2017**, *139*, 17281.
- [50] Z. Lu, B. Wang, Y. Hu, W. Liu, Y. Zhao, R. Yang, Z. Li, J. Luo, B. Chi, Z. Jiang, M. Li, S. Mu, S. Liao, J. Zhang, X. Sun, *Angew. Chem., Int. Ed.* **2019**, *58*, 2622.
- [51] Y. Zhou, W. Yang, W. Utetiawabo, Y. M. Lian, X. Yin, L. Zhou, P. Yu, R. Chen, S. Sun, *J. Phys. Chem. Lett.* **2020**, *11*, 1404.
- [52] W. Ren, X. Tan, W. Yang, C. Jia, S. Xu, K. Wang, S. C. Smith, C. Zhao, *Angew. Chem., Int. Ed.* **2019**, *58*, 6972.
- [53] L. Gong, H. Zhang, Y. Wang, E. Luo, K. Li, L. Gao, Y. Wang, Z. Wu, Z. Jin, J. Ge, Z. Jiang, C. Liu, W. Xing, *Angew. Chem., Int. Ed.* **2020**, *59*, 13923.
- [54] N. Mihara, Y. Yamada, H. Takaya, Y. Kitagawa, S. Aoyama, K. Igawa, K. Tomooka, K. Tanaka, *Chem. - Eur. J.* **2017**, *23*, 7508.
- [55] L. Jiao, J. Li, L. L. Richard, Q. Sun, T. Stracensky, E. Liu, M. T. Sougrati, Z. Zhao, F. Yang, S. Zhong, H. Xu, S. Mukerjee, Y. Huang, D. A. Cullen, J. H. Park, M. Ferrandon, D. J. Myers, F. Jaouen, Q. Jia, *Nat. Mater.* **2021**, *20*, 1385.
- [56] M. Busch, N. B. Halck, U. I. Kramm, S. Siahrostami, P. Krtil, J. Rossmeisl, *Nano Energy* **2016**, *29*, 126.
- [57] H. Wan, Y. Jiao, A. Bagger, J. Rossmeisl, *ACS Catal.* **2021**, *11*, 533.
- [58] L. Bai, C.-S. Hsu, D. T. L. Alexander, H. M. Chen, X. Hu, *J. Am. Chem. Soc.* **2019**, *141*, 14190.
- [59] Y. Yang, Y. Qian, H. Li, Z. Zhang, Y. Mu, D. Do, B. Zhou, J. Dong, W. Yan, Y. Qin, L. Fang, R. Feng, J. Zhou, P. Zhang, J. Dong, G. Yu, Y. Liu, X. Zhang, X. Fan, *Sci. Adv.* **2020**, *6*, eaba6586.
- [60] Z. W. Chen, L. X. Chen, C. C. Yang, Q. Jiang, *J. Mater. Chem. A* **2019**, *7*, 3492.
- [61] X. Zhu, D. Zhang, C. J. Chen, Q. Zhang, R. S. Liu, Z. Xia, L. Dai, R. Amal, X. Lu, *Nano Energy* **2020**, *71*, 104597.
- [62] L. Zhang, J. M. T. A. Fischer, Y. Jia, X. Yan, W. Xu, X. Wang, J. Chen, D. Yang, H. Liu, L. Zhuang, M. Hankel, D. J. Searles, K. Huang, S. Feng, C. L. Brown, X. Yao, *J. Am. Chem. Soc.* **2018**, *140*, 10757.
- [63] A. Han, B. Wang, A. Kumar, Y. Qin, J. Jin, X. Wang, C. Yang, B. Dong, Y. Jia, J. Liu, X. Sun, *Small Methods* **2019**, *3*, 1800471.
- [64] J. Barrio, M. Shalom, *ChemCatChem* **2018**, *10*, 5573.
- [65] C. Wu, X. Zhang, Z. Xia, M. Shu, H. Li, X. Xu, R. Si, A. I. Rykov, J. Wang, S. Yu, S. Wang, G. Sun, *J. Mater. Chem. A* **2019**, *7*, 14001.
- [66] D. Liu, S. Ding, C. Wu, W. Gan, C. Wang, D. Cao, Z. U. Rehman, Y. Sang, S. Chen, X. Zheng, Y. Wang, B. Ge, L. Song, *J. Mater. Chem. A* **2018**, *6*, 6840.
- [67] L. Lin, H. Li, C. Yan, H. Li, R. Si, M. Li, J. Xiao, G. Wang, X. Bao, *Adv. Mater.* **2019**, *31*, 1903470.
- [68] W. Ye, S. S. Chen, Y. Lin, L. Yang, S. S. Chen, X. Zheng, Z. Qi, C. Wang, R. Long, M. Chen, J. Zhu, P. Gao, L. Song, J. Jiang, Y. Xiong, *Chem* **2019**, *5*, 2865.
- [69] Y. Zhu, H. A. Tahini, J. Zhou, Y. Chen, Q. Lin, Z. Hu, R. Fan, S. She, H.-J. Lin, C.-T. Chen, S. C. Smith, Z. Shao, H. Wang, *Chem. Mater.* **2021**, *33*, 5233.
- [70] Y. Zhu, Q. Lin, Y. Zhong, H. A. Tahini, Z. Shao, H. Wang, *Energy Environ. Sci.* **2020**, *13*, 3361.
- [71] J. Dai, Y. Zhu, H. A. Tahini, Q. Lin, Y. Chen, D. Guan, C. Zhou, Z. Hu, H.-J. Lin, T.-S. Chan, C.-T. Chen, S. C. Smith, H. Wang, W. Zhou, Z. Shao, *Nat. Commun.* **2020**, *11*, 5657.
- [72] R. Jasinski, *Nature* **1964**, *201*, 1212.
- [73] S. Mitchell, J. Pérez-Ramírez, *Nat. Commun.* **2020**, *11*, 4302.
- [74] J. P. Collman, M. Marrocco, P. Denisevich, C. Koval, F. C. Anson, *J. Electroanal. Chem.* **1979**, *101*, 117.
- [75] L. Zhang, R. Si, H. Liu, N. Chen, Q. Wang, K. Adair, Z. Wang, J. Chen, Z. Song, J. Li, M. N. Banis, R. Li, T. K. Sham, M. Gu, L. M. Liu, G. A. Botton, X. Sun, *Nat. Commun.* **2019**, *10*, 5453.
- [76] H. Wan, A. W. Jensen, M. Escudero-Escribano, J. Rossmeisl, *ACS Catal.* **2020**, *10*, 5979.
- [77] D. Zhao, Z. Zhuang, X. Cao, C. Zhang, Q. Peng, C. Chen, Y. Li, *Chem. Soc. Rev.* **2020**, *49*, 2215.
- [78] H. Li, H. Zhu, Z. Zhuang, S. Lu, F. Duan, M. Du, *Sustainable Energy Fuels* **2020**, *4*, 996.
- [79] T. Sharifi, E. Gracia-Espino, A. Chen, G. Hu, T. Wågberg, *Adv. Energy Mater.* **2020**, *10*, 1902084.
- [80] B. Mohanty, B. K. Jena, S. Basu, *ACS Omega* **2020**, *5*, 1287.
- [81] Y. Chen, S. Ji, C. Chen, Q. Peng, D. Wang, Y. Li, *Joule* **2018**, *2*, 1242.
- [82] H. Fei, J. Dong, D. Chen, T. Hu, X. Duan, I. Shakir, Y. Huang, X. Duan, *Chem. Soc. Rev.* **2019**, *48*, 5207.
- [83] Q. Shi, S. Hwang, H. Yang, F. Ismail, D. Su, D. Higgins, G. Wu, *Mater. Today* **2020**, *37*, 93.
- [84] T. Sun, L. Xu, D. Wang, Y. Li, *Nano Res.* **2019**, *12*, 2067.
- [85] W. Zang, Z. Kou, S. J. Pennycook, J. Wang, *Adv. Energy Mater.* **2020**, *10*, 1903181.
- [86] F. Zhang, Y. Zhu, Q. Lin, L. Zhang, X. Zhang, H. Wang, *Energy Environ. Sci.* **2021**, *14*, 2954.
- [87] Y. He, S. Liu, C. Priest, Q. Shi, G. Wu, *Chem. Soc. Rev.* **2020**, *49*, 3484.
- [88] Y. Pan, C. Zhang, Z. Liu, C. Chen, Y. Li, *Matter* **2020**, *2*, 78.
- [89] J. Zhang, Q. Huang, J. Wang, J. Wang, J. Zhang, Y. Zhao, *Chin. J. Catal.* **2020**, *41*, 783.
- [90] Y. Ying, X. Luo, J. Qiao, H. Huang, *Adv. Funct. Mater.* **2021**, *31*, 2007423.
- [91] E. Guan, J. Ciston, S. R. Bare, R. C. Runnebaum, A. Katz, A. Kulkarni, C. X. Kronawitter, B. C. Gates, *ACS Catal.* **2020**, *10*, 9065.
- [92] P. Sabatier, *Ber. Dtsch. Chem. Ges.* **1911**, *44*, 1984.
- [93] J. K. Nørskov, J. Rossmeisl, A. Logadottir, L. Lindqvist, J. R. Kitchin, T. Bligaard, H. Jónsson, *J. Phys. Chem. B* **2004**, *108*, 17886.
- [94] J. H. Zagal, M. T. M. Koper, *Angew. Chem., Int. Ed.* **2016**, *55*, 14510.
- [95] A. S. Bandarenka, H. A. Hansen, J. Rossmeisl, I. E. L. Stephens, *Phys. Chem. Chem. Phys.* **2014**, *16*, 13625.
- [96] I. E. L. Stephens, A. S. Bondarenko, F. J. Perez-Alonso, F. Calle-Vallejo, L. Bech, T. P. Johansson, A. K. Jepsen, R. Frydendal, B. P. Knudsen, J. Rossmeisl, I. Chorkendorff, *J. Am. Chem. Soc.* **2011**, *133*, 5485.
- [97] J. K. Nørskov, T. Bligaard, A. Logadottir, J. R. Kitchin, J. G. Chen, S. Pandelov, U. Stimming, *J. Electrochem. Soc.* **2005**, *152*, j23.
- [98] J. Rossmeisl, A. Logadottir, J. K. Nørskov, *Chem. Phys.* **2005**, *319*, 178.
- [99] A. A. Peterson, J. K. Nørskov, *J. Phys. Chem. Lett.* **2012**, *3*, 251.
- [100] E. Skúlason, T. Bligaard, S. Gudmundsdóttir, F. Studt, J. Rossmeisl, F. Abild-Pedersen, T. Vegge, H. Jónsson, J. K. Nørskov, *Phys. Chem. Chem. Phys.* **2012**, *14*, 1235.
- [101] J. Pérez-Ramírez, N. López, *Nat. Catal.* **2019**, *2*, 971.
- [102] C. Song, J. Zhang, in *PEM Fuel Cell Electrocatalysts and Catalyst Layers: Fundamental and Applications*, (Ed: J. Zhang), Springer, London **2008**, pp. 89–134.
- [103] A. Kulkarni, S. Siahrostami, A. Patel, J. K. Nørskov, *Chem. Rev.* **2018**, *118*, 2302.
- [104] Z. F. Huang, J. Song, S. Dou, X. Li, J. Wang, X. Wang, *Matter* **2019**, *1*, 1494.
- [105] J. Gopeesingh, M. A. Ardagh, M. Shetty, S. T. Burke, P. J. Dauenhauer, O. A. Abdelrahman, *ACS Catal.* **2020**, *10*, 9932.
- [106] H. A. Hansen, J. Rossmeisl, J. K. Nørskov, *Phys. Chem. Chem. Phys.* **2008**, *10*, 3722.
- [107] K. L. Svane, H. A. Hansen, T. Vegge, *J. Catal.* **2021**, *393*, 230.
- [108] J. P. Collman, N. K. Devaraj, R. A. Decréau, Y. Yang, Y. L. Yan, W. Ebina, T. A. Eberspacher, C. E. D. Chidsey, *Science* **2007**, *315*, 1565.

- [109] P. Peljo, L. Murtomäki, T. Kallio, H.-J. Xu, M. Meyer, C. P. Gros, J. Barbe, H. H. Girault, K. Laasonen, K. Kontturi, *J. Am. Chem. Soc.* **2012**, *134*, 5974.
- [110] R. R. Durand, C. S. Bencosme, J. P. Collman, F. C. Anson, *J. Am. Chem. Soc.* **1983**, *105*, 2710.
- [111] P. Peljo, L. Murtomäki, T. Kallio, H.-J. Xu, M. Meyer, C. Gros, J. Barbe, H. H. Girault, K. Laasonen, K. Kontturi, *J. Am. Chem. Soc.* **2012**, *134*, 5974.
- [112] H. Wan, T. M. Østergaard, L. Arnarson, J. Rossmeisl, *ACS Sustainable Chem. Eng.* **2019**, *7*, 611.
- [113] V. Viswanathan, H. A. Hansen, J. Rossmeisl, T. F. Jaramillo, H. Pitsch, J. K. Nørskov, *J. Phys. Chem. C* **2012**, *116*, 4698.
- [114] X. Li, S. Duan, E. Sharman, Y. Zhao, L. Yang, Z. Zhuo, P. Cui, J. Jiang, Y. Luo, *J. Mater. Chem. A* **2020**, *8*, 10193.
- [115] T. Sours, A. Patel, J. Nørskov, S. Siahrostami, A. Kulkarni, *J. Phys. Chem. Lett.* **2020**, *11*, 10029.
- [116] M. Lions, J. B. Tommasino, R. Chattot, B. Abeykoon, N. Guillou, T. Devic, A. Demessence, L. Cardenas, F. Maillard, A. Fateeva, *Chem. Commun.* **2017**, *53*, 6496.
- [117] M. O. Cichocka, Z. Liang, D. Feng, S. Back, S. Siahrostami, X. Wang, L. Samperisi, Y. Sun, H. Xu, N. Hedin, H. Zheng, X. Zou, H. C. Zhou, Z. Huang, *J. Am. Chem. Soc.* **2020**, *142*, 15386.
- [118] L. Cao, Y. Shao, H. Pan, Z. Lu, *J. Phys. Chem. C* **2020**, *124*, 11301.
- [119] X. Zhu, J. Yan, M. Gu, T. Liu, Y. Dai, Y. Gu, Y. Li, *J. Phys. Chem. Lett.* **2019**, *10*, 7760.
- [120] F. Luo, C. H. Choi, M. J. M. Primbs, W. Ju, S. Li, N. D. Leonard, A. Thomas, F. Jaouen, P. Strasser, *ACS Catal.* **2019**, *9*, 4841.
- [121] N. R. Sahraie, U. I. Kramm, J. Steinberg, Y. Zhang, A. Thomas, T. Reier, J. P. Paraknowitsch, P. Strasser, *Nat. Commun.* **2015**, *6*, 8618.
- [122] D. Malko, A. Kucernak, T. Lopes, *Nat. Commun.* **2016**, *7*, 13285.
- [123] G. Bae, H. Kim, H. Choi, P. Jeong, D. H. Kim, H. C. Kwon, K.-S. Lee, M. Choi, H.-S. Oh, F. Jaouen, C. H. Choi, *JACS Au* **2021**, *1*, 586.
- [124] C. Zhang, J. Sha, H. Fei, M. Liu, S. Yazdi, J. Zhang, Q. Zhong, X. Zou, N. Zhao, H. Yu, Z. Jiang, E. Ringe, B. I. Yakobson, J. Dong, D. Chen, J. M. Tour, *ACS Nano* **2017**, *11*, 6930.
- [125] M. Xiao, H. Zhang, Y. Chen, J. Zhu, L. Gao, Z. Jin, J. Ge, Z. Jiang, S. Chen, C. Liu, W. Xing, *Nano Energy* **2018**, *46*, 396.
- [126] M. Xiao, Y. Chen, J. Zhu, H. Zhang, X. Zhao, L. Gao, X. Wang, J. Zhao, J. Ge, Z. Jiang, S. Chen, C. Liu, W. Xing, *J. Am. Chem. Soc.* **2019**, *141*, 17763.
- [127] Z. Odabaş, A. Altindal, A. R. Özkaya, B. Salih, Ö. Bekaroğlu, *Sens. Actuators, B* **2010**, *145*, 355.
- [128] M. Özer, A. Altindal, A. R. Özkaya, Ö. Bekaroğlu, *Dalton Trans.* **2009**, 3175.
- [129] L. M. Özer, M. Özer, A. Altindal, A. R. Özkaya, B. Salih, Ö. Bekaroğlu, *Dalton Trans.* **2013**, *42*, 6633.
- [130] A. S. Başak, A. R. Özkaya, A. Altindal, B. Salih, A. Şengül, Ö. Bekaroğlu, *Dalton Trans.* **2014**, *43*, 5858.
- [131] T. Ceyhan, A. Altindal, A. R. Özkaya, B. Salih, Ö. Bekarolu, *Dalton Trans.* **2010**, *39*, 9801.
- [132] I. Koç, M. Özer, A. R. Özkaya, Bekaroğlu, *Dalton Trans.* **2009**, *119*, 6368.
- [133] E. Doğan, M. Özer, A. Altindal, A. R. Özkaya, B. Salih, Ö. Bekaroğlu, *J. Porphyrins Phthalocyanines* **2016**, *20*, 1319.
- [134] J. Y. Cheon, T. Kim, Y. Choi, H. Y. Jeong, M. G. Kim, Y. J. Sa, J. Kim, Z. Lee, T.-H. Yang, K. Kwon, O. Terasaki, G.-G. Park, R. R. Adzic, S. H. Joo, *Sci. Rep.* **2013**, *3*, 2715.
- [135] L. Pan, S. Ott, F. Dionigi, P. Strasser, *Curr. Opin. Electrochem.* **2019**, *18*, 61.
- [136] I. E. L. Stephens, J. Rossmeisl, I. Chorkendorff, *Science* **2016**, *354*, 1378.
- [137] S. Martens, L. Asen, G. Ercolano, F. Dionigi, C. Zalitis, A. Hawkins, A. Martinez, L. Seidl, A. C. Knoll, J. Sharman, P. Strasser, D. Jones, O. Schneider, *J. Power Sources* **2018**, *392*, 274.
- [138] C. M. Zalitis, D. Kramer, A. R. Kucernak, *Phys. Chem. Chem. Phys.* **2013**, *15*, 4329.
- [139] M. Inaba, A. W. Jensen, G. W. Sievers, M. Escudero-Escribano, A. Zana, M. Arenz, *Energy Environ. Sci.* **2018**, *11*, 988.
- [140] K. Ehelebe, T. Ashraf, S. Hager, D. Seeberger, S. Thiele, S. Cherevko, *Electrochem. Commun.* **2020**, *116*, 106761.
- [141] P. Mardle, G. Thirunavukkarasu, S. Guan, Y.-L. Chiu, S. Du, *ACS Appl. Mater. Interfaces* **2020**, *12*, 42832.
- [142] L. Osmieri, J. Park, D. A. Cullen, P. Zelenay, D. J. Myers, K. C. Neyerlin, *Curr. Opin. Electrochem.* **2021**, *25*, 100627.
- [143] X. Zeng, J. Shui, X. Liu, Q. Liu, Y. Li, J. Shang, L. Zheng, R. Yu, *Adv. Energy Mater.* **2018**, *8*, 1701345.
- [144] US DOE, *Fuel Cell Technical Team Roadmap*, **2017**, <https://www.energy.gov/eere/vehicles/downloads/us-drive-fuel-cell-technical-teamroadmap> (accessed: November 2021).
- [145] A. S. Leach, J. Hack, M. Amboage, S. Diaz-Moreno, H. Huang, P. L. Cullen, M. Wilding, E. Magliocca, T. S. Miller, C. A. Howard, D. J. L. Brett, P. R. Shearing, P. F. McMillan, A. E. Russell, R. Jervis, *J. Phys.: Condens. Matter* **2021**, *33*, 314002.
- [146] F. Jaouen, D. Jones, N. Coutard, V. Artero, P. Strasser, A. Kucernak, *Johnson Matthey Technol. Rev.* **2018**, *62*, 231.
- [147] M. Bernt, A. Siebel, H. A. Gasteiger, *J. Electrochem. Soc.* **2018**, *165*, F305.
- [148] Y. Lee, J. Suntivich, K. J. May, E. E. Perry, Y. Shao-Horn, *J. Phys. Chem. Lett.* **2012**, *3*, 399.
- [149] T. Reier, M. Oezaslan, P. Strasser, *ACS Catal.* **2012**, *2*, 1765.
- [150] S. E. S. El Wakkad, A. Hickling, *Trans. Faraday Soc.* **1950**, *46*, 820.
- [151] M. Morita, C. Iwakura, H. Tamura, *Electrochim. Acta* **1977**, *22*, 325.
- [152] J. W. Schultz, S. Mohr, M. M. Lohrengel, *J. Electroanal. Chem. Interfacial Electrochem.* **1983**, *154*, 57.
- [153] G. Młynarek, M. Paszkiewicz, A. Radniecka, *J. Appl. Electrochem.* **1984**, *14*, 145.
- [154] F. Song, L. Bai, A. Moysiadou, S. Lee, C. Hu, L. Liardet, X. Hu, *J. Am. Chem. Soc.* **2018**, *140*, 7748.
- [155] M. Wohlfahrt-Mehrens, J. Heitbaum, *J. Electroanal. Chem.* **1987**, *237*, 251.
- [156] O. Diaz-Morales, F. Calle-Vallejo, C. De Munck, M. T. M. Koper, *Chem. Sci.* **2013**, *4*, 2334.
- [157] J. Rossmeisl, Z. W. Qu, H. Zhu, G. J. Kroes, J. K. Nørskov, *J. Electroanal. Chem.* **2007**, *607*, 83.
- [158] I. C. Man, H. Y. Su, F. Calle-Vallejo, H. A. Hansen, J. I. Martínez, N. G. Inoglu, J. Kitchin, T. F. Jaramillo, J. K. Nørskov, J. Rossmeisl, *ChemCatChem* **2011**, *3*, 1159.
- [159] N. B. Halck, V. Petrykin, P. Krtil, J. Rossmeisl, *Phys. Chem. Chem. Phys.* **2014**, *16*, 13682.
- [160] J. Huang, S. B. Scott, I. Chorkendorff, Z. Wen, *ACS Catal.* **2021**, *11*, 12745.
- [161] S. B. Scott, J. Kibsgaard, P. C. K. Vesborg, I. Chorkendorff, *Electrochim. Acta* **2021**, *374*, 137844.
- [162] Y. Chen, S. Hu, F. Nichols, F. Bridges, S. Kan, T. He, Y. Zhang, S. Chen, *J. Mater. Chem. A* **2020**, *8*, 11649.
- [163] Z. Li, H. He, H. Cao, S. Sun, W. Diao, D. Gao, P. Lu, S. Zhang, Z. Guo, M. Li, R. Liu, D. Ren, C. Liu, Y. Zhang, Z. Yang, J. Jiang, G. Zhang, *Appl. Catal., B* **2019**, *240*, 112.
- [164] X. Han, X. Ling, D. Yu, D. Xie, L. Li, S. Peng, C. Zhong, N. Zhao, Y. Deng, W. Hu, *Adv. Mater.* **2019**, *31*, 1905622.
- [165] Y. Wang, A. Kumar, M. Ma, Y. Jia, Y. Wang, Y. Zhang, G. Zhang, X. Sun, Z. Yan, *Nano Res.* **2020**, *13*, 1090.
- [166] M. Ma, A. Kumar, D. Wang, Y. Wang, Y. Jia, Y. Zhang, G. Zhang, Z. Yan, X. Sun, *Appl. Catal., B* **2020**, *274*, 119091.
- [167] X. Zhao, X. Liu, B. Huang, P. Wang, Y. Pei, *J. Mater. Chem. A* **2019**, *7*, 24583.
- [168] G. C. da Silva, K. J. J. Mayrhofer, E. A. Ticianelli, S. Cherevko, *Electrochim. Acta* **2019**, *308*, 400.
- [169] M. Aresta, A. Dibenedetto, *J. Chem. Soc., Dalton Trans.* **2007**, 2975.

- [170] T. T. Zhuang, Z. Q. Liang, A. Seifitokaldani, Y. Li, P. De Luna, T. Burdyny, F. Che, F. Meng, Y. Min, R. Quintero-Bermudez, C. T. Dinh, Y. Pang, M. Zhong, B. Zhang, J. Li, P. N. Chen, X. L. Zheng, H. Liang, W. N. Ge, B. J. Ye, D. Sinton, S. H. Yu, E. H. Sargent, *Nat. Catal.* **2018**, *1*, 421.
- [171] C. Kim, T. Eom, M. S. Jee, H. Jung, H. Kim, B. K. Min, Y. J. Hwang, *ACS Catal.* **2016**, *7*, 779.
- [172] S. Mezzavilla, S. Horch, I. E. L. Stephens, B. Seger, I. Chorkendorff, *Angew. Chem., Int. Ed.* **2019**, *58*, 3774.
- [173] F. Cheng, X. Zhang, K. Mu, X. Ma, M. Jiao, Z. Wang, P. Limpachanangkul, B. Chalermisinsuwan, Y. Gao, Y. Li, Z. Chen, L. Liu, *Energy Technol.* **2021**, *9*, 2000799.
- [174] Y. Hori, A. Murata, R. Takahashi, *J. Chem. Soc., Faraday Trans. 1* **1989**, *85*, 2309.
- [175] R. B. Kutz, Q. Chen, H. Yang, S. D. Sajjad, Z. Liu, I. R. Masel, *Energy Technol.* **2017**, *5*, 929.
- [176] H. Shin, K. U. Hansen, F. Jiao, *Nat. Sustainability* **2021**, *4*, 911.
- [177] J. Jiao, R. Lin, S. Liu, W.-C. Cheong, C. Zhang, Z. Chen, Y. Pan, J. Tang, K. Wu, S.-F. Hung, H. M. Chen, L. Zheng, Q. Lu, X. Yang, B. Xu, H. Xiao, J. Li, D. Wang, Q. Peng, C. Chen, Y. Li, *Nat. Chem.* **2019**, *11*, 222.
- [178] Y. J. Zhang, V. Sethuraman, R. Michalsky, A. A. Peterson, *ACS Catal.* **2014**, *4*, 3742.
- [179] R. Daiyan, W. H. Saputera, H. Masood, J. Leverett, X. Lu, R. Amal, *Adv. Energy Mater.* **2020**, *10*, 1902106.
- [180] A. Bagger, H. Wan, I. E. L. Stephens, J. Rossmeisl, *ACS Catal.* **2021**, *11*, 6596.
- [181] Y. Hu, C. C. Lee, M. W. Ribbe, *Science* **2011**, *333*, 753.
- [182] Z. Y. Yang, D. R. Dean, L. C. Seefeldt, *J. Biol. Chem.* **2011**, *286*, 19417.
- [183] H. A. Hansen, J. B. Varley, A. A. Peterson, J. K. Nørskov, *J. Phys. Chem. Lett.* **2013**, *4*, 388.
- [184] S. Woonsup, S. H. Lee, J. W. Shin, S. P. Lee, Y. Kim, *J. Am. Chem. Soc.* **2003**, *125*, 14688.
- [185] A. S. Varela, W. Ju, A. Bagger, P. Franco, J. Rossmeisl, P. Strasser, *ACS Catal.* **2019**, *9*, 7270.
- [186] J. Li, P. Pršlja, T. Shinagawa, A. J. Martín Fernández, F. Krumeich, K. Artyushkova, P. Atanassov, A. Zitolo, Y. Zhou, R. García-Muelas, N. López, J. Pérez-Ramírez, F. Jaouen, *ACS Catal.* **2019**, *9*, 10426.
- [187] Y. Li, H. Su, S. H. Chan, Q. Sun, *ACS Catal.* **2015**, *5*, 6658.
- [188] A. Bagger, W. Ju, A. S. Varela, P. Strasser, J. Rossmeisl, *ChemPhysChem* **2017**, *18*, 3266.
- [189] A. Bagger, W. Ju, A. S. Varela, P. Strasser, J. Rossmeisl, *Catal. Today* **2017**, *288*, 74.
- [190] H. Shen, Y. Li, Q. Sun, *J. Phys. Chem. C* **2017**, *121*, 3963.
- [191] O. Matsushita, V. M. Derkacheva, A. Muranaka, S. Shimizu, M. Uchiyama, E. A. Luk'yanets, N. Kobayashi, *J. Am. Chem. Soc.* **2012**, *134*, 3411.
- [192] O. Enoki, T. Imaoka, K. Yamamoto, *Macromol. Symp.* **2003**, *204*, 151.
- [193] M.-J. Sun, Z.-W. Gong, J.-D. Yi, T. Zhang, X. Chen, R. Cao, *Chem. Commun.* **2020**, *56*, 8798.
- [194] T. Ding, X. Liu, Z. Tao, T. Liu, T. Chen, W. Zhang, X. Shen, D. Liu, S. Wang, B. Pang, D. Wu, L. Cao, L. Wang, T. Liu, Y. Li, H. Sheng, M. Zhu, T. Yao, *J. Am. Chem. Soc.* **2021**, *143*, 11317.
- [195] Y. Li, C. Chen, R. Cao, Z. Pan, H. He, K. Zhou, *Appl. Catal., B* **2020**, *268*, 118747.
- [196] X.-F. Qiu, H.-L. Zhu, J.-R. Huang, P.-Q. Liao, X.-M. Chen, *J. Am. Chem. Soc.* **2021**, *143*, 7242.
- [197] K. Zhao, X. Nie, H. Wang, S. Chen, X. Quan, H. Yu, W. Choi, G. Zhang, B. Kim, J. G. Chen, *Nat. Commun.* **2020**, *11*, 2455.
- [198] D. Karapinar, N. T. Huan, N. Ranjbar Sahraie, J. Li, D. Wakerley, N. Touati, S. Zanna, D. Taverna, L. H. Galvão Tizei, A. Zitolo, F. Jaouen, V. Mougel, M. Fontecave, *Angew. Chem., Int. Ed.* **2019**, *58*, 15098.
- [199] S. Chen, S. Perathoner, C. Ampelli, G. Centi, in *Horizons in Sustainable Industrial Chemistry and Catalysis* (Eds: S. Albonetti, S. Perathoner, E. A. Quadrelli), Elsevier, Amsterdam **2019**, pp. 31–46.
- [200] M. Capdevila-Cortada, *Nat. Catal.* **2019**, *2*, 1055.
- [201] J. Wang, S. Chen, Z. Li, G. Li, X. Liu, *ChemElectroChem* **2020**, *7*, 1067.
- [202] H. Iriawan, S. Z. Andersen, X. Zhang, B. M. Comer, J. Barrio, P. Chen, A. J. Medford, I. E. L. Stephens, I. Chorkendorff, Y. Shao-Horn, *Nat. Rev. Methods Primers* **2021**, *1*, 56.
- [203] J. H. Montoya, C. Tsai, A. Vojvodic, J. K. Nørskov, *ChemSusChem* **2015**, *8*, 2180.
- [204] N. Lazouski, Z. J. Schiffer, K. Williams, K. Manthiram, *Joule* **2019**, *3*, 1127.
- [205] J. A. Schwalbe, M. J. Statt, C. Chosy, A. R. Singh, B. A. Rohr, A. C. Nielander, S. Z. Andersen, J. M. McEnaney, J. G. Baker, T. F. Jaramillo, J. K. Nørskov, M. Cargnello, *ChemElectroChem* **2020**, *7*, 1542.
- [206] S. Liu, T. Qian, M. Wang, H. Ji, X. Shen, C. Wang, C. Yan, *Nat. Catal.* **2021**, *4*, 322.
- [207] A. R. Singh, B. A. Rohr, M. J. Statt, J. A. Schwalbe, M. Cargnello, J. K. Nørskov, *ACS Catal.* **2019**, *9*, 8316.
- [208] A. Logadottir, T. H. Rod, J. K. Nørskov, B. Hammer, S. Dahl, C. J. H. Jacobsen, *J. Catal.* **2001**, *197*, 229.
- [209] A. B. Jorge, R. Jervis, A. P. Periasamy, M. Qiao, J. Feng, L. N. Tran, M.-M. Titirici, *Adv. Energy Mater.* **2020**, *10*, 1902494.
- [210] J. Barrio, M. Volokh, M. Shalom, *J. Mater. Chem. A* **2020**, *8*, 11075.
- [211] J. Mahmood, E. K. Lee, M. Jung, D. Shin, I.-Y. Jeon, S.-M. Jung, H.-J. Choi, J.-M. Seo, S.-Y. Bae, S.-D. Sohn, N. Park, J. H. Oh, H.-J. Shin, J.-B. Baek, *Nat. Commun.* **2015**, *6*, 6486.
- [212] X. Zhang, A. Chen, Z. Zhang, M. Jiao, Z. Zhou, *J. Mater. Chem. A* **2018**, *6*, 11446.
- [213] X. Zhang, A. Chen, Z. Zhang, Z. Zhou, *J. Mater. Chem. A* **2018**, *6*, 18599.
- [214] Z. W. Chen, J.-M. Yan, Q. Jiang, *Small Methods* **2019**, *3*, 1800291.
- [215] L. Li, L. Xu, *Chem. Commun.* **2020**, *56*, 8960.
- [216] Y. Qian, Y. Liu, Y. Zhao, X. Zhang, G. Yu, *EcoMat* **2020**, *2*, e12014.
- [217] S. Z. Andersen, V. Čolić, S. Yang, J. A. Schwalbe, A. C. Nielander, J. M. McEnaney, K. Enemark-Rasmussen, J. G. Baker, A. R. Singh, B. A. Rohr, M. J. Statt, S. J. Blair, S. Mezzavilla, J. Kibsgaard, P. C. K. Vesborg, M. Cargnello, S. F. Bent, T. F. Jaramillo, I. E. L. Stephens, J. K. Nørskov, I. Chorkendorff, *Nature* **2019**, *570*, 504.
- [218] J. Choi, B. H. R. Suryanto, D. Wang, H. L. Du, R. Y. Hodgetts, F. M. Ferrero Vallana, D. R. MacFarlane, A. N. Simonov, *Nat. Commun.* **2020**, *11*, 5546.
- [219] Z. He, K. He, A. W. Robertson, A. I. Kirkland, D. Kim, J. Ihm, E. Yoon, G.-D. Lee, J. H. Warner, *Nano Lett.* **2014**, *14*, 3766.
- [220] L. Zhang, Y. Jia, H. Liu, L. Zhuang, X. Yan, C. Lang, X. Wang, D. Yang, K. Huang, S. Feng, X. Yao, *Angew. Chem., Int. Ed.* **2019**, *58*, 9404.
- [221] J. Masa, W. Xia, M. Muhler, W. Schuhmann, *Angew. Chem., Int. Ed.* **2015**, *54*, 10102.
- [222] C. Wei, R. R. Rao, J. Peng, B. Huang, I. E. L. Stephens, M. Risch, Z. J. Xu, Y. Shao-Horn, *Adv. Mater.* **2019**, *31*, 1806296.
- [223] R. Hu, Y. Li, Q. Zeng, J. Shang, *Appl. Surf. Sci.* **2020**, *525*, 146588.
- [224] W. Zhu, L. Zhang, S. Liu, A. Li, X. Yuan, C. Hu, G. Zhang, W. Deng, K. Zang, J. Luo, Y. Zhu, M. Gu, Z.-J. Zhao, J. Gong, *Angew. Chem., Int. Ed.* **2020**, *59*, 12664.
- [225] M. B. Solomon, T. L. Church, D. M. D'Alessandro, *CrystEngComm* **2017**, *19*, 4049.
- [226] D. M. D'Alessandro, *Chem. Commun.* **2016**, *52*, 8957.
- [227] S. Gong, C. Wang, P. Jiang, L. Hu, H. Lei, Q. Chen, *J. Mater. Chem. A* **2018**, *6*, 13254.
- [228] N. Cheng, L. Ren, X. Xu, Y. Du, S. X. Dou, *Adv. Energy Mater.* **2018**, *8*, 1801257.

- [229] J. Tang, Y. Yamauchi, *Nat. Chem.* **2016**, *8*, 638.
- [230] D. Liu, B. Wang, H. Li, S. Huang, M. Liu, J. Wang, Q. Wang, J. Zhang, Y. Zhao, *Nano Energy* **2019**, *58*, 277.
- [231] G. Zhang, Y. Jia, C. Zhang, X. Xiong, K. Sun, R. Chen, W. Chen, Y. Kuang, L. Zheng, H. Tang, W. Liu, J. Liu, X. Sun, W. F. Lin, H. Dai, *Energy Environ. Sci.* **2019**, *12*, 1317.
- [232] D. Menga, F. Ruiz-zepeda, L. Moriau, M. Šala, F. Wagner, T. P. Fellingner, *Adv. Energy Mater.* **2019**, *9*, 1902412.
- [233] U. I. Kramm, I. Herrmann-Geppert, S. Fiechter, G. Zehl, I. Zizak, I. Dorbandt, D. Schmeißer, P. Bogdanoff, *J. Mater. Chem. A* **2014**, *2*, 2663.
- [234] A. Mehmood, J. Pampel, G. Ali, H. Y. Ha, F. Ruiz-zepeda, T. P. Fellingner, *Adv. Energy Mater.* **2018**, *8*, 1701771.
- [235] S. Tian, Q. Fu, W. Chen, Q. Feng, Z. Chen, J. Zhang, W.-C. Cheong, R. Yu, L. Gu, J. Dong, J. Luo, C. Chen, Q. Peng, C. Draxl, D. Wang, Y. Li, *Nat. Commun.* **2018**, *9*, 2353.
- [236] E. Vorobyeva, E. Fako, Z. Chen, S. M. Collins, D. Johnstone, P. A. Midgley, R. Hauert, O. V. Safonova, G. Vilé, N. López, S. Mitchell, J. Pérez-Ramírez, *Angew. Chem., Int. Ed.* **2019**, *58*, 8724.
- [237] P. Zhou, X. Hou, Y. Chao, W. Yang, W. Zhang, Z. Mu, J. Lai, F. Lv, K. Yang, Y. Liu, J. Li, J. Ma, J. Luo, S. Guo, *Chem. Sci.* **2019**, *10*, 5898.
- [238] B. A. Glišić, L. Senerovic, P. Comba, H. Wadepohl, A. Veselinovic, D. R. Milivojevic, M. I. Djuran, J. Nikodinovic-Runic, *J. Inorg. Biochem.* **2016**, *155*, 115.
- [239] S. M. George, *Chem. Rev.* **2010**, *110*, 111.
- [240] Z. Chen, G. Zhang, J. Prakash, Y. Zheng, S. Sun, *Adv. Energy Mater.* **2019**, *9*, 1900889.
- [241] C. Detavernier, J. Dendooven, S. Pulinthanathu Sree, K. F. Ludwig, J. A. Martens, *Chem. Soc. Rev.* **2011**, *40*, 5242.
- [242] L. Du, W. Huang, Y. Zhang, X. Liu, Y. Ding, *Chem. Commun.* **2019**, *55*, 1943.
- [243] Y. Shao, Z. Guo, H. Li, Y. Su, X. Wang, *Angew. Chem., Int. Ed.* **2017**, *129*, 3274.
- [244] A. L. Johnson, J. D. Parish, in *Organometallic Chemistry*, Vol. 42, American Chemical Society **2018**, pp. 1–53.
- [245] B. C. Mallick, C. Hsieh, K. Huang, K. Yin, Y. A. Gandomi, *ECS J. Solid State Sci. Technol.* **2019**, *8*, N55.
- [246] B. S. Lim, A. Rahtu, R. O. Y. G. Gordon, *Nat. Mater.* **2003**, *2*, 749.
- [247] S. Liu, M. Wang, X. Yang, Q. Shi, Z. Qiao, M. Lucero, Q. Ma, K. L. More, D. A. Cullen, Z. Feng, G. Wu, *Angew. Chem., Int. Ed.* **2020**, *59*, 21698.
- [248] J. Zhang, Y. Zhao, X. Guo, C. Chen, C. L. Dong, R. S. Liu, C. P. Han, Y. Li, Y. Gogotsi, G. Wang, *Nat. Catal.* **2018**, *1*, 985.
- [249] L. Zhang, L. Han, H. Liu, X. Liu, J. Luo, *Angew. Chem., Int. Ed.* **2017**, *56*, 13694.
- [250] J. Zhang, J. Liu, L. Xi, Y. Yu, N. Chen, S. Sun, W. Wang, K. M. Lange, B. Zhang, *J. Am. Chem. Soc.* **2018**, *140*, 3876.
- [251] J. J. Zhao, J. J. Zhao, F. Li, Z. Chen, *J. Phys. Chem. C* **2018**, *122*, 19712.
- [252] X. Li, W. Zhong, P. Cui, J. Li, J. Jiang, *J. Phys. Chem. Lett.* **2016**, *7*, 1750.
- [253] Z. Tian, N. López-Salas, C. Liu, T. Liu, M. Antonietti, *Adv. Sci.* **2020**, *7*, 2001767.
- [254] Y. Zhu, J. Wang, H. Chu, Y.-C. Chu, H. M. Chen, *ACS Energy Lett.* **2020**, *5*, 1281.
- [255] J. Li, J. Gong, *Energy Environ. Sci.* **2020**, *13*, 3748.
- [256] M. Zachman, D. Chung, E. Holby, M. Chi, D. Cullen, *Microsc. Microanal.* **2020**, *26*, 162.
- [257] T. Mullarkey, C. Downing, L. Jones, *Microsc. Microanal.* **2020**, *26*, 2964.
- [258] D. M. Koshy, A. T. Landers, D. A. Cullen, A. V. Ievlev, H. M. Meyer, C. Hahn, Z. Bao, T. F. Jaramillo, *Adv. Energy Mater.* **2020**, *10*, 2001836.
- [259] F. S. Hage, G. Radtke, D. M. Kepaptsoglou, M. Lazzeri, Q. M. Ramasse, *Science* **2020**, *367*, 1124.
- [260] Z. Jakub, J. Hulva, M. Meier, R. Bliem, F. Kraushofer, M. Setvin, M. Schmid, U. Diebold, C. Franchini, G. S. Parkinson, *Angew. Chem., Int. Ed.* **2019**, *58*, 13961.
- [261] Y. Liang, J. H. K. Pfisterer, D. McLaughlin, C. Csoklich, L. Seidl, A. S. Bandarenka, O. Schneider, *Small Methods* **2019**, *3*, 1800387.
- [262] P. Sobotík, M. Setvín, P. Zimmermann, P. Kocán, I. Ošťádal, P. Mutombo, M. Ondráček, P. Jelínek, *Phys. Rev. B: Condens. Matter Mater. Phys.* **2013**, *88*, 205406.
- [263] Z. Jakub, F. Kraushofer, M. Bichler, J. Balajka, J. Hulva, J. Pavelec, I. Sokolović, M. Müllner, M. Setvin, M. Schmid, U. Diebold, P. Blaha, G. S. Parkinson, *ACS Energy Lett.* **2019**, *4*, 390.
- [264] J. Hulva, M. Meier, R. Bliem, Z. Jakub, F. Kraushofer, M. Schmid, U. Diebold, C. Franchini, G. S. Parkinson, *Science* **2021**, *371*, 375.
- [265] R. W. Haid, R. M. Kluge, T. O. Schmidt, A. S. Bandarenka, *Electrochim. Acta* **2021**, *382*, 138285.
- [266] K. Jiang, S. Back, A. J. Akey, C. Xia, Y. Hu, W. Liang, D. Schaak, E. Stavitski, J. K. Nørskov, S. Siahrostami, H. Wang, *Nat. Commun.* **2019**, *10*, 3997.
- [267] K. Jiang, S. Siahrostami, A. J. Akey, Y. Li, Z. Lu, J. Lattimer, Y. Hu, C. Stokes, M. Gangishetty, G. Chen, Y. Zhou, W. Hill, W.-B. Cai, D. Bell, K. Chan, J. K. Nørskov, Y. Cui, H. Wang, *Chem* **2017**, *3*, 950.
- [268] B. Gault, A. Chiaramonti, O. Cojocar-Mirédin, P. Stender, R. Dubosq, C. Freysoldt, S. K. Mäkinen, T. Li, M. Moody, J. M. Cairney, *Nat. Rev. Methods Primers* **2021**, *1*, 51.
- [269] J. Timoshenko, B. Roldan Cuenya, *Chem. Rev.* **2021**, *121*, 882.
- [270] M. M. Roessler, E. Salvadori, *Chem. Soc. Rev.* **2018**, *47*, 2534.
- [271] S. Wagner, H. Auerbach, C. E. Tait, I. Martinaiou, S. C. N. Kumar, C. Kübel, I. Sergeev, H. Wille, J. Behrends, J. A. Wolny, V. Schünemann, U. I. Kramm, *Angew. Chem., Int. Ed.* **2019**, *58*, 10486.
- [272] T. Spatzal, M. Aksoyoglu, L. Zhang, S. L. A. Andrade, E. Schleicher, S. Weber, D. C. Rees, O. Einsle, *Science* **2011**, *334*, 940.
- [273] Y. Le Mest, C. Inisan, A. Laouénan, M. L'Her, J. Talarmin, M. El Khalifa, J. Y. Saillard, *J. Am. Chem. Soc.* **1997**, *119*, 6095.
- [274] J. Nehrhorn, S. A. Bonke, A. Aliabadi, M. Schwalbe, A. Schnegg, *Inorg. Chem.* **2019**, *58*, 14228.
- [275] U. I. Kramm, I. Herrmann-Geppert, J. Behrends, K. Lips, S. Fiechter, P. Bogdanoff, *J. Am. Chem. Soc.* **2016**, *138*, 635.
- [276] L. Ni, C. Gallenkamp, S. Paul, M. Kübler, P. Theis, S. Chhabra, K. Hofmann, E. Bill, A. Schnegg, B. Albert, V. Krewald, U. I. Kramm, *Adv. Energy Sustainable Res.* **2021**, 2000064.
- [277] V. A. Saveleva, K. Ebner, L. Ni, G. Smolentsev, D. Klose, A. Zitolo, E. Marelli, J. Li, M. Medarde, O. V. Safonova, M. Nachttegaal, F. Jaouen, U. I. Kramm, T. J. Schmidt, J. Herranz, *Angew. Chem., Int. Ed.* **2021**, *60*, 11707.
- [278] J. Feng, R. Cai, E. Magliocca, H. Luo, L. Higgins, G. L. F. Romario, X. Liang, A. Pedersen, Z. Xu, Z. Guo, A. Periasamy, D. Brett, T. S. Miller, S. J. Haigh, B. Mishra, M.-M. Titirici, *Adv. Funct. Mater.* **2021**, 2102974.
- [279] M. Šiménas, J. O'Sullivan, C. W. Zollitsch, O. Kennedy, M. Seif-Eddine, I. Ritsch, M. Hülsmann, M. Qi, A. Godt, M. M. Roessler, G. Jeschke, J. J. L. Morton, *J. Magn. Reson.* **2021**, *322*, 106876.
- [280] S. A. Bonke, T. Risse, A. Schnegg, A. Brückner, *Nat. Rev. Methods Primers* **2021**, *1*, 33.
- [281] B. Hamzaoui, J. D. A. Pelletier, E. Abou-Hamad, Y. Chen, M. El Eter, E. Chermak, L. Cavallo, J.-M. Basset, *Chem. Eur. J.* **2016**, *22*, 3000.
- [282] T. Mineva, I. Matanovic, P. Atanassov, M. T. Sougrati, L. Stievano, M. Clémancey, A. Kochem, J. M. Latour, F. Jaouen, *ACS Catal.* **2019**, *9*, 9359.
- [283] U. I. Kramm, J. Herranz, N. Larouche, T. M. Arruda, M. Lefèvre, F. Jaouen, P. Bogdanoff, S. Fiechter, I. Abs-Wurmbach, S. Mukerjee, J. P. Dodelet, *Phys. Chem. Chem. Phys.* **2012**, *14*, 11673.
- [284] J. L. Kneebone, S. L. Daifuku, J. A. Kehl, G. Wu, H. T. Chung, M. Y. Hu, E. E. Alp, K. L. More, P. Zelenay, E. F. Holby, M. L. Neidig, *J. Phys. Chem. C* **2017**, *121*, 16283.

- [285] E. F. Holby, G. Wu, P. Zelenay, C. D. Taylor, *J. Phys. Chem. C* **2014**, *118*, 14388.
- [286] E. F. Holby, C. D. Taylor, *Sci. Rep.* **2015**, *5*, 9286.
- [287] G. Lalonde, R. Côté, G. Tamizhmani, D. Guay, J. P. Dodelet, L. Dignard-Bailey, L. T. Weng, P. Bertrand, *Electrochim. Acta* **1995**, *40*, 2635.
- [288] M. Lefèvre, J. P. Dodelet, P. Bertrand, *J. Phys. Chem. B* **2002**, *106*, 8705.
- [289] M. Lefèvre, J. P. Dodelet, P. Bertrand, *J. Phys. Chem. B* **2000**, *104*, 11238.
- [290] T. Matsui, S. Suzuki, Y. Katayama, K. Yamauchi, T. Okanishi, H. Muroyama, K. Eguchi, *Langmuir* **2015**, *31*, 11717.
- [291] J. Torrero, F. J. Pérez-Alonso, M. A. Peña, C. Domínguez, A. O. Al-Youbi, S. A. Al-Thabaiti, S. N. Basahel, A. A. Alshehri, S. Rojas, *ChemElectroChem* **2016**, *3*, 1072.
- [292] J. Torrero, M. A. Peña, M. Retuerto, L. Pascual, S. Rojas, *Electrochim. Acta* **2019**, *319*, 312.
- [293] G. Zhang, A. Kucernak, *ACS Catal.* **2020**, 9684.
- [294] K. Ding, A. Gulec, A. M. Johnson, N. M. Schweitzer, G. D. Stucky, L. D. Marks, P. C. Stair, *Science* **2015**, *350*, 189.
- [295] Y. Zhao, X. Yan, K. R. Yang, S. Cao, Q. Dong, J. E. Thorne, K. L. Materna, S. Zhu, X. Pan, M. Flytzani-Stephanopoulos, G. W. Brudvig, V. S. Batista, D. Wang, *ACS Cent. Sci.* **2018**, *4*, 1166.
- [296] I. X. Green, W. Tang, M. Neurock, J. T. Yates, *Science* **2011**, *333*, 736.
- [297] C. E. Tinberg, S. J. Lippard, *Acc. Chem. Res.* **2011**, *44*, 280.
- [298] M. Wirstam, S. J. Lippard, R. A. Friesner, *J. Am. Chem. Soc.* **2003**, *125*, 3980.
- [299] R. E. Stenkamp, *Chem. Rev.* **1994**, *94*, 715.
- [300] M. A. Thorseth, C. S. Letko, T. B. Rauchfuss, A. A. Gewirth, *Inorg. Chem.* **2011**, *50*, 6158.
- [301] Y. Lu, J. Wang, L. Yu, L. Kovarik, X. Zhang, A. S. Hoffman, A. Gallo, S. R. Bare, D. Sokaras, T. Kroll, V. Dagle, H. Xin, A. M. Karim, *Nat. Catal.* **2019**, *2*, 149.
- [302] A. S. Hoffman, D. Sokaras, S. Zhang, L. M. Debeve, C.-Y. Fang, A. Gallo, T. Kroll, D. A. Dixon, S. R. Bare, B. C. Gates, *Chem. - Eur. J.* **2017**, *23*, 14760.
- [303] J. Timoshenko, A. Anspoks, A. Cintins, A. Kuzmin, J. Purans, A. I. Frenkel, *Phys. Rev. Lett.* **2018**, *120*, 225502.
- [304] X. Guo, J. Gu, S. Lin, S. Zhang, Z. Chen, S. Huang, *J. Am. Chem. Soc.* **2020**, *142*, 5709.
- [305] J. N. Hansen, *Ph.D. Thesis*, Technical University of Denmark **2021**.
- [306] H. Sun, D. Liu, J. Du, *Chem. Sci.* **2019**, *10*, 657.
- [307] Z. Zhu, Z. Chen, Y. Yao, C. Cui, S. Li, X. Zhao, Q. Zhang, H. Tian, P. Xu, F. Xie, X. Xie, Y. Tan, S. Deng, J. M. Quimby, L. T. Scott, S. Xie, R.-B. Huang, L.-S. Zheng, *Sci. Adv.* **2019**, *5*, eaaw0982.
- [308] H. Chen, X. Zhang, Y. Zhang, D. Wang, D. Bao, Y. Que, W. Xiao, S. Du, M. Ouyang, S. T. Pantelides, H. Gao, *Science* **2019**, *365*, 1036.
- [309] H. Qiang, G. Zhuang, M. Zhang, J. Wang, S. Wang, Y. Wu, S. Yang, P. Du, *J. Am. Chem. Soc.* **2019**, *141*, 18938.



Angus Pedersen received his M.Eng. in Chemical Engineering with industrial placement from the University of Bath in 2019. He is currently pursuing a Ph.D. under the supervision of Prof. Maria-Magdalena Titirici and Dr. Ifan E. L. Stephens at Imperial College London and Prof. Dan J. L. Brett and Dr. Rhodri Jervis at University College London. Angus' research focuses on synthesizing and characterizing single and dual metal atom electrocatalysts for oxygen reduction in low-temperature hydrogen fuel cells.



Maria Magdalena Titirici received her Ph.D. from the University of Dortmund. She then completed a postdoc and later became a group leader at the Max-Planck Institute of Colloids and Interface. She held positions at Queen Mary University of London between 2013 and 2019, first as a reader and then full professor. She is currently a chair in Sustainable Energy Materials at Imperial College London and RAEng Chair in Emerging Technologies. Her research is in the field of sustainable materials for energy storage and conversion.



Ifan E. L. Stephens received his Ph.D. from the University of Cambridge. He conducted his postdoctoral studies at the Technical University of Denmark, first as a postdoctoral researcher and later became Assistant and Associate Professor there. In 2015, Massachusetts Institute of Technology appointed him as the Peabody Visiting Associate Professor. Since 2017 he has been at the Department of Materials at Imperial College London, where he currently holds the position of Reader in Electrochemistry. His research aims to enable the large scale electrochemical conversion of renewable energy to fuels and value chemicals and vice versa; his focus is on the electrocatalyst.